DISSERTATION

submitted to the

Combined Faculties for the Natural Sciences and for Mathematics

of the Ruperto-Carola University of Heidelberg, Germany

for the degree of

Doctor of Natural Sciences

Put forward by

Dipl. Phys. Benjamin Fröhlich

Born in Singen, Germany

Date of oral examination: 05.06.2019

Haemoglobinopathies and the Protection Against Severe Malaria: Probing Cytoadhesion and Mechanics of *Plasmodium falciparum* Infected Erythrocytes

Referees: Prof. Dr. Motomu Tanaka

Priv.-Doz. Dr. Falko Ziebert

Hämoglobinopathien und der Schutz vor schwerer Malaria: Untersuchung von Zelladhäsion und Zellmechanik von *Plasmodium falciparum* infizierten Erythrozyten

Ziel dieser Arbeit war die Untersuchung der Zelladhäsion und der mechanischen Eigenschaften von *Plasmodium falciparum* infizierten menschlichen wildtyp und hämglobinopatischen Erythrozyten, um den Schutzmechanism gegen schwere Malariaverläufe, der mit Hämoglobin Polymorphismen assoziiert wird, zu beleuchten.

In Kapitel 3 wurde die Zelladhäsion von infizierten wildtyp und hämoglobinopatischen Erythrozyten mit Hilfe von festkörpergestützten mit CD36 oder ICAM-1 funktionalisierten Lipiddoppelschichten untersucht, die als *in vitro* Modell der Enothelzellmembrane dienten. Unter statischen Bedingungen wurde die Bindungstärke durch den kritschen Ablösedruck quantifiziert, basierend auf der Zellablösung durch Laser induzierte Druckwellen. Zusätzlich wurde die Zahl der Bindungsereignisse und die kritische Ablöseschерspannung unter physiologisch relevanten Scherspannungen in klassischen Flusskammerexperimenten bestimmt. Darüber hinaus wurde durch labelfreie Interferenzreflexionsmokroskopie die Veränderungen der Adhäsionsfläche in Abhängigkeit der Scherspannung untersucht.

In Kapitel 4 wurden die, durch den Parasiten hervorgerufenen, Veränderungen der Erythrozytenmechanik für verschiedene Parasitenentwicklungsstadien mit labelfreier und kontaktfreier Flicker Spektroskopie untersucht, die detailierte Auskünfte über den Membranbiegemodulus, die Membranspannung, das harmonische Membranenconfinement durch das Zytoskelett und die effektive Zytosolviskosität gaben.

Ferner wurde durch quantitative Röntgenstrahlenfluoereszenzmikroskopie ein umfangreiches Bild des intraerythrozytischen Parasitenmetabolimus erstellt.

Haemoglobinopathies and the Protection Against Severe Malaria: Probing Cytoadhesion and Mechanics of *Plasmodium falciparum* Infected Erythrocytes

Aim of this thesis was the probing of the cytoadhesion and the mechanical properties of *Plasmodium falciparum* infected human wildtype and haemoglobinopathic erythrocytes, to shed light on the protection mechanism against severe malaria associated with haemoglobin polymorphisms.

In Chapter 3, the cytoadhesion of infected wildtype and haemoglobinopathic erythrocytes was probed using solid-supported lipid bilayers functionalized with CD36 or ICAM-1, acting as *in vitro* endothelial cell membrane models. Under static conditions, the binding strength was quantified in terms of the critical pressure of detachment based on cell detachment by laser induced pressure waves. Additionally, the number of binding events and the critical shear stress of detachment were determined based on classical parallel plate flow experiments at physiological relevant shear stresses. Furthermore, the shear stress dependent changes in tight adhesion area were investigated based on label-free reflection interference contrast microscopy.

In Chapter 4, the parasite induced changes to the erythrocyte mechanics were probed at different parasite stages using label and contact-free flicker spectroscopy, yielding the membrane bending modulus, the membrane tension, the harmonic membrane confinement by the cytoskeleton and the apparent cytosolic viscosity.

Moreover, a comprehensive image of the intraerythrocytic parasite metabolism was generated using quantitative scanning X-ray fluorescence microscopy.

“Kindly let me help you or you will drown,” said the monkey putting the fish safely up a tree.

Alan Wilson Watts (1915-1973)

Acknowledgements

I would like to thank…

…Prof. Dr. Motomu Tanaka for the continuous support, the helpful guidance throughout my thesis and the never ending patience in our many fruitful discussions. Additionally, I would like to thank him for giving me the chance to travel to Japan and France to broaden my scientific horizon.

…Priv.-Doz. Dr. Falko Ziebert for kindly acting as second referee for my thesis and as examiner for my thesis defense.

…Prof. Dr. Michael Lanzer for all the discussions, providing a rich background on the biology of erythrocytes and *P. falciparium*.

…Prof. Dr. Ulrich Schwarz for many suggestions and continuous input from the field of theoretical biophysics.

…Dr. Christine Lansche for being such a good friend, for the shared time, for the long explanations on the various biological facets of *P. falciparium* and for making this thesis possible.

…Dr. Anil Dasanna and **Julia Jäger** for sharing your knowledge and providing such a friendly environment, especially throughout all our malaria meetings.

…Dr. Stefan Kaufmann for your help at all times and for the continues effort to improve my backhand.

…Dr. Mariam Veschgini for so many fruitful lunchbreaks.

…Dr. Akihisa Yamamoto for your continuous motivation and scientific input throughout the years and the uncountable number of Tokyo bananas.

…Judith Thoma for taking care of a piece of aluminum foil, when I needed a safe place for it.

…Federico Amadei for providing a relentless Italian flavor to AK Tanaka.

…Salomé Mielke, **Sven Mehlhose** and **Philipp Linke** for providing a friendly atmosphere in the lab and beyond.

…Dr. Yang Yang for the friendly support during the stay at ESRF and many rounds of explanation.

…Dr. Yuji Higaki for the fruitful cooperation.

…Gabriele Fabry and **Mieko Yoshida** for helping with all organizational tasks in Heidelberg and Japan.

…all other current and former **members of AK Tanaka** and **members of AK Lanzer** for your continuous support and many beautiful and happy memories.

Last, but not least, I want to thank the two most important girls in my life…

…my most beloved love of all love loves, **Sonja Koschuhar** for her never ending patience, understanding and support during this time.

…my daughter, **Elenor Ophelia Koschuhar**, for providing motivational smiles and full diapers at all times.

Table of Contents

1 Introduction

1.1 The human red blood cell

Human red blood cells (erythrocytes) are highly specialized cells and the principal transporter delivering oxygen to body tissues in exchange for carbon dioxide. They have a biconcave-discoid shape with an equatorial diameter of 6 to 8 µm and a thickness of 2 to 3 µm, creating a high surface (~135 µm^2) to volume (~90 µm^3) ratio, optimized for the fast uptake and release of oxygen[1, 2]. Mature erythrocytes lack internal cell organelles and are mainly composed of the oxygen binding protein haemoglobin to maximize the oxygen transport capacity.

The resulting low cytoplasmic viscosity together with their unique cell shape allow erythrocytes to repeatedly navigate through capillaries with diameters of only 2 to 3 µm without taking damage[3]. The necessary high deformability is mainly provided by the unique structure of the erythrocyte membrane. It consists of a highly fluidic 4 to 5 nm thick phospholipid bilayer anchored to a flexible two-dimensional spectrin/actin-cytoskeleton (Figure 1.1)[4].

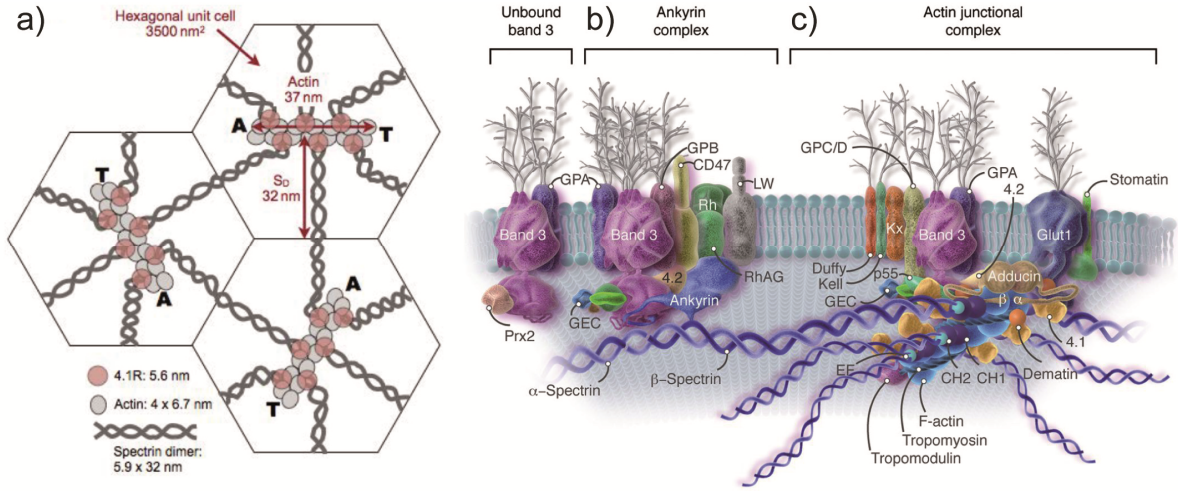

Figure 1.1 | Model of the erythrocyte membrane (adapted from Samuel E. Lux, IV, 2015)[5]. (a) The erythrocyte cytoskeleton is based on a quasi-hexagonal spectrin-actin meshwork. Short actin protofilaments are interconnected by up to six spectrin tetramers. The cytoskeleton is anchored to the plasma membrane by vertical connections of (b) spectrin via the ankyrin complex or (c) the actin protofilaments via the actin junctional complex. The surface of the membrane is decorated with a glycocalix consisting mainly of glycoproteins A-D.

The cytoskeleton consists of a quasi-hexagonal meshwork of spectrin tetramers interconnecting short actin protofilaments (Figure 1.1 a)[6]. The spectrin tetramers are made of two coupled dimers, which in turn are each formed by a pair of antiparallel aligned α-spectrin and β-spectrin units. The high flexibility of the spectrin network can be attributed to the ability of the spectrin tetramers to dissociate and reform under shear stress conditions[7]. In addition, the tetramers themselves are highly extensible. While the typical *in vivo* end-to-end distance of the tetramer is found between 35-100 nm[8, 9], it can extend up to 190 nm when spread *in vitro*[10].

The anchoring of the cytoskeleton to the erythrocyte membrane is mainly mediated by two vertical connector types. Firstly, ankyrin complexes (Figure 1.1 b), that connect spectrin tetramers via the ankyrin protein to the integral membrane protein Band 3[6], and secondly, actin junctional complexes (Figure 1.1 c), that connect the actin protofilaments via α-β-adducin to the Band 3[6, 11].

To further minimize interactions with endothelial cells, that cover the inside of the micro vascular system, and with other erythrocytes, the erythrocytes surface is covered with a negatively charged glycocalix[12].

During their live time of 100 to 120 days the erythrocytes shrink accompanied by a loss of ~20% of haemoglobin, while the cytosolic concentration increases by ~14%[13, 14]. The increase in cytoplasmic viscosity together with an increased membrane rigidity finally promotes the removal of aged erythrocytes during passages through the spleen.

1.2 Malaria

1.2.1 Background on Malaria

Malaria is an infectious disease in humans caused by the protozoan parasite *Plasmodium* most commonly transmitted by an infected female *Anopheles* mosquito. Infection typically causes a range of unspecific symptoms including fever, headache or chills. Yet, a lack of treatment can lead up to life threatening conditions. The species *Plasmodium falciparum* is responsible for the most severe forms of malaria in humans, resulting in an estimated 438,000 deaths in 2015 alone, especially among children under the age of five, pregnant women and non-immune travelers[15, 16].

1.2.2 The blood stages of *P. falciparum*

An infected mosquito typically inoculates < 25 sporozoites into the host skin. Sporozoites are a highly motile cell species able to enter the blood stream and invade the liver. There they multiply asexually for ~10 days creating approximately 40000 merozoites.

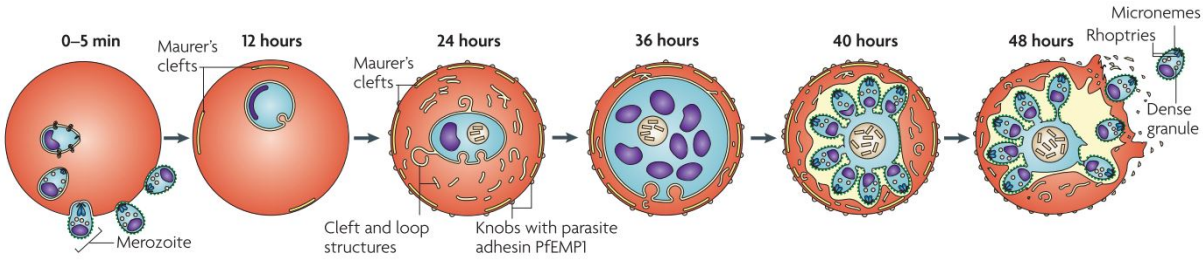

Figure 1.2 | Blood stage of *plasmodium falciparum* (reproduced from Maier *et al.* 2009)[17]. One or multiple merozoites invade an uninfected human red blood cell. 24 h post invasion the erythrocyte membrane is decorated with knobs and infected cells develop cytoadhesive capabilities. The intraerythrocytic parasite maturation leads to the destruction of the host cell and the release of 16-32 new merozoites after ~48 hours[18].

Upon release from the liver into the blood flow, this parasite form is able to penetrate the membrane of human erythrocytes[18].

The approximately 48 h lasting intraerythrocytic development cycle is initiated by the ~5 min lasting invasion process of an erythrocyte by one or several merozoites (Figure 1.2)[18]. Erythrocytes are consecutively remolded by the parasite leading to the formation of novel cytosolic organelles such as Maurer's cleft (ring stage up to 16 h post invasion) and the formation of membrane protrusions termed knobs (trophozoite stage 20 to 36 h post invasion)[18]. Finally, each infected erythrocyte releases between 16-32 asexually reproduced merozoites upon bursting (end of schizont stage 48 h post invasion). 10% of the intraerythrocytic parasites develop into the sexual forms termed gametocytes[19]. Gametocytes circulate freely through the blood stream and can be taken up by another mosquito during its blood meal. For information on the intra-mosquito development of *P. falciparum* please see[18].

The clinical picture of *P. falciparum* induced malaria can be largely attributed to this asexual intraerythrocytic development and multiplication cycle[20, 21]. While most of the infections with malaria are accompanied only with asymptomatic levels of parasitaemia (percentage of infected erythrocytes) or mild fever, roughly 1 to 2% of infections can progress to life threating conditions[22, 23].

The WHO classifies malaria cases as severe, if patients fulfill one or several criteria, such as hyper-parasitaemia, severe anemia or cerebral malaria (Supporting Table 8-1)[24]. Among them, cerebral malaria is the most common severe form among children, causing up to 30% of total deaths[25, 26]. The earliest pathological features observable in severe cases are the presence of late stage infected erythrocytes in capillaries, post capillary venules and various organs including the brain, the hearth and the liver[27].

1.2.3 Haemoglobin based intraerythrocytic metabolism of *P. falciparum*

Human haemoglobin is a tetramer structure consisting of two α-globin and two β-globin chains. Each unit embeds heme, a porphyrin group complexing a ferrous iron atom (Fe^{II}) enabling haemoglobin to bind and release oxygen[28].

During the intraerythrocytic development, haemoglobin acts as an important source of amino acids, required for the parasite mediated protein synthesis (Figure 1.3)[29]. Upon haemoglobin degradation, the liberated free heme group acts as a very toxic and reactive monomer species[30]. *P. falciparum* developed the capability to store heme in the form of hemozoin crystals, rendering the heme groups biochemically inert.

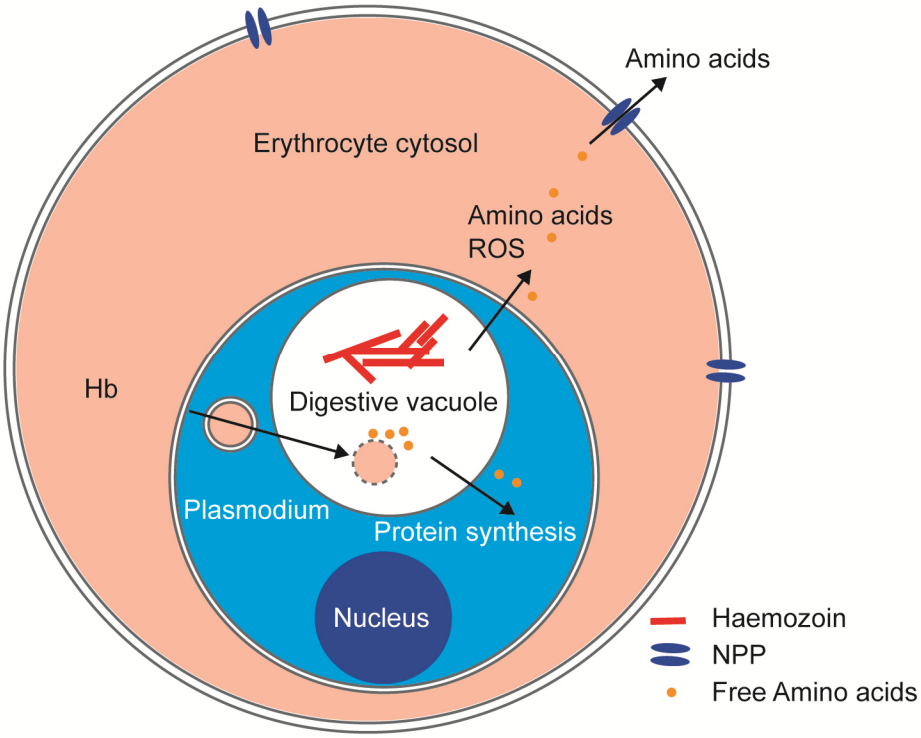

Figure 1.3 | Simplified *P. falciparum* mediated haemoglobin digestion. Host cytosolic volume is uptaken via cytosome, passing the parasite membrane and the digestive vacuole membrane. Inside the digestive vacuole, haemoglobin (Hb) is digested by a cascade of parasite enzymes. The toxic residual heme is stored in crystalline form as haemozoin. The freed amino acids are either used for parasite mediated protein syntheses or transported into the extracellular space by new permeation pathways (NPP). The digestion process leads to the enhanced production of reactive oxygen species (ROS).

Although 65% - 80% of total hemoglobin is degraded during the parasites maturation, only a small fraction of below 25% of liberated amino acids is in fact incorporated into parasite encoded proteins[31], while the majority is released into the extracellular space via porin-like channels and other specific amino acid transporters[32, 33]. In the framework of the colloid-osmotic model, this apparent wasteful behavior has been explained by the need to reduce the osmotic pressure to avoid premature cell lysis[34, 35].

1.2.4 Cytoadhesive capabilities of *P. falciparum* infected erythrocytes

The intraerythrocytic development leads to a variety of changes to the erythrocyte cytosolic composition and the structure of the host cell membrane. Thereby, the volume and the mechanics of the infected red blood cell are altered in a similar fashion as observed during red blood cell aging, making them targets for splenic clearance[36]. The hereditary survival strategy of *P. falciparum* is based on the circumvention of splenic passages by the development of cytoadhesive capabilities.

During the early ring stage *P. falciparum* sets up Maurer's clefts, large membranous structures that mediate trafficking of parasite encoded proteins through the erythrocyte cytosol (Figure 1.2). To reach to the erythrocyte membrane, they are connected to long actin filaments built up by the parasite, based on actin mined from the erythrocyte cytoskeleton[37, 38]. Thereafter,

the capability for cytoadherence is established via the formation of membrane protrusions termed “knobs” that emerge at the trophozoite stage of infection and are decorated with adhesive proteins (Figure 1.4)[39, 40].

The knob structures are mainly supported by the knob associated histidine rich protein (KAHRP), a variety of other parasite encoded proteins and protein structures naturally embedded in the host membrane (Figure 1.4 a)[41, 42]. Please note, that studies based on KAHRP knockouts demonstrated that KAHRP is essential for the formation of knobs[43]. A membrane surface of an infected erythrocyte can express as many as 10000 knobs with reported heights between 2-20 nm and diameters between 5-120 nm dependent of the parasite strain[44, 45, 46].

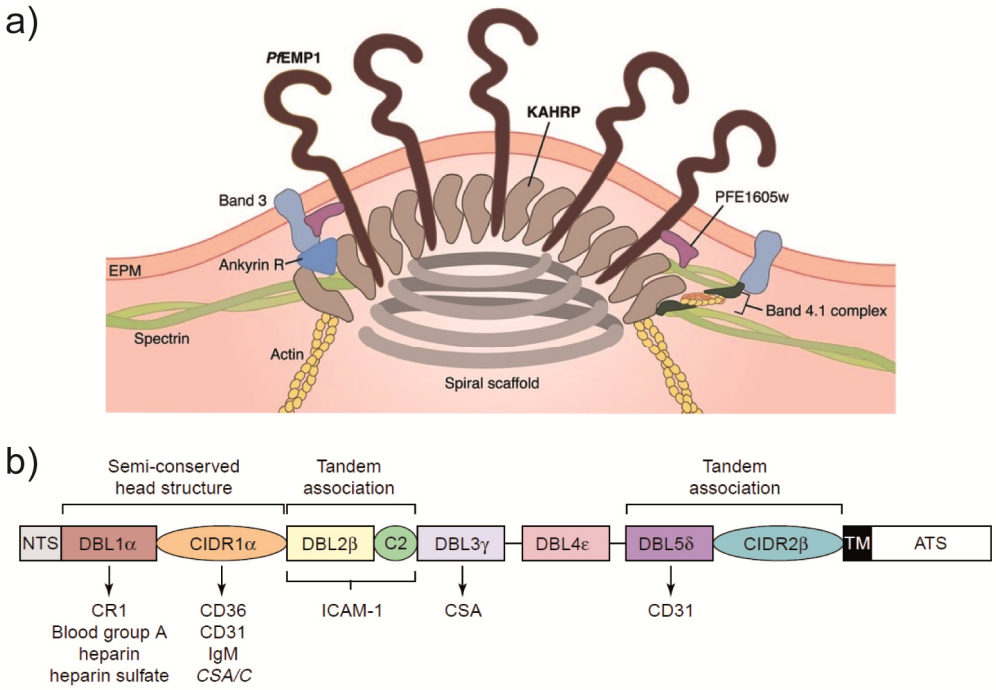

Figure 1.4 | Schematics of *P. falciparum* induced membrane protrusions termed “knobs” and the binding domains of the major adhesins PfEMP1. (a) “Knob” structures built upon knob associated histidine rich proteins (KHARP) are strongly connected to the underlying actin/spectrin cytoskeleton and provide an elevated platform for PfEMP1 (reproduced from Helms *et al.* 2016)[47]. (b) Protein architecture of PfEMP1 with the intracellular domain (ATS). The extracellular domain is highly variable but is mainly dominated by sequences of Duffy-Binding Like (DBL) and Cysteine-Rich Inter-Domain Regions (CIDR) domains that facilitate binding to key receptors like ICAM-1, CD36 or CSA. (adapted from Smith *et al.* 2001)[48].

The major *P. falciparum* adhesins termed as *Plasmodium falciparum* erythrocyte membrane protein 1 (PfEMP1) are anchored to these knob structures[49]. PfEMP1 proteins are encoded by a var-gene family and can mediate cytoadhesion to a variety of host receptors like CD36, intercellular adhesion molecule 1 (ICAM-1), chondroitin sulfate A (CSA) and others[50]. The binding is mediated by large extracellular ectodomains consisting of 2-10 copies of mainly two domain types, namely Duffy-Binding Like (DBL) and Cysteine-Rich Inter-Domain Region (CIDR) domains[51, 52]. Thereby, each infected erythrocyte only expresses a single PfEMP1 variant, thus minimizing the exposure of the parasite antigenic repertoire[53, 54].

1.2.4.1 Cytoadhesion mediated by CD36 and ICAM-1

P. falciparum infected erythrocytes have the ability to bind to a variety of ligands expressed on the surface of vascular endothelial cells. Of these, both CD36 and ICAM-1 are of special interest, since they have been associated with severe forms of malaria[55, 56, 57, 58].

CD36 is an integral membrane protein (MW = 88 kDa) of the family of class B scavenger receptors and able to bind ligands including collagen, native lipoproteins and long-chain fatty acids. Its main functions involve fatty acid metabolism, angiogenesis and phagocytosis[59]. Since it is expressed on all vascular endothelial cells, with abundancies in organs like the liver, kidney, lungs and muscles, CD36 is generally involved in various cases of clinical malaria[60]. The fact that CD36 is also expressed on activated platelet cells can contribute to the severity of the disease, due to cell clumping (auto-agglutination) and subsequent mechanical capillary obstruction[61]. Binding to CD36 is mediated via the cysteine rich inter domain regions in PfEMP1 (Figure 1.4 b)[62].

ICAM-1 is a transmembrane protein (MW = 80 − 115 kDa) and a member of the immunoglobulin superfamily. Similar to CD36 it is expressed on endothelial cells where it mediates adhesion of leukocytes during immune and inflammatory responses[63]. It is highly abundant in organs like the lungs and the brain[64], with the later abundancy linked to cases of cerebral malaria[57, 65]. Binding to ICAM-1 is mediated via Duffy-Binding-Like domain DBL2β in PfEMP1 (Figure 1.4 b)[66].

1.2.5 Influence of haemoglobin polymorphisms on *P. falciparum*

Several human polymorphisms of the haemoglobin protein provide distinct resistance against severe forms of malaria. As a consequence of the selective pressure exerted by *P. falciparum* during the several thousand years of co-evolution, large parts of the population in malaria endemic areas are carriers of such haemoglobin disorders[67, 68]. The disorders can be categorized into haemoglobin structure variants, where amino acids are substituted in the α- or β-globin (haemoglobin S, haemoglobin C), and haemoglobin synthesis variants, where the synthesis of the haemoglobin is altered due to the lack of synthesized α- or β-globin (α- and β-thalassemia)[28].

1.2.5.1 Haemoglobin S and C

Haemoglobin S distinguishes itself from wildtype haemoglobin A by a single amino acid substitution at position 6 of the β-globin, where glutamic acid is exchanged to valine (β 6Glu→Val)[69]. This change from a polar to a non-polar amino acid creates a binding side for deoxygenated haemoglobin, leading to haemoglobin aggregation, characteristic for haemoglobin S[70]. The haemoglobin aggregation in turn reduces the oxygen carrying capacity and can induce the destruction of the erythrocyte. While this can lead to fatale conditions like severe anemia for carriers of the homozygote form (HbSS, sickle cell disease), carriers of the heterozygote from (HbAS, sickle-cell trait) are mostly clinically asymptotic[71].

In haemoglobin C the glutamic acid at position 6 of the β-globin is exchanged to a positively charged lysine (β 6Glu→Val)[69]. Similar to haemoglobin S, carriers of the homozygote form (HbCC) can suffer from chronic anemia while carriers of the heterozygote form (HbAC) are also clinically asymptotic[71].

Most interestingly, carriers of the sickle-cell trait (HbAS) are highly protected against malaria, with ~90% reduced likelihood to develop severe malaria conditions and ~60% reduced probability to require clinical care compared to carriers of wildtype haemoglobin (HbAA)[72]. Comparable protection rates are provided for carriers of HbAC with ~90% reduced likelihood to develop severe malaria conditions and ~30% reduced probability to require clinical care[72].

1.2.5.2 Protective mechanisms of HbAS and HbAC

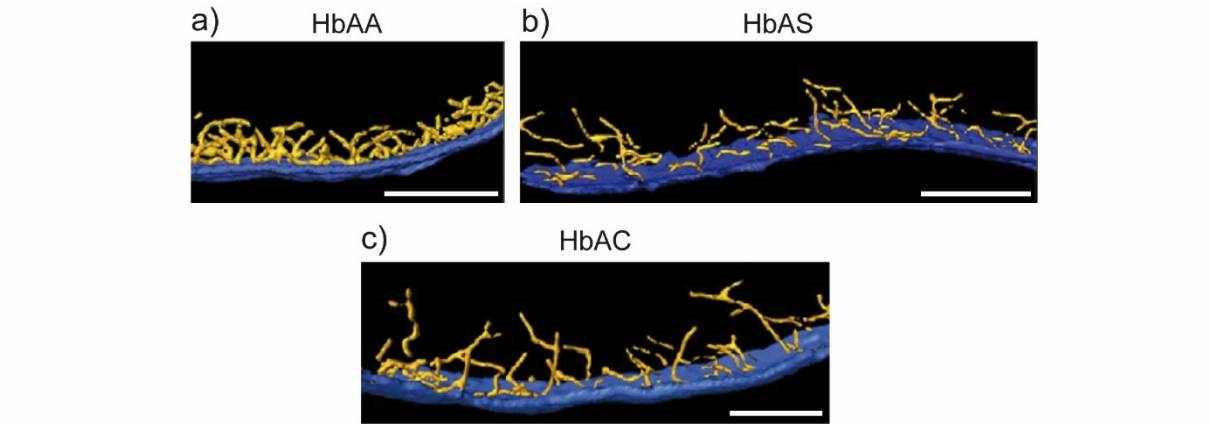

Figure 1.5 | Distorted cytoskeleton in uninfected erythrocytes (adapted from Cyrklaff *et al.*)[73]. Surface rendering of the plasma membrane (dark blue) and the actin filaments (yellow) calculated from cryo-electron tomograms. Reconstruction for (a) a wildtype erythrocyte, (b) and (c) for haemoglobinopathic erythrocytes of type HbAS and type HbAC, respectively. Scale bars, 100 nm.

Haemoglobin S and C are chemically unstable with elevated rates of auto oxidization, leading to higher amounts of reactive species like ferric haemoglobin $HbFe^{III}$, that can degrade to form haemichromes, and ferryl haemoglobin $HbFe^{IV}$ [74, 75]. Haemichromes disturb the spectrin-protein 4.1-actin binding, while the additional oxidative stress brought upon by reactions with ferryl haemoglobin interferes directly with actin polymerization and actin dynamics[76, 77]. Both effects result in distorted cytoskeletons characteristic for haemoglobinopathic erythrocytes (Figure 1.5).

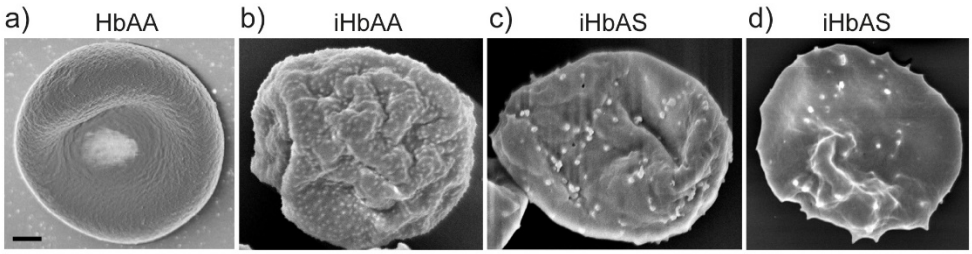

Figure 1.6 | Changes in erythrocyte surface morphology by *P. falciparum*. (a) Uninfected wildtype erythrocytes display a smooth surface (b-d) Infected erythrocytes at the trophozoite stage present membrane protrusions on the surface, with varying size and density dependent on the blood type. (SEM imaging was performed by Dr. Marek Cyrklaff, Center for Infectious Diseases, Heidelberg University Hospital).

The high oxidative stress levels in haemoglobinopathic erythrocytes combined with the additional oxidative stress due to the parasite metabolic activity (Figure 1.3) are believed to be a major source of their protective capabilities. Analogue to the interference of the actin activity in uninfected erythrocytes, the parasite mediated reorganization of actin should be strongly disturbed in haemoglobinopathic erythrocytes. This in turn results in a distorted protein trafficking system[38] and might explain the abnormal size and distribution of knobs (Figure 1.6) and the lower level of PfEMP1 expression for infected HbAS and HbAC erythrocytes[78]. This observation correlates with the reduced cytoadhesive capabilities to microvascular endothelia cells observed under static and flow conditions for infected HbAS and HbAC erythrocytes[78, 79]. As a clear consequence infected HbAS and HbAC erythrocytes should indeed perform more passages through the spleen, resulting in a higher probability to be removed, thereby possibly moderating the disease symptoms.

1.3 Aims of this study

In spite of reduced cytoadhesion of *P. falciparum* infected haemoglobinopathic erythrocytes observed *in vitro*[78, 79], carriers of HbAS and HbAC, suffering from a malaria infection, have been reported to exhibit parasitemia levels comparable to patients with wildtype haemoglobin[80, 81]. This raised the question: How can haemoglobinopathies protect from severe malaria?

Primary aim of this study was the detailed quantification of infected wildtype (iHbAA) and haemoglobinopathic erythrocytes (iHbAS) adhesion capability to the endothelial cell receptors CD36 and ICAM-1, both of which are associated with cases of severe malaria[55, 57], to gain insight on their individual contributions to the sequestration process.

The cytoadhesion was investigated using CD36 and ICAM-1 functionalized solid-supported lipid bilayers acting as *in vitro* models mimicking the endothelial cell surface[82, 83, 84]. They allow to fine-tune the intermolecular ligand distance $\langle d \rangle$ on a nanometer scale[82, 85] and provide a high lateral ligand mobility[86] comparable to biological membranes.

Under static conditions, the adhesion strength of iHbAA and iHbAS to CD36 and ICAM-1 was quantified in terms of the critical pressure of detachment $P_{\mathrm{crit}}(\langle d \rangle)$, obtained by detaching cells using picosecond laser pulse induced supersonic pressure waves (Chapter 3.2). The combination of functionalized solid-supported lipid bilayers with parallel flow chambers, further allowed to determine the adhesion probability and the critical shear stress of detachment $\tau_{\mathrm{crit}}(\langle d \rangle)$ as a function of physiological relevant shear stresses (Chapter 3.3). Label free reflection interference contrast microscopy was applied to quantify the adhesion area of individual iHbAA and iHbAS as a function of applied shear stress τ (Chapter 3.4).

The intraerythrocytic development of *P. falciparum* induces drastic changes the host cell mechanical properties, resulting in loss in cell deformability. Cell mechanics are directly correlated to processes like cytoadhesion[87], mechanical capillary obstruction[88, 89] and splenic clearance[90].

Secondary aim of this study was the detailed quantification of cell mechanics of iHbAA and iHbAS/iHbAC to investigate how the differences in knob morphology and distribution[78], as well as differences in the cytoskeleton structure observed for iHbAA and iHbAS/iHbAC[73] are affecting their cell mechanical properties.

Cell mechanics of individual iHbAA, iHbAS and iHbAC were probed using non-invasive, label free flicker spectroscopy based on the analysis of thermally and non-thermally induced membrane fluctuations in Fourier space (Chapter 4.1)[91]. The study included uninfected erythrocytes and infected erythrocytes at the ring and trophozoite stage of infection. Additionally, a genetically modified knobless parasite phenotype was investigated.

Based on recent reports of delayed protein expression for iHbAS and iHbAC in comparison to iHbAA[34, 92], the scope of this study was extended to investigate how the intraerythrocytic development and biochemical metabolism of *P. falciparum* is affected by the host haemoglobin.

Quantitative X-ray scanning fluorescence microscopy was performed on uninfected and infected erythrocytes at the trophozoite stage to provide an image of the elemental composition with high spatial resolution and trace-level sensitivity (Chapter 4.2)[93, 94].

2 Materials and methods of cell culture

This chapter contains a short overview of all applied methods necessary for the continuous and stage synchronized *in vitro* cultivation of *P. falciparum* FCR3 in human erythrocytes. It includes all techniques necessary to generate highly purified suspensions of infected erythrocytes used throughout this study.

2.1 Ethical clearance

Conducted experiments within this study were following the guidelines of the ethics committee of Heidelberg University, Mannheim University Hospital and the Biomolecular Research Center (CERBA/Labiogene). Written consent was obtained for all voluntary donors in accordance with the relevant guidelines and regulations.

2.2 Buffers and solutions

All chemicals used to prepare aqueous buffer solutions were purchased either form Karl Roth (Karlsruhe, Germany), Thermo Fisher Scientific (Waltham, USA) or Sigma-Aldrich Co. (St. Louis, USA).

Culture medium:

RPMI 1640, 2 mM L-glutamine, 25 mM HEPES, 100 µM hypoxanthine, 20 µg/mL gentamicin and 10% (v/v) human serum (A^+ for type HbAA, AB for types HbAS and HbAC).

Sorbitol lysis solution:

280 mM D-sorbitol, 5 mM HEPES, pH 7.4. (300 mOsm), (heat sterilized).

MACS buffer:

Phosphate buffered saline (PBS), 2 mM EDTA, 0.5% (w/v) Bovine serum albumin (BSA), pH 7.4.

Gelatin solution:

RPMI 1640, 2 mM L-glutamine, 25 mM HEPES, 0.5% (w/v) gelatin (from porcine skin type A).

RPMI-BSA:

RPMI 1640, 2 mM L-glutamine, 25 mM HEPES and 0.1% BSA (w/v) at pH 7.4.

2.3 Blood collection and genotyping

A total volume of approximately 12 ml of citrated whole blood was collected per donor. Whole blood was centrifuged at 800 × g for 10 min at room temperature. After discarding the plasma and buffy coating layer, the remaining erythrocytes were washed three times in RPMI-1640 basic medium and stored at 4°C. Haemoglobin genotyping was performed by the Zentrallabor and Koopertives Speziallabor of the Heidelberg University Hospital. Erythrocytes were used within two weeks after collection.

2.4 In vitro culture of *P. falciparum*

P. falciparum was cultured following the description of Trager and Jensen[95]. Briefly, Parasites were cultured in human erythrocytes suspended in culture medium under controlled atmospheric conditions (3% CO_2, 5% O_2, 92% N_2 and 96% humidity). The parasitemia was kept below 5%.

2.5 Determination of parasitemia levels

Small volumes of erythrocyte suspension were smeared over glass cover slips and fixed in absolute methanol, followed by a staining with 10% (v/v) Giemsa solution for 20 min. After washing and drying under nitrogen flow, the coverslips were mounted onto a light microscope using a 100 × oil-immersion objective. Parasitemia was estimated as a percentage from at least 1000 counted cells.

2.6 Synchronization of *P. falciparum* using D-sorbitol

P. falciparum induces additional pathways through the plasma membrane of the infected erythrocytes, often termed as new permeation pathways (NPP). Therefore, infected cells exhibit an increasing permeability to small solutes like D-sorbitol approximately 16 h post invasion. The incubation of infected erythrocytes older than 16 h with a D-sorbitol solution induces haemolyzation, while earlier parasite stages and uninfected erythrocytes are not affected.

In a first step, erythrocytes were collected from culture by centrifugation at 500 × g for 2 min and washed with PBS buffer. The resulting pellet was resuspended in sorbitol lysis solution and incubated at 37°C for 5 min. Sorbitol lysis solution was removed by additional centrifugation, afterwards the pellet was resuspended into culture medium. To achieve a high temporal synchronicity of 4 to 6 hours, the synchronization steps were repeated again after 12 h.

2.7 Magnetic column isolation

During intraerythrocytic development of *P. falciparum*, the parasite digests the host haemoglobin and stores the remaining haemozoin groups in heme crystals to avoid toxification (Chapter 4.2.2). Thereby the diamagnetic ferrous Fe^{II} of oxyhaemoglobin changes to the paramagnetic ferric Fe^{III} of haemozoin. This phenomenon is exploited by magnetic column isolation to reach a purification of infected erythrocytes (trophozoite, schizont) up to ~98%[96, 97].

In a first step, a magnetic activated cell sorting (MACS) separation column was mounted into the vario MACS magnetic support (Miltenyi Biotec, Bergisch Gladbach, Germany), filled with pre-warmed MACS buffer and incubated for 20 min at RT. Whole parasite cultures were loaded into the magnetic column. The culture volume traverses the column at a flow rate of 1 drop/sec. Thereafter, non-interacting cells (uninfected and ring stages) were washed away by 50 ml of pre-warmed MACS buffer. Afterwards, the column was removed from the MACS

magnetic support and washed again with 10 ml of MACS buffer. The purified infected erythrocytes were washed three times in RPMI 1640 medium and counted using a particle counter (Z1, Beckman Coulter, Krefeld, Germany). Additionally, blood smears were produced to ensure the desired purification level.

The obtained highly purified erythrocytes were used directly for experiments or to parasitize HbAS and HbAC cultures.

2.8 Panning of *P. falciparum* to human dermal microvascular endothelial cells

The *P. falciparum* FC3 parasites were panned against ICAM-1 and CD36 following the procedure by Claessens and Rowe[98]. The panning process was exclusively performed by Dr. Christine Lansche[46]. Briefly, infected erythrocytes at the trophozoite stage were co-incubated on a confluent layer of endothelial cells, expressing ICAM-1 and CD36. Non-sticking infected erythrocytes were removed by washing. Adhesive infected cells were kept in co-culture with the endothelial cells for 24 h and were harvested afterwards by vigorously washing with RPMI incomplete medium. The parasite binding capability was monitored using static adhesion assays[46].

3 Interaction of infected red blood cells with key receptors

The following chapters comprise a detailed study on the interaction of infected red blood cells with CD36 and ICAM-1 functionalized solid-supported lipid bilayers, that act as *in vitro* endothelial cell membrane models (Chapter 3.1). Under static condition, the adhesiveness was quantified by the critical pressure of detachment P_{crit} as a function of mean intermolecular ligand distance $\langle d \rangle$ of CD36 or ICAM-1, based on the cell detachment by laser induced pressure waves (Chapter 3.2). Additionally, the adhesion probability and the critical shear stress of detachment τ_{crit} were determined as a function of physiological shear stresses using parallel flow chambers (Chapter 3.3). The application of reflection interference contrast microscopy further provided a quantification of the adhesion area of individual cells (Chapter 3.4). Each subchapter contains a detailed background description of the applied method, an overview of the experimental conditions and the obtained results.

3.1 Endothelial cell model system

3.1.1 Background on cell adhesion

Classically, cell adhesion has been described as an interplay between different short-range attractive forces, mid-range generic repulsive forces and the elastic stresses due to the formation of an adhesion area[99, 100]. Thereby the attractive forces are originating from highly specific interactions between ligand-receptor pairs, while the repulsive forces are typically caused by neutral biopolymers constituting the glycocalix.

In the case of an elastic shell, resembling an erythrocyte, the elastic free energy ΔG_{adh} can be described according to the Helfrich theory of soft shells[99, 100]:

$$\Delta G_{\mathrm{adh}} = -\omega A_{\mathrm{Adh}} + \Delta G_{\mathrm{grav}} + \int_S \left[\frac{\kappa}{2}\left(\Delta h(\boldsymbol{x})\right)^2 + \frac{\sigma}{2}\left(\nabla h(\boldsymbol{x})\right)^2 + V(h(\boldsymbol{x}))\right] d\boldsymbol{x}. \qquad 3\text{-}1$$

The first term describes the change in free energy by the formation of specific-ligand receptor pairs inside the cell adhesion area A_{Adh} under the assumption of a homogenous binding energy per unit area ω. The binding energy density $\omega = \partial \Delta G_{\mathrm{adh}} / \partial \Delta A_{\mathrm{adh}}$ is a function of the density of binders and their individual affinity, but also relates to the membrane elasticity and steric interactions[87, 101]. The second term describes the contribution of gravity[102].

The integral over the whole cell surface constitutes the energy contribution associated with the membrane bending modulus κ and the membrane tension σ. The last term in equation (3-1) denotes to the effective interfacial potential $V(h(\boldsymbol{x})$ per unit area and consists of:

$$V\big(h(\boldsymbol{x})\big) \cong V_{\mathrm{hyd}}\big(h(\boldsymbol{x})\big) + V_{\mathrm{vdW}}\big(h(\boldsymbol{x})\big) + V_{\mathrm{rep}}\big(h(\boldsymbol{x})\big). \qquad 3\text{-}2$$

The first two terms denote to the potential create by two bare membranes in close proximity. The short-range hydration repulsion $V_{\mathrm{hyd}}\big(h(\boldsymbol{x})\big)$ can be approximated phenomenologically as:

$$V_{\mathrm{hyd}}\big(h(\boldsymbol{x})\big) = V_0 e^{-h/\lambda} \qquad 3\text{-}3$$

With V_0 in the range of $V_0 < 30$ mJ m^{-2} and a characteristic decay length of $\lambda < 1$ nm.

The attractive van der Waals (vdW) interactions arising from induced or permanent dipoles of the two layers are given by:

$$V_{\mathrm{vdW}}\big(h(\boldsymbol{x})\big) = -\frac{H_{\mathrm{A}}}{12\pi}\left(\frac{1}{(h+2\delta)^2} + \frac{1}{(h)^2} + \frac{1}{(h+\delta)^2}\right), \qquad 3\text{-}4$$

with H_{A} being the Hamaker constant with a typical range of $H_{\mathrm{A}} \sim 10^{-21}$ J for phospholipid membranes. The last term in (3-2) describes the generic repulsion evoked from neutral polymers on the surface of the cell, which act as repellers :

$$V_{\mathrm{rep}}\big(h(\boldsymbol{x})\big) \cong \begin{cases} \frac{\pi}{6} k_{\mathrm{B}} T \sigma_0 \left(\frac{R_{\mathrm{g}}}{h(\boldsymbol{x})}\right)^2 e^{-1.5\left(\frac{h(\boldsymbol{x})}{R_{\mathrm{g}}}\right)^2}, & h \gg R_{\mathrm{g}} \\ k_{\mathrm{B}} T \sigma_0, & h \ll R_{\mathrm{g}}, \end{cases} \qquad 3\text{-}5$$

where R_{g} denotes to the radius of gyration of the polymer and σ_0 to the density of repellers. In many cases the generic potential $V\big(h(\boldsymbol{x})\big)$ can be approximated as harmonic with an equilibrium height h_0:

$$V(h(x)) \cong V_0 + \tfrac{1}{2}\gamma(h - h_0)^2, \qquad 3\text{-}6$$

Where γ represents the effective spring constant of the potential[100, 103]. The harmonic potential often is corrected for the Helfrich repulsion as a consequence of the suppression or freezing of thermally and non-thermally excited membrane fluctuations:

$$V_{\mathrm{und}}\big(h(x)\big) = \frac{(k_{\mathrm{B}}T)^2}{\kappa h^2}. \qquad 3\text{-}7$$

3.1.2 Mimicking endothelial cells

In vitro model systems are used to investigate the interaction of cells either with a specific ligand species or directly with other cells or cell types. In the field of malaria research, the models for specific ligand studies often consist of plastic substrates covered with different concentrations of purified ligands[104]. On the other hand, cell-cell interactions are probed typically using confluent layers of vascular endothelial cells or human tissue samples[46, 105, 106].

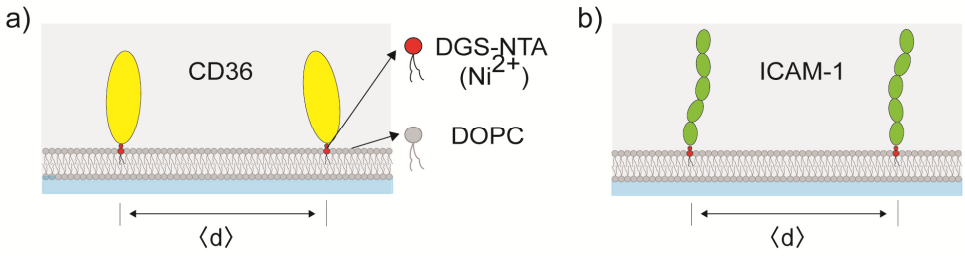

Figure 3.1 | Schematics of functionalized solid-supported lipid bilayers. The variation of the molar fraction between the matrix lipid DOPC and the anchor or functionalization lipid DGS-NTA (Ni^{2+}) allows to fine-tune the mean intermolecular distance $\langle d \rangle$ on a nanometer scale. The *P. falciparum* targets (a) CD36 and (b) ICAM-1 are bound to DGS-NTA (Ni^{2+}) via a poly-histidine tag.

Yet, the first model can suffer from ill-defined local ligand densities and doesn't allow for lateral movement of the deposited receptors. The second model does not allow to derive the role of a specific ligand type, since living cells typically express a large variety of receptors with highly variable receptor densities.

In vitro models based on solid-supported lipid bilayers functionalized (shortened as functionalized bilayers) with single receptor species allow to quantitatively probe the role of specific receptors. They consist of a single phospholipid bilayer deposited onto a glass substrate (Figure 3.1). The in cooperation of phospholipids coupled to specific ligands at fixed molar ratios allow to fine-tune the intermolecular ligand distance $\langle d \rangle$ on a nanometer scale[82, 85]. Additionally, the phospholipid bilayer provides a high lateral ligand mobility, similar to those in biological membranes[86].

3.1.3 Experimental realization

3.1.3.1 Buffers

All chemicals used to prepare aqueous buffer solutions were purchased either form Karl Roth (Karlsruhe, Germany), Thermo Fisher Scientific (Waltham, USA) or Sigma-Aldrich Co. (St. Louis, USA).

HBS-buffer:

10 mM HEPES and 150 mM NaCl at pH 7.5.

HBS-Ni^{2+} loaded-buffer:

10 mM HEPES, 150 mM NaCl and 1 mM $NiCl_2$ at pH 7.5.

HBS-Ca^{2+} loaded-buffer:

10 mM HEPES, 150 mM sodium chloride and 1 mM $CaCl_2$ at pH 7.5.

3.1.3.2 Lipids and proteins

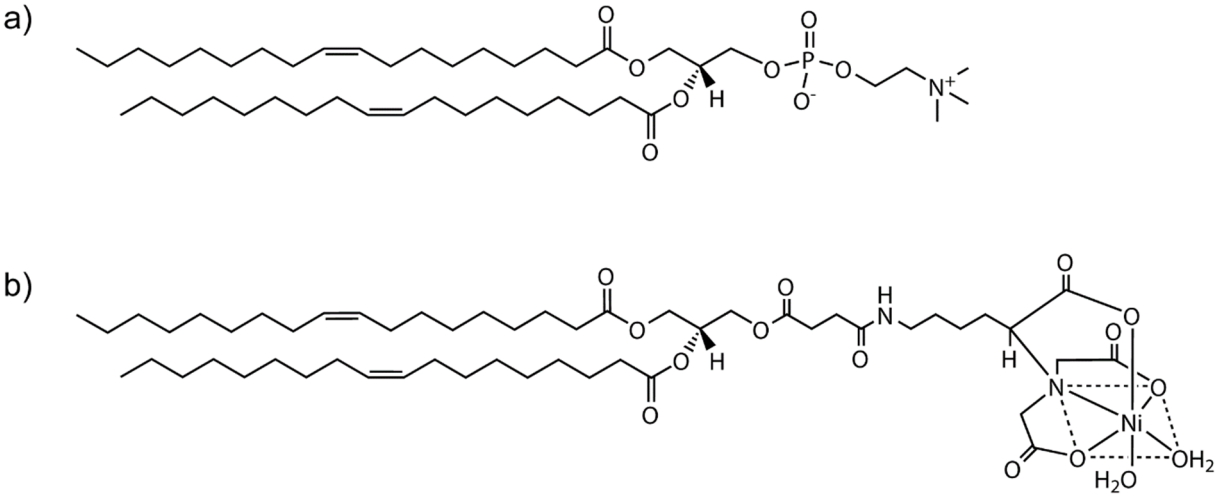

Figure 3.2 | Synthetic phospholipids. Solid-supported membranes are composed of (a) the matrix phospholipid DOPC and (b) the functionalization lipid DOGS-NTA (Ni^{2+}) mixed at different molar ratios.

1,2-dioleoyl-sn-glycero-3-phosphocholine (DOPC, Figure 3.2) and 1,2-dioleoyl-*sn*-glycero-3-[(N-(5-amino-1-carboxypentyl)iminodiacetic acid)succinyl] (nickel salt) (DOGS-NTA (Ni^{2+}), Figure 3.2) were purchased from Avanti Polar Lipids (Alabaster, USA). Hexa-histidine-tagged human proteins ICAM-1 and CD36 were purchased from Thermo Fischer Scientific (Waltham, USA).

3.1.3.3 Substrates

Glass substrates were cleaned based on a modified RCA protocol[107] consisting of consecutive sonication steps in acetone, ethanol, methanol, water and a 1 : 1 : 5 (v/v/v) solution of H_2O_2(30%)/NH_4OH(25%)/H_2O each for 3 min at room temperature. Thereafter, substrates were incubated in this solution for 30 min at 60°C, followed by intensive rinsing with ultrapure water. Finally, the substrates were dried at 70°C and stored in a vacuum chamber at room temperature.

For laser induced pressure wave experiments (Chapter 3.2), round microscopic glass slides ($Ø = 28$ mm) from Gerhard Menzel Gmbh (Braunschweig, Germany) were glued to bottomless culture dishes purchased from Ibidi (Martinsried, Germany) using polydimethylsiloxane (SYLGARD184) purchased from Dow Corning Co. (Shanghai, China). For flow based experiments (Chapters 3.3 and 3.4) bottomless plastic parallel flow chambers (µ-Slide VI$^{0.4}$) were glued to 25×75 mm^2 microscopic grade glass slides, purchased from the same respective companies.

3.1.3.4 Vesicle preparation

DOPC and DOGS-NTA (Ni^{2+}) stock solutions (5 mg/mL, $CHCl_3$) were mixed at different molar ratios χ. Thereafter, the obtained solutions were dried under a gentle stream of nitrogen gas and stored under vacuum conditions to remove residual chloroform. The dried lipids were resuspended (0.5 mg/mL) in HBS-buffer and sonicated using a titanium micro-tip sonicater (Misonix, Farmingdale, USA) for 30 min to create small unilamellar vesicles (SUV). Residual titanium was removed by centrifugation of the vesicle suspensions (13400 rpmi, 10 min).

3.1.3.5 Deposition of supported membranes and functionalization

The lipid vesicle suspensions were incubated inside the respective chambers for 1 h at room temperature. Solid-supported lipid bilayers were formed by vesicle fusion[108]. Excess SUVs were removed by intensive rinsing with HBS-Ni^{2+} loaded-buffer, followed by an incubation period of 1 h to saturate the nickel chelating nitrilotriacetic acid (NTA) headgroups. Afterwards, the chambers were rinsed with HBS-Ca^{2+} loaded-buffer and the protein solutions (50 µg/mL) was added and incubated overnight at room temperature. The intermolecular distance $\langle d \rangle$ of the monomerly incorporated lipid anchors, and therefore the mean intermolecular ligand distance was calculated using the molar ratios χ and a lipid head area size of $A_{\mathrm{lipid}} \sim 65$ Å^2[109, 110]:

$$\langle d \rangle = \sqrt{\frac{A_{lipid}}{\chi}}. \qquad 3\text{-}8$$

The binding between histidine tagged proteins and NTA group carrying lipids was intensively studied by our group using quartz-crystal microbalance with dissipation[109] and grazing incidence X-ray fluorescence[109, 111]. The quality of the solid-supported lipid bilayers, the functionality of the NTA-histidine binding as well as the homogenous covering with both CD36 and ICAM-1 were tested on a regular basis (Supporting Figure 8.1).

3.2 Pressure wave based evaluation of cell adhesion strength

3.2.1 Background on the quantification of cell adhesion strength

In the past a variety of methods has been developed to quantify the mechanical strength of binding between an individual adherent cell and its respective target (e.g. adjacent cells, single receptors or functionalized artificial membranes). The most popular among these methods are micropipette aspiration[112, 113], cell manipulation by optical or magnetic tweezers[114, 115, 116, 117], or atomic force microcopy (AFM) peeling[118, 119, 120]. All techniques probe the adhesion strength differently and are limited to a specific range of applied forces/stresses and the corresponding resolution (Table 3-1).

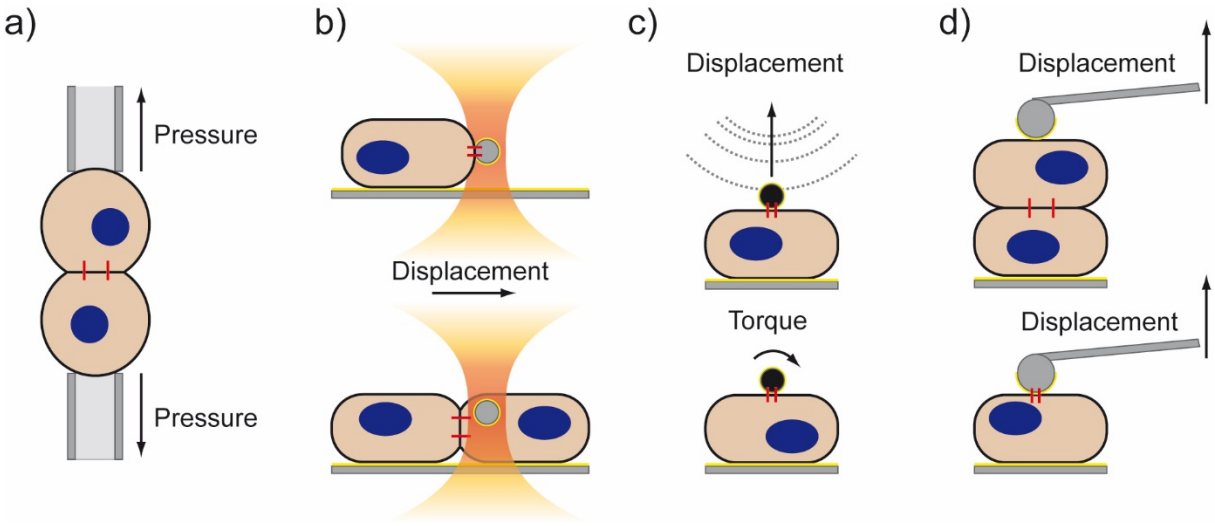

Figure 3.3 | Comparison of techniques used to determine the mechanical strength of an adherent cell and its respective binding partner. Cell-cell adhesion is highlighted in red and adhesion to the specific ligands in yellow. (a) Adhesion strength is probed as a function of applied sucking pressure in the connected capillary. (b) Functionalized dielectric microbeads are attached to the cell membrane. Force is applied by displacing the laser focus and subsequently the position of the bead. (c) Force is induced by displacing functionalized magnetic beads adherent to the cell surface via an external magnetic field. (d) Force is induced directly by mechanically displacing a functionalized adherent bead.

There are three general disadvantages all presented techniques share. (1) The adhesion strength is determined non-contact-free, (2) the techniques usually are highly time-consuming and therefore yield poor statistics, and (3) due to the small loading rates the inelastic cell response is included in the derived values.

Table 3-1 | Comparison of techniques used to study the cell-cell or cell-substrate adhesion strength.

Technique	Force/Stress (resolution)	Statistics [cells/h]
Micropipette Aspiration	0-700 Pa (0.1 Pa)[113, 121]	5-10
Optical Tweezers	0-300 pN (5 pN)[114, 115]	5-10
Magnetic Tweezers	0-120 pN (1 pN)[122]	5-10
Atomic Force Microscopy	0-20 nN (1 pN)[123]	1-5

An elegant technique, circumventing these three disadvantages, is the quantification of adhesion strength based on picosecond laser pulse induced pressure waves[124]. As depicted in Figure 3.4 the setup consists of an infrared picosecond laser focused above a planar substrate. Due to high energy input per pulse (~25 mJ) combined with a short pulse duration (~28 ps FWHM) the aqueous medium evaporates forming a cavitation bubble[125, 126]. Both the formation and the collapse of this cavitation bubble generate intensive pressure waves able to detach cells from the substrate. Thereby, the nature of the pressure waves, characterized by their supersonic propagation velocity ($V_{\mathrm{water}} \sim 1640\ \mathrm{ms}^{-1}$) combined with the already mentioned pulse duration, largely hampers any inelastic responses of the cells[124].

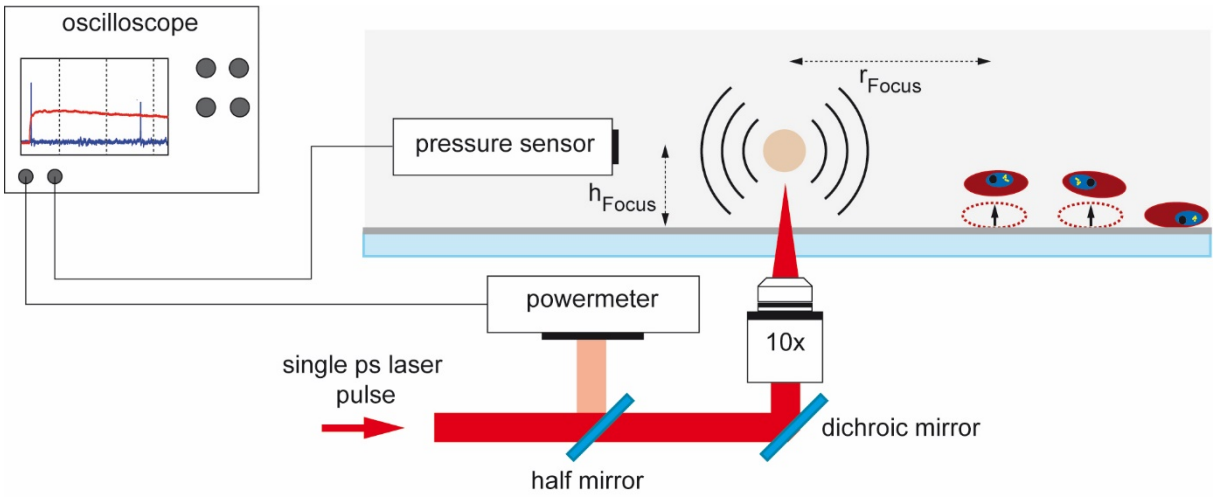

Figure 3.4 | Experimental setup for picosecond laser pulse induced supersonic pressure waves. Single laser pulses are focused at distance h_{Focus} above the substrate. Cell detachment events due to the propagating pressure wave are recorded as a function of radial distance r_{Focus} to the focal point.

3.2.2 Experimental realization

3.2.2.1 Picosecond laser pulse setup and calibration

The experimental setup consisted of a Nd:YAG laser system ($\lambda = 1064$ nm, $E_{\mathrm{Pulse,Max}} = 25$ mJ, FWHM $= 28 \pm 3$ ps, EKSLPLA, Vilnius, Lithuania) coupled to an inverted microscope (Eclipse TE2000-U, Nikon, Amstelveen, Netherlands Europe). The measurement chamber was prepared as previously described (Chapter 3.1.3). All experiments were conducted after cells were incubated for 1 h on the substrates at cell densities below 200 cells/mm². Infected erythrocytes (RPMI-BSA) were kept at 37°C using a self-built cell incubation chamber. Laser pulses were focused at $h_{\mathrm{Focus}} = 500$ µm above the substrate surface using a 10x/0.30 objective. Images were taken two times before and two times after the laser pulse was applied for different radial positions covering the range of $r_{\mathrm{Focus}} = 0 - 5.7$ mm (Figure 3.4).

Prior or directly following each experiment, the system was calibrated using a piezo electric hydrophone (Müller Instruments, Oberursel, Germany), yielding the hydrodynamic pressure P as a function of the applied laser pulse energy E_{Pulse} and as a function of the radial distance r_{Focus} from the focal point (Figure 3.5).

3.2.2.2 Categorization of adherent vs non-adherent cells

In a first step, the position of each individual cell was determined from the two image sequences taken before the application of the laser pulse $I_{B,1}$ and $I_{B,2}$ and after the application of the laser pulse $I_{A,1}$ and $I_{A,2}$ based on an edge detection algorithm. Cells loosely hovering above the substrate were identified by their movement between $I_{B,1}$ and $I_{B,2}$ (caused by the microscope table movement) and excluded from further analyses. Thereafter, cells were categorized as adhesive, if their center of mass position (CM) did not change by more than a third of their diameter $\Delta = 2.5$ µm between the image series $I_{B,2}$ and $I_{A,1}$ and as detached otherwise. To correct for cells that were detached but didn't exhibit lateral movement, cells moving between $I_{B,1}$ and $I_{B,2}$ were also categorized as detached. Cells found at a distance $r_{\mathrm{Focus}} < R_{min} = 1.2$ mm were not subjected to the analyses to avoid artefacts due to the direct exposure to the cavitation bubble (Supporting Information 8.3.3).

Lastly, the cell position was converted to "experienced pressure" based on the corresponding calibration functions $P(r_{\mathrm{Focus}})$ and $P\ (E_{\mathrm{Pulse}})$.

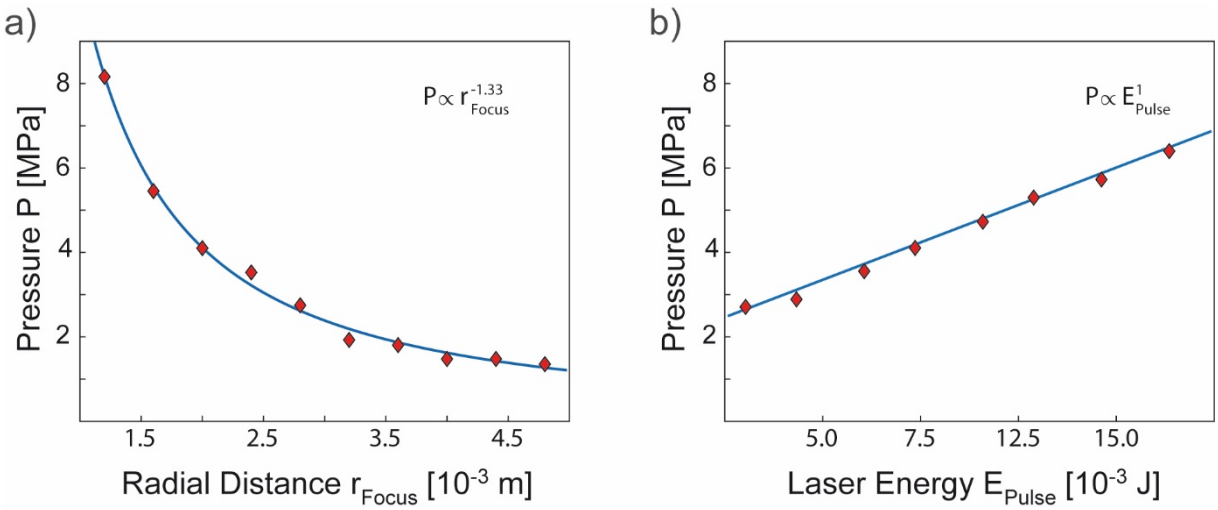

Figure 3.5 | Pressure wave calibration. (a) Pressure P as a function of radial distance from the laser focus point r_{Focus} using a constant laser energy of $E_{\mathrm{Pulse}} = 7.5$ mJ and the corresponding power law coefficient. (b) Linear dependency of applied pressure P as a function of the laser pulse energy E_{Pulse} measured at a constant distance of $r_{\mathrm{Focus}} = 2$ mm.

3.2.3 Results

As a first step, the adhesion strength was determined for infected wildtype erythrocytes (iHbAA) adhering to CD36 and ICAM-1 functionalized bilayers with varying mean intermolecular ligand distances $\langle d \rangle$ (Figure 3.6 a, b). The critical pressure of detachment P_{crit} was calculated based on the assumption that the population follows a Gaussian distribution characterized by P_{crit} with a standard deviation σ. Consequently, the pressure dependent fraction of detached cells $\chi_{\mathrm{D}}(P)$ should follow:

$$\chi_{\mathrm{D}}(P) = \frac{1}{2}(1 - \chi_{\mathrm{U}})\left(\mathrm{erf}\left(\frac{P - P_{\mathrm{crit}}}{\sqrt{2}\sigma}\right) + 1\right) + \chi_{\mathrm{U}}, \qquad 3\text{-}9$$

where χ_U denotes to the fraction of unbound cells before the laser pulse. It should be noted that this fraction was not excluded during the first categorization presented above (Chapter 3.2.2.2). The measured data sets exhibited the sigmoidal trend as predicted by equation (3-9) independent of the ligand type or the mean intermolecular ligand distance $\langle d \rangle$. Thereafter, the experiments were performed using infected haemoglobinopathic erythrocytes (iHbAS, sickle-cell trait) (Figure 3.6 c, d).

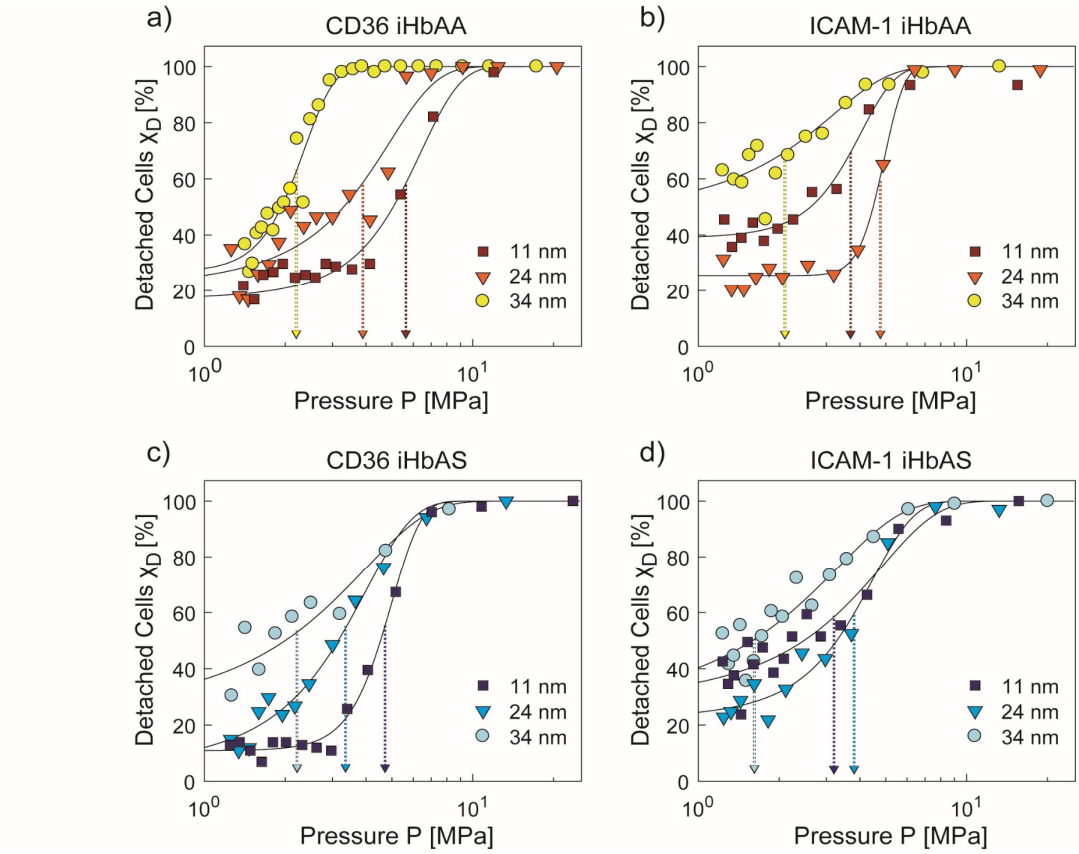

Figure 3.6 | Detachment of adherent cells by picosecond laser pulse induced pressure waves. (a) Representative data sets depicting the fraction of detached cells χ_D as a function of sustained pressure P for infected wildtype (iHbAA) erythrocytes. Cells were seeded onto CD36 functionalized bilayers at various intermolecular ligand distances $\langle d \rangle$. Single data points correspond to 50 individual cells. Vertical arrows indicate the critical pressure of detachment derived by fitting the data to equation (3-9) (b) Corresponding data sets for infected wildtype erythrocytes on ICAM-1 functionalized bilayers. (c), (d) Respective data sets using infected haemoglobinopathic (iHbAS) erythrocytes.

The dependency of P_{crit} on $\langle d \rangle$ was probed for $\langle d \rangle = 7 - 94$ nm (Figure 3.7). In the case of CD36, P_{crit} was found to monotonically decrease with increasing ⟨d⟩ for both iHbAA and iHbAS. The obtained $P_{\text{crit,iHbAA,CD36}}(\langle d \rangle)$ for infected wildtype erythrocytes were found to be significantly higher than corresponding values $P_{\text{crit,iHbAS,CD36}}(\langle d \rangle)$ of haemoglobinopathic erythrocytes according to a χ^2-test ($p = 0.01$). The values for the critical shear stress as a function of the intermolecular ligand distance obtained for ICAM-1 were comparable between iHbAA and iHbAS. In contrast to CD36, a clear decrease of the critical pressure values was only prominent beyond $\langle d \rangle = 24$ nm.

The application of an empirical Hill function yielded the critical distance $\langle d \rangle_{\mathrm{crit}}$ characterizing the transition between binding and unbinding[127]:

$$P_{\mathrm{crit}}(\langle d \rangle) = P_{\mathrm{crit,min}} + \frac{P_{\mathrm{crit,max}} - P_{\mathrm{crit,min}}}{1 + \left(\frac{\langle d \rangle}{\langle d \rangle_{\mathrm{crit}}}\right)^{n}}, \qquad 3\text{-}10$$

where the maximum and minimum observed critical pressures are represented by $P_{\mathrm{crit,max}}$ and $P_{\mathrm{crit,min}}$, respectively. n denotes to the cooperative coefficient and describes the steepness of the transition. For CD36 the transition for infected wildtype erythrocytes occurred at $\langle d_{\mathrm{iHbAA,CD36}} \rangle_{\mathrm{crit}} \sim 33$ nm, while the transition for infected haemoglobinopathic erythrocytes was found already at $\langle d_{\mathrm{iHbAS,CD36}} \rangle_{\mathrm{crit}} \sim 21$ nm. The corresponding cooperativity coefficients of $n_{\mathrm{iHbAA,CD36}} \sim 3$ and $n_{\mathrm{iHbAS,CD36}} \sim 5$ suggest a cooperative nature of the CD36 to PfEMP1 interaction. In the case of ICAM-1 slightly higher values for the critical distances of $\langle d_{\mathrm{iHbAA,ICAM-1}} \rangle_{\mathrm{crit}} \sim 37$ nm and $\langle d_{\mathrm{iHbAS,ICAM-1}} \rangle_{\mathrm{crit}} \sim 33$ nm were obtained. The cooperative coefficient was significantly higher compared to CD36 reaching $n_{\mathrm{iHbAA,ICAM-1}} \sim 6$ and $n_{\mathrm{iHbAS,ICAM-1}} \sim 9$, respectively.

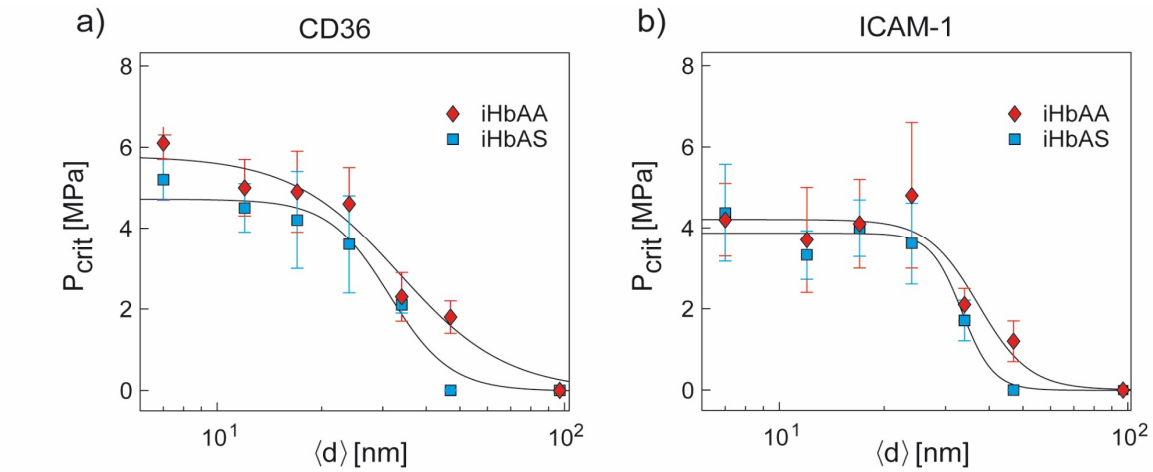

Figure 3.7 | Critical pressure of detachment P_{crit} as a function of mean intermolecular ligand distance $\langle d \rangle$. Data were fitted to equation (3-10) yielding the critical distance of the binding-unbinding transition $\langle d \rangle_{\mathrm{crit}}$ and the cooperativity coefficient n. Summarized data for infected HbAA and HbAS erythrocytes on (a) CD36 and (b) ICAM-1 functionalized bilayers.

3.2.3.1 Statistics

Data was obtained from at least three independent experiments using blood from at least 3 different donors both for HbAA and HbAS. If not stated otherwise the presented values correspond to mean value and standard deviation.

3.2.4 Discussion

Recently, the quantification of adhesion strength based on laser induced pressure waves has been successfully demonstrated for *P. falciparum* infected erythrocytes adhering to CSA functionalized bilayers and for human hematopoietic stem and progenitor cells adhering to SDF1α[83, 84]. In this study the extension of the observed adhesion area together with the

automated detection of cell positions allowed to probe the population characteristics with an unmatched cell statistics (>250 cells per single laser shot). Consequently, single data sets were well fitted assuming that the population characteristics follow a Gaussian distribution (Figure 3.6).

Firstly, the experiments were performed on infected wildtype erythrocytes to establish proper reference data and to gain insight into the different characteristics of the two receptor species CD36 and ICAM-1 and thereafter compared to infected haemoglobinopathic erythrocytes at corresponding experimental conditions.

Probing the adhesion strength of iHbAA as a function of mean intermolecular ligand distance of CD36 revealed a clear binding-unbinding transition at $\langle d_{\mathrm{iHbAA,CD36}}\rangle_{\mathrm{crit}} \sim 33$ nm, corresponding to a receptor density of $\sigma_{0,\mathrm{CD36}} \sim 1000 \times 10^6\ \mathrm{mm}^{-2}$. In comparison, the density of CD36 expressed on human dermal microvascular endothelial cells (HDMEC) is reported to be in the range of $\sigma_{0,\mathrm{CD36,HDMEC}} \sim 90 \times 10^6\ \mathrm{mm}^{-2}$ corresponding to a mean intermolecular ligand distance of $\langle d\rangle_{\mathrm{CD36,HDMEC}} \sim 110$ nm[128]. Even though this value is significantly higher compared to $\langle d_{\mathrm{iHbAA,CD36}}\rangle_{\mathrm{crit}} \sim 33$ nm, parasites are able to bind firmly to HDMECs[128]. A convincing explanation for this apparent discrepancy could be based on the results of force measurements performed by Davis *et al*. using atomic force microscopy. According to their results, the binding between HDMECs and infected erythrocytes significantly increases over time due to the parasites ability to "activate" HDMECs (termed "parasite induced cell activation"). In the case of CD36 the adaptor protein P130CAS is triggered resulting in the clustering of CD36 at the binding sites[129]. Although the resulting local CD36 densities are not known from their experiment, the data presented here indicate that the CD36 density needs to increase locally by a factor of ~10 to provide firm adhesion conditions. The increase in binding strength due to receptor clustering is additionally reflected in the observed cooperative binding character between CD36 and PfEMP1 expressed by a positive cooperativity factor of $n_{\mathrm{HbAA,CD36}} \sim 3$.

The experiments performed on infected haemoglobinopathic erythrocytes revealed ~15% lower critical pressures of detachment for all probed ligand distances compared with the corresponding data for infected HbAA erythrocytes. The binding-unbinding distance was found to be $\langle \mathrm{d}_{\mathrm{iHbAS,CD36}}\rangle_{\mathrm{crit}} \sim 21$ nm. In a first step, the morphological differences were taken into consideration, to help interpreting this result.

The mean knob diameter and knob densities for infected HbAA and HbAS erythrocytes were determined by scanning electron microscopy (Supporting Figure 8.4, the experiments and the measurement of knob diameter and knob densities were performed by Dr. Marek Cyrklaff, Center for Infectious Diseases, Heidelberg University Hospital). The mean knob diameters for infected HbAA and HbAS were found to be $d_{\mathrm{Knob,iHbAA}} = 72 \pm 21$ nm and $d_{\mathrm{Knob,iHbAS}} = 191 \pm 99$ nm, respectively, with corresponding knob densities of $\sigma_{\mathrm{Knob,iHbAA}} = 14 \pm 4\ \mu\mathrm{m}^{-2}$ and

$\sigma_{\mathrm{Knob,iHbAS}} = 3 \pm 2\ \mu\mathrm{m}^{-2}$. Assuming that knobs resemble half spheres, on can calculate the unit-less effective knob areas:

$$\varepsilon = 2\pi \left(\frac{d}{2}\right)^2 \sigma. \qquad 3\text{-}11$$

The effective knob area for iHbAS of $\varepsilon_{\mathrm{iHbAS}} = 0.16$ was significantly higher than the corresponding value obtained for iHbAA with $\varepsilon_{\mathrm{iHbAA}} = 0.12$. This results indicate, that the reported difference in the PfEMP1 expression level might be responsible for the reduced adhesion strength[49, 130]. Yet, to quantify the differences in expression level from the differences in adhesion strength alone, one would neglect the influence of several factors according to equation (3-1):

- Influence of differences in cell mechanics as characterized by the membrane tension σ and the membrane bending modulus κ (Chapter 4.1).
- Influence of the distribution and orientation of individual PfEMP1 in each single knob as characterized by an effective adhesion energy density per knob ω_{Knob}.
- Influence of the actual knob height on the interaction potential $V(h(\boldsymbol{x}))$ due to electrostatic shielding of the positively charged knobs[131] by the negatively charged glycocalix[132, 133].

Although this thesis sheds light on the first factor, the other factors demand further studies.

In a next step, the experiments were performed on ICAM-1 functionalized bilayers. In the case of infected wildtype erythrocytes a binding-unbinding transition was observed at $\langle d_{\mathrm{iHbAA,ICAM-1}} \rangle_{\mathrm{crit}} \sim 37$ nm. Following the consideration similar to the case of CD36, one needs to regard the mean intermolecular ligand distance of ICAM-1 on HDMECs, which can be calculated to be $\langle d \rangle_{\mathrm{ICAM-1,HDMEC}} \sim 440$ nm[128]. Recently, Lansche *et al*. reported an increase in surface expression of ICAM-1 induced by infected wildtype erythrocytes binding to HDMEC monolayers[46, 134]. This type of HDMEC activation is based on signal cascades via the nuclear factor κB[46, 135]. The presented results indicate that parasite induced cell activation could be the main reason to achieve firm adhesion to ICAM-1 and that a ligand distance of $\langle d_{\mathrm{iHbAA,ICAM-1}} \rangle_{\mathrm{crit}} \sim 37$ nm could represent the ICAM-1 surface expression level of an activated HDMEC. Similarly to CD36, the binding between ICAM-1 and PfEMP1 was found to be highly cooperative with $n_{\mathrm{HbAA,ICAM-1}} \sim 6$.

In contrast to CD36, the data obtained for infected haemoglobinopathic erythrocytes on ICAM-1 functionalized bilayers were comparable to the corresponding wildtype data. Following the line of arguments one might therefore conclude, that the discussed influencing factors of the adhesion strength, like the differences in cell mechanics or differences in knob morphology, are rather irrelevant for the ICAM-1 mediated adhesion under static conditions.

3.2.5 Summary

Cell detachment by pico-second laser induced pressure waves allowed to probe the adhesion strength with high cell statistics. The experiments on *P. falciparum* infected erythrocytes on CD36 and ICAM-1 functionalized solid-supported lipid bilayers revealed clear binding-unbinding transitions at low intermolecular ligand distances between of $\langle d \rangle \sim 21 - 37$ nm. The interaction between PfEMP1 and CD36/ICAM-1 displayed positive cooperative characteristics. The results indicate that the parasite mediated activation of HDMECs reported recently in literature, might be necessary to generate firm adhesion conditions by clustering of receptors (CD36) or by increased receptor expression levels (ICAM-1). Infected haemoglobinopathic erythrocytes exhibited a reduced binding strength to CD36 compared to infected wildtype erythrocytes. In contrast, the adhesion strength between iHbAA and iHbAS was comparable for ICAM-1.

3.3 Dynamic interaction of infected red blood cells

3.3.1 Background on cell adhesion and cell detachment as function of shear stress

Cell adhesion is mediated by noncovalent interactions between single receptor-ligand pairs. The corresponding interaction energy landscape displays a potential minima (Figure 3.8 a), corresponding to the bound state. Transition to the unbound state is possible by passing the transition-state energy barrier ΔE and associated with the bond dissociation rate $k_{\mathrm{off}}^{f=0}$ [136, 137]:

$$k_{\mathrm{off}}^{f=0} \sim e^{-\frac{\Delta E}{k_{\mathrm{B}}T}} \qquad 3\text{-}12$$

The application of an additional external force f leads to an decrease of the barrier height:

$$k_{\mathrm{off}}^{f\neq 0} \sim e^{-\frac{\Delta E - f x_c}{k_{\mathrm{B}}T}} = k_{\mathrm{off}}^{f=0} e^{\frac{f x_c}{k_{\mathrm{B}}T}} = k_{\mathrm{off}}^{f=0} e^{\frac{f}{f_c}}, \qquad 3\text{-}13$$

where x_c denotes to the distance between potential minima and transition-state barrier. f_c describes the characteristic force scale of the receptor-ligand pair. Equation (3-13) describes a "slip-bond" that becomes short-living when exposed to an external force (Figure 3.8 b).

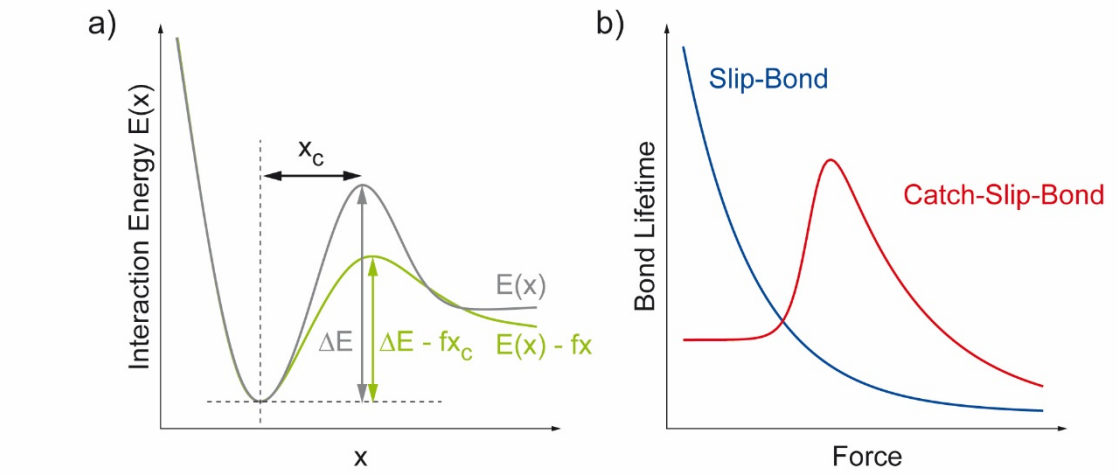

Figure 3.8 | Interaction energy and characteristics of ligand-receptor bonds. (a) Interaction energy landscape of a noncovalent receptor-ligand bond. Passing the energy barrier ΔE corresponds to the switching between the bound state (potential minimum) and the unbound state ($x \to \infty$). Due to the application of external stimuli in the form of the force f , the energy barrier decreases to $\Delta E - f x_c$ leading to an increase in the bond dissociation rates. (b) Bond lifetime of slip-bond (equation 3-12) and catch-slip-bond (equation 3-14) type of ligand-receptor bonds.

Another important type of bond is the "catch-slip-bond" that initially displays an increase in bond lifetime with increase of force. Yet, beyond a transition region, they are indistinguishable from slip-bonds (Figure 3.8 b). Evans *et al.* described them in their "two bounds states, two dissociation pathways model"[138]. In this model the ligand-receptor bond switches rapidly between two binding states I and II under equilibrium conditions. Binding states I and II are associated with a high but constant dissociation rate $k_{\mathrm{off}}^{\mathrm{I}}$ and a small but force dependent dissociation rate $k_{\mathrm{off}}^{\mathrm{II}}$, respectively[139]:

$$k_{\mathrm{off}}^{f\neq 0} = \frac{k_{\mathrm{off}}^{\mathrm{I}}\Phi_0 + k_{\mathrm{off}}^{\mathrm{II}}\, e^{f/f_{\mathrm{I}\leftrightarrow\mathrm{II}}} e^{f/f_c}}{\Phi_0 + e^{f/f_{\mathrm{I}\leftrightarrow\mathrm{II}}}}, \qquad 3\text{-}14$$

where $\Phi_0 = e^{\frac{\Delta E_{\mathrm{I}\leftrightarrow\mathrm{II}}}{k_{\mathrm{B}}T}}$ denotes to the equilibrium occupancy ratio between state I and II and $\Delta E_{\mathrm{I}\leftrightarrow\mathrm{II}}$ describes the small energy difference between them. The combined dissociation rate $k_{\mathrm{off}}^{f\neq 0}$ becomes dependent on the applied force f and the bond specific force scale $f_{\mathrm{I}\leftrightarrow\mathrm{II}}$.

3.3.2 Experimental realization

The adhesive behavior of uninfected and infected erythrocytes was quantified using parallel flow chambers combined with functionalized bilayers. The measurement chamber was prepared as previously described (Chapter 3.1.3) and connected to a high precision syringe pump (Harvard Apparatus, Holliston, USA), mounted onto an Axio Observer Z.1 inverse microscope (Zeiss, Oberkochen, Germany) equipped with a 40x/1.3 oil-immersion objective and an ORCA-Flash4.0 LT CMOS camera (Hamamatsu Photonics, Hamamatsu, Japan).

RPMI-BSA (Chapter 2.2) containing 10^6 cells/mL at 37°C was flushed through the chambers at different shear stresses covering the physiological shear stress range of $\tau = 0.03 - 0.3$ Pa characteristic for the post-capillary venules[140]. For each condition the total number of attached cells was recorded after 15 min of experiment time by taking 40 bright field images equivalent to a total observed area of ~4.4 mm^2.

Substrates, populated with iRBCs at 0.03 Pa were further used to determine the critical shear stress of detachment. For this purpose, the chambers were flushed with RPMI-BSA at stepwise increasing shear stresses, ranging from 0.05 to 4.0 Pa. Each shear stress condition was applied for 15 min, followed by the determination of the number of remaining cells for the same observed area size as previously mentioned.

3.3.3 Results

3.3.3.1 Binding of infected erythrocytes to CD36 and ICAM-1 under physiologic shear stresses

Functionalized bilayers in combination with parallel flow chambers allowed to quantify the adhesive capabilities of infected erythrocytes in terms of observed shear stress dependent binding events $N(\tau, \langle d \rangle)$ (Figure 3.9 a).

Between 0.03 Pa and 0.30 Pa the number of binding events $N(\tau, \langle d \rangle)$ decreased gradually for infected wildtype erythrocytes adhering to CD36 functionalized bilayers (Figure 3.9 b). Thereby, $N(\tau, \langle d \rangle)$ was significantly reduced from $N_{\mathrm{iHbAA,CD36}}(0.03\ \mathrm{Pa}, 11\ nm) = 185\ \mathrm{mL^{-1}mm^{-2}}$ to $N_{\mathrm{iHbAA,CD36}}(0.10\ \mathrm{Pa}, 11\ \mathrm{nm}) = 15\ \mathrm{mL^{-1}mm^{-2}}$.

The binding to ICAM-1 displayed similar characteristics (Figure 3.9 c) with $N(\tau, \langle d \rangle)$ decreasing gradually for higher shear stresses. Consequently, $N(\tau, \langle d \rangle)$ was reduced from $N_{\mathrm{iHbAA,ICAM-1}}(0.03\ \mathrm{Pa}, 11\ \mathrm{nm}) = 245\ \mathrm{mL^{-1}mm^{-2}}$ to $N_{\mathrm{iHbAA,ICAM-1}}(0.10\ \mathrm{Pa}, 11\ nm) = 38\ \mathrm{mL^{-1}mm^{-2}}$.

Probing $N(\tau, \langle d \rangle)$ at higher shear stresses typically yielded poor statistics with $N(0.03\ \text{Pa}, 11\ nm) \sim 0 - 2\text{mL}^{-1}\text{mm}^{-2}$ observed for both CD36 and ICAM-1.

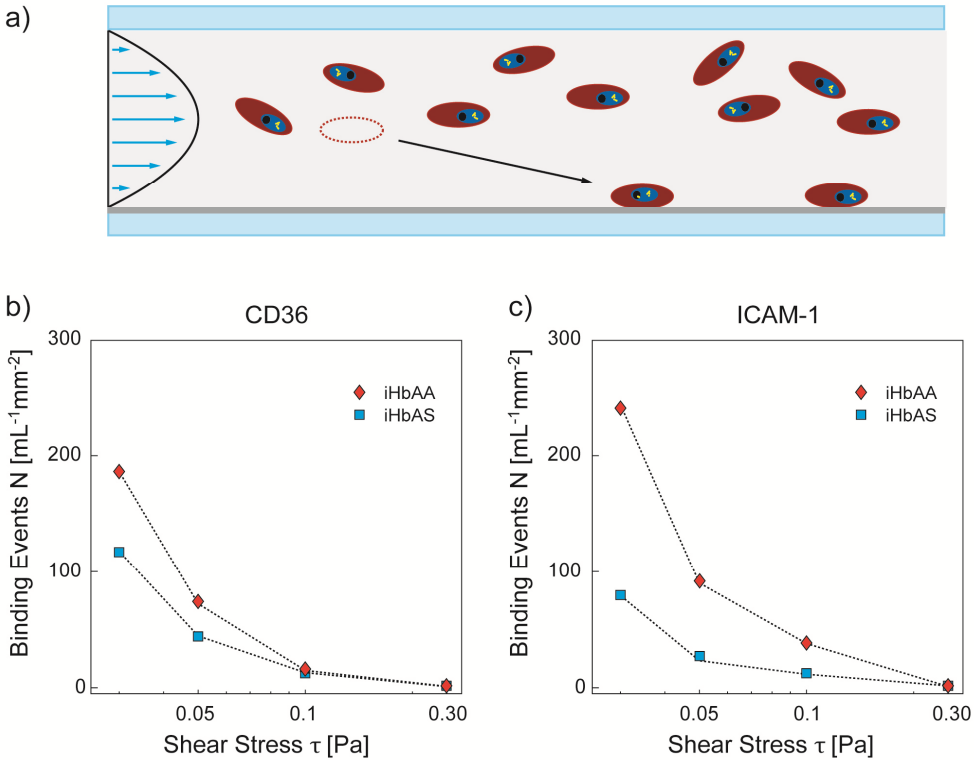

Figure 3.9 | Probing the adhesive capabilities of infected erythrocytes. (a) Experimental setup combining a parallel plate microfluidic chamber with a functionalized bilayer. (b) and (c) Slip bond behavior observed for both CD36 and ICAM-1 ($\langle d \rangle = 11$ nm) under physiological shear stresses. Infected haemoglobinopathic erythrocytes display strongly reduced binding capabilities.

The number of binding events $N(\tau)$ to CD36 and ICAM-1 of infected haemoglobinopathic erythrocytes displayed a similar shear dependent decrease (Figure 3.9 b, c). Yet, the $N(\tau)$ was significantly reduced, e.g. $N_{\text{iHbAS,CD36}}(\tau = 0.03\ \text{Pa}, \langle d \rangle = 11\ \text{nm}) = 117\ \text{mL}^{-1}\text{mm}^{-2}$ and $Ni_{\text{iHbAS,ICAM}-1}(\tau = 0.03\ \text{Pa}, \langle d \rangle = 11\ \text{nm}) = 79\ \text{mL}^{-1}\text{mm}^{-2}$, corresponding to a reduce of 37% and 68%, respectively, compared to data obtained for infected wildtype erythrocytes at the same conditions.

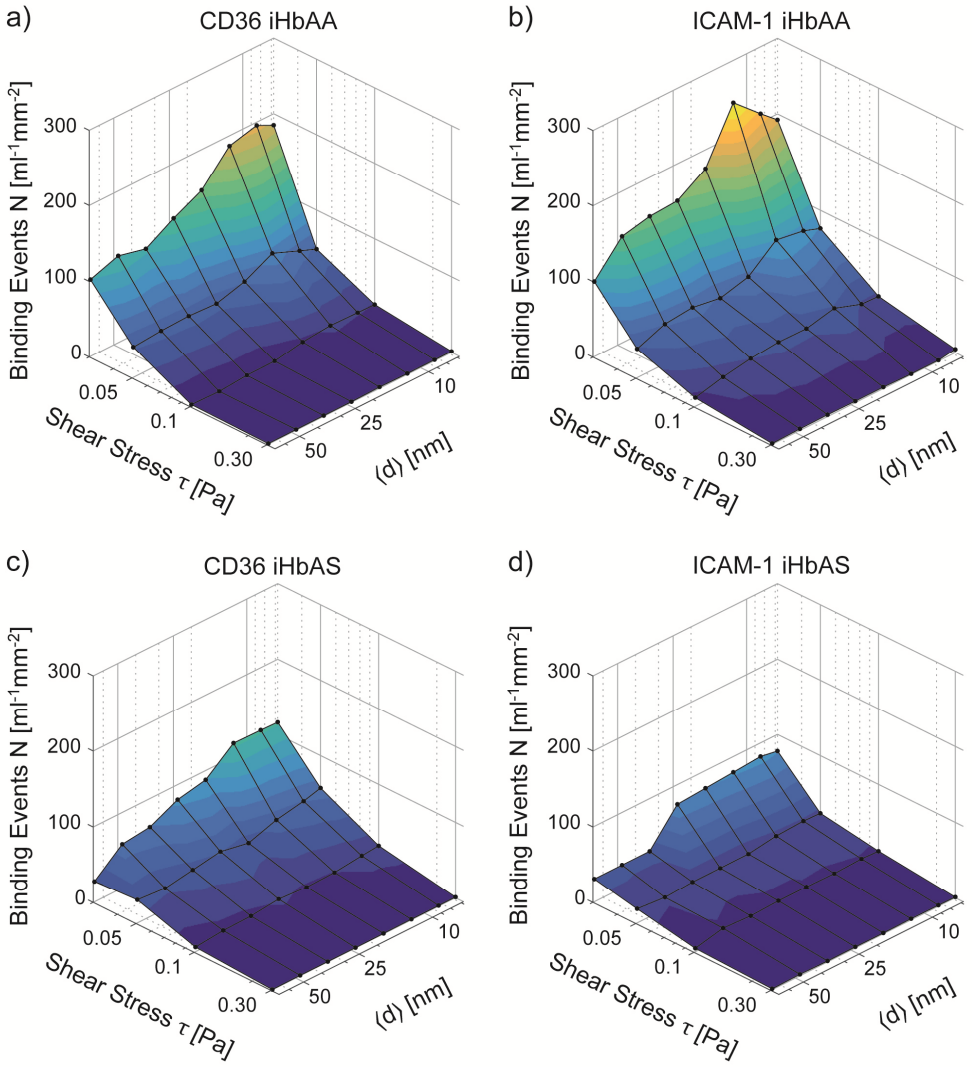

Figure 3.10 | Binding of infected erythrocytes to functionalized solid-supported lipid bilayers. Number of binding events N as a function of intermolecular ligand distance $\langle d \rangle$ and applied shear stress τ for infected wildtype (iHbAA) erythrocytes to (a) CD36 and (b) ICAM-1. (c) and (d) Corresponding data obtained for infected haemoglobinopathic (iHbAS) erythrocytes.

Further experiments were performed, varying the mean intermolecular ligand distances between $\langle d \rangle = 7 - 67$ nm. In fact, $N(\tau, \langle d \rangle = \text{const.})$ displayed the same shear depend binding for both receptor types and both blood types for all probed intermolecular ligand distances $\langle d \rangle$ (Figure 3.10). The influence of the ligand distance on $N(\tau = \text{const.}, \langle d \rangle)$ was most prominent at $\tau = 0.03$ Pa. Increasing the intermolecular ligand distance of CD36 or ICAM-1 to $\langle d \rangle = 67$ nm, resulted in a significant reduction in binding events of ~50% for iHbAA for both ligand species and >60% for iHbAS, compared to the corresponding values obtained for $\langle d \rangle = 11$ nm. Control experiments conducted with uninfected erythrocytes showed no binding events for CD36 nor ICAM-1 for both HbAA and HbAS.

3.3.3.2 Adhesion sustainability

The adhesion strength was quantified using the classical approach of exposing bound cells to stepwise increasing shear stress conditions. After the application of each shear stress

condition the number of adherent/remaining cells N_A was determined (Figure 3.11), yielding the critical pressure of detachment τ_{crit} following:

$$N_{\mathrm{A}}(\tau) = \frac{N_A^0}{2}\left(-\mathrm{erf}\left(\frac{\tau-\tau_{\mathrm{crit}}}{\sqrt{2}\sigma}\right)+1\right), \qquad 3\text{-}15$$

where N_A^0 denotes to the initial number of adherent cells and σ to the width of the underlying Gaussian distribution.

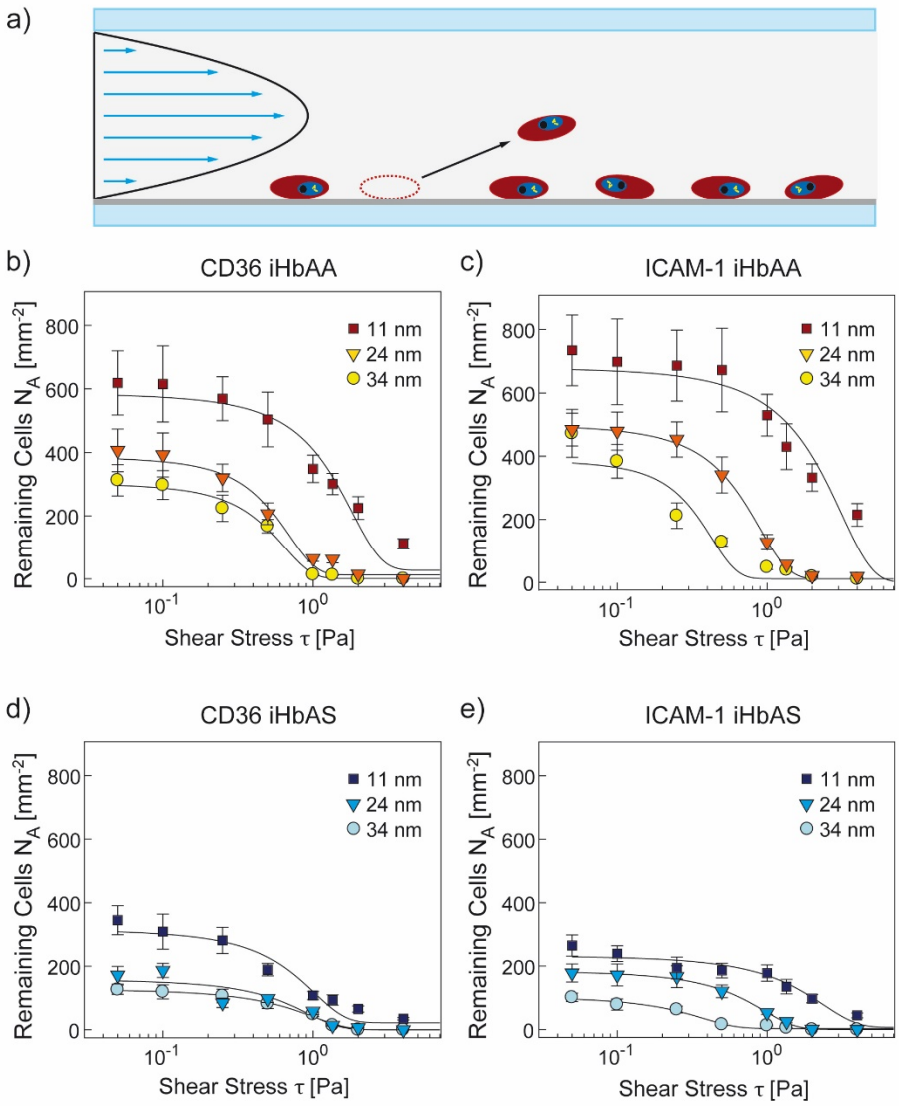

Figure 3.11 | Probing the adhesion strength of infected erythrocytes initally bound to CD36 and ICAM-1 functionalized bilayers at physioglical flow conditions. (a) Infected erythrocytes are detached under stepwise increasing shear stress conditions. (b) Representative data sets depicting the number of remaining infected wildtype erythrocytes as a function of the applied shear stress τ and the intermolecular ligand distance $\langle d \rangle$ for (b) CD36 and (c) ICAM-1. (d) and (e) Corresponding data sets for infected haemoglobinopathic erythrocytes. Data points were fitted to equation (3-15).

In a first step, experiments were performed for infected wildtype erythrocytes adhering to CD36 or ICAM-1 functionalized bilayers. The resulting detachment curves (Figure 3.11 b, c) all exhibited a clear transition from binding to unbinding as predicted by equation (3-15). The

critical shear stress values τ_{crit} decreased as a function of intermolecular ligand distance $\langle d \rangle$, reflected in a shift of the corresponding data curves to the left. Representative data obtained for infected haemoglobinopathic erythrocytes depicted similar characteristics (Figure 3.11 d, e).

Probing τ_{crit} as a function of mean intermolecular ligand distance between $\langle d \rangle = 7 - 67$ nm revealed clear differences between the ligand species CD36 and ICAM-1 independent of blood type (Figure 3.12). For CD36 the highest critical shear stresses were observed at $\langle d \rangle = 7$ nm for both infected wildtype and haemoglobinopathic erythrocytes with $\tau_{\mathrm{crit,iHbAA,CD36}} \sim 2$ Pa and $\tau_{\mathrm{crit,iHbAS,CD36}} \sim 0.8$ Pa, respectively. In clear contrast to this, the corresponding data for ICAM-1 exhibited a local maximum around $\langle d \rangle = 11$ nm with $\tau_{\mathrm{crit,iHbAA,ICAM-1}} \sim 2.2$ Pa and $\tau_{\mathrm{crit,iHbAS,ICAM-1}} \sim 1.2$ Pa, whereas lower intermolecular distances resulted in a significantly reduced binding strength.

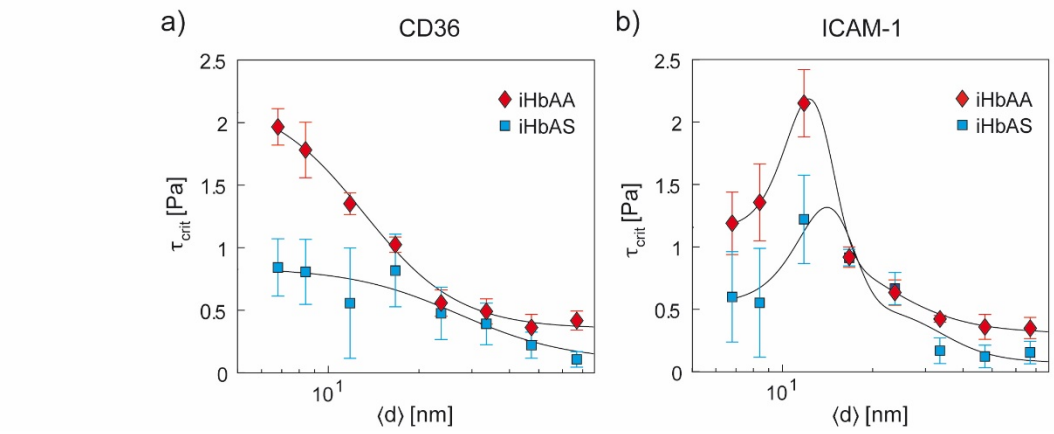

Figure 3.12 | Critical shear stress of detachment τ_{crit} as a function of mean intermolecular ligand distance $\langle d \rangle$. Summarized data for infected HbAA and HbAS erythrocytes on (a) CD36 and (b) ICAM-1 functionalized bilayers.

Yet, both CD36 and ICAM-1 share the general feature of reduced critical shear stresses observed for iHbAS compered to iHbAA (χ^2-test, $p = 0.01$). Thereby, iHbAS displayed very poor binding strengths at ligand distances of $\langle d \rangle = 67$ nm with 2 to 3 times reduced critical pressures in the range of only ~0.1 Pa, compared to iHbAA.

The critical distance describing the binding-unbinding transition $\langle d \rangle_{\mathrm{crit}}$ was derived from an empirical Hill function[127]:

$$\tau_{\mathrm{crit}}(\langle d \rangle) = \tau_{\mathrm{crit,min}} + \frac{\tau_{\mathrm{crit,max}} - \tau_{\mathrm{crit,min}}}{1 + \left(\frac{\langle d \rangle}{\langle d \rangle_{\mathrm{crit}}}\right)^{n}}, \qquad 3\text{-}16$$

where $\tau_{\mathrm{crit,max}}$ and $\tau_{\mathrm{crit,min}}$ denote to the maximum and minimum observed value of τ_{crit} and n to the cooperativity coefficient.

Although the experiments with infected wildtype erythrocytes iHbAA yielded significantly higher critical shear stresses for all intermolecular distances of CD36 compared to infected haemoglobinopathic erythrocytes, the binding-unbinding transition was found at a lower

value with $\langle d \rangle_{\mathrm{crit,iHbAA,CD36}} = 13$ nm against $\langle d \rangle_{\mathrm{crit,iHbAS,CD36}} = 26$ nm. Yet, the cooperative factors were comparable with $n_{\mathrm{iHbAA,CD36}} = 2.9$ and $n_{\mathrm{iHbAS,CD36}} = 2.5$.

Equation (3-16) cannot capture local maxima characteristics as displayed for ICAM-1. Due to the poor resolution in $\langle d \rangle$, resulting in a single data point covering the maxima region, double sigmoidal curve approaches did not converge. To capture the course of the curve, a single Gaussian was added to equation (3-16). Thereafter, the binding-unbinding transitions were found at $\langle d \rangle_{\mathrm{crit,iHbAA,ICAM-1}} = 20$ nm and $\langle d \rangle_{\mathrm{crit,iHbAS,ICAM-1}} = 32$ nm for iHbAA and iHbAS, respectively. The cooperativity factors were comparable with $n_{\mathrm{iHbAA,ICAM-1}} = 4.3$ and $n_{\mathrm{iHbAS,ICAM-1}} = 5.0$. From the single Gaussian, the maxima for the critical shear stress of detachment were found at 12 nm for iHbAA and 14 nm for iHbAS.

3.3.3.3 Statistics

Data was obtained from at least three independent experiments using blood from at least 3 different donors both for HbAA and HbAS. If not stated otherwise the presented values correspond to mean value and standard deviation.

3.3.4 Discussion

The capability of *P. falciparum* infected erythrocytes to adhere to human dermal microvascular endothelial cells (HDMEC) is vital for the parasites proliferation by avoiding splenic clearance[36, 141]. Functionalized solid-supported lipid bilayers in combination with parallel flow chambers provide a sophisticated *in vitro* model to study the specific role of single receptor species under physiological shear stress conditions[84].

Infected erythrocytes were found to bind to CD36 and ICAM-1 in a shear dependent manner, suggesting slip-bond characteristics for the CD36-PfEMP1 and the ICAM-1-PfEMP1 ligand pairs. This seems to coincide with previous studies based on parallel flow chambers using plastic substrates coated with purified CD36 and ICAM-1 and on studies based on the binding to microvascular endothelial cells expressing both receptor species[134, 142, 143]. However, it should be noted that recent studies based on force measurement using AFM, revealed catch-slip-bond characteristics for ICAM-1 – PfEMP1 at shear stresses below 0.045 Pa[144].

An increase in the mean intermolecular ligand distance lead to a decrease in the number of binding events. This effect was most prominent at 0.03 Pa, where the change from $\langle d \rangle = 11$ nm to $\langle d \rangle = 67$ nm was accompanied by a decrease of binding events by roughly 50% for both CD36 and ICAM-1. Interestingly, the number of binding events at $\langle d \rangle = 67$ nm did not reach zero, indicating that binding at low shear rates might also be possible for intermolecular distances not investigated in this study.

The number of observed binding events was strongly reduced for infected haemoglobinopathic erythrocytes (iHbAS) compared to infected wildtype erythrocytes (iHbAA) independent of the ligand species. This finding is supported by previous studies investigating the binding to microvascular endothelial cells[78, 79, 134]. Since the effective knob

area was found to be ~30% larger for iHbAS compared to iHbAA (Chapter 3.2.4, Supporting Figure 8.4), the reduction in binding events could confirm a reduced expression of PfEMP1. Additionally, the abnormal knob distribution and differences in cell mechanics might contribute negatively to the binding capabilities of infected haemoglobinopathic erythrocytes[145].

For carries of the sickle trait, who suffer from malaria, the reduced binding probability indeed could lead to an overall delayed progression of the infection, since a higher fraction of infected erythrocytes would be exposed to splenic clearance. Indeed, the number of freely circulating infected erythrocytes was reported to be higher in patients carrying HbAS[146].

Naturally, the number of freely circulating infected erythrocytes is reduced by binding events to endothelial cells, but will further increase once an infected cell is prematurely (before reaching to the schizont stage) detached. Therefore, the adhesion strength was quantified based on the critical shear stress of detachment, obtained by stepwise increasing shear stress conditions.

The experiments revealed distinct differences between the binding strength to CD36 and ICAM-1 as a function of their respective intermolecular ligand distance. While the adhesion strength of CD36 monotonically increased by decreasing the intermolecular ligand distances, ICAM-1 displayed a maximum around 12 nm. Smaller ligand distances led to a significant decrease in the binding strength, which could be attributed to steric hindrance of the receptor. Interestingly, the binding site of ICAM-1 to PfEMP1 was found to be shear dependent[147]. Chakravorty *et al*. found that mutations of ICAM-1 at the side of the protein lead to significant reduction in cytoadherence under flow, while mutations at the top did influence the binding strength mainly under static conditions[147]. This finding would support the explanation of steric hindrance due to the high ligand density. Furthermore, it could also explain, why such a decrease in adhesion strength for ICAM-1 at low intermolecular ligand distances was not prominent under static conditions (Chapter 3.2.4).

The majority of infected wildtype erythrocytes sustained firm adhesion under naturally occurring shear stresses for both CD36 and ICAM-1 for the intermolecular distance range between $\langle d \rangle = 7 - 67$ nm. In contrast, the reduced binding strength of the majority of iHbAS demanded for ligand distances below ~35 nm to be able to sustain binding to CD36 and ICAM-1 functionalized bilayers.

Although the intermolecular ligand distance range was not extended above 67 nm, the results indicate that the binding of iHbAS to HDMECs expressing CD36 and ICAM-1, with reported ligand distances of $\langle d \rangle_{\mathrm{CD36,HDMEC}} \sim 110$ nm and $\langle d \rangle_{\mathrm{ICAM-1,HDMEC}} \sim 440$ nm[128], might be very weak and therefore unable to sustain natural occurring shear stresses long enough to pass through the parasite maturation process.

Ligand distances of CD36 and ICAM-1 below 17 nm allowed a fraction of adherent iHbAA to sustain shear stresses beyond the maximum applied shear stress of 4 Pa, corresponding to

values measured for the human abdominal aorta[148]. Surprisingly, a small number of iHbAS termed as “heavy binders” sustained firm adhesion under the same conditions. Previous studies demonstrated that a small fraction of iHbAS display similar knob sizes and amounts of expressed PfEMP1 as in iHbAA[149]. Yet, the performed experiments cannot answer the question, if this phenotype is indeed represented among the “heavy binders” let alone the major fraction.

Independently, such a population of “heavy-binders” would be the dominant phenotype in malaria patients after several intraerythrocytic multiplication cycles, thereby increasing the average adhesion strength of the parasite population. This might explain, why *in vivo* studies revealed that HbAA and HbAS children can display comparable parasitemia levels[78, 150].

3.3.5 Summary

Probing the dynamic interaction of infected erythrocytes with solid-supported lipid bilayers functionalized with CD36 or ICAM-1 revealed clear difference between infected wildtype and infected haemoglobinopathic erythrocytes, while both ligand species displayed similar characteristics.

In the physiological relevant shear stress range between 0.03 and 0.3 Pa, the number of binding events was strongly reduced for iHbAS compared to iHbAA. Additionally, the corresponding critical shear stress of detachment was found to be significantly lower for iHbAS, with values below 0.3 Pa for intermolecular ligand distances beyond ~35 nm. Both findings could lead to a delayed increase in parasitemia levels in carries of the sickle-cell trait, due to enhanced splenic clearance of infected erythrocytes, which in turn would result in milder symptoms.

The experiments performed at intermolecular ligand distances below 17 nm, revealed a subpopulation of “heavy binders” in iHbAS, that displayed similar binding characteristics as iHbAA, and are capable of sustaining shear stress conditions only to be found in the human abdominal aorta. This subpopulation might be responsible for comparable parasitemia levels found in children carrying HbAS and HbAA, during malaria infection.

3.4 Quantification of cell adhesion by micro interferometry

3.4.1 Background of reflection interference contrast microscopy

Reflection Interference Contrast Microscopy (RICM) is a label and contact free method to determine the geometry of a variety of objects in close proximity to a planar surface[151]. Thereby, typical objects of interest consist of thin films of liquid, giant unilamellar vesicles, micrometer-sized spherical beads or living cells[152, 153].

In a generic RICM setup an object is homogeneously illuminated by monochromatic light (Figure 3.13 a). The resulting images represent the superposition of rays reflected from different interfaces characterized by their respective refractive indices (Figure 3.13 b). Under the assumption of a quasi-point source the recorded intensity I at position (x, y) relates to the time average of the local electrical field[154]:

$$I(x,y) = \langle \boldsymbol{E}^2 \rangle_t, \tag{3-17}$$

$$\boldsymbol{E}(\boldsymbol{r},t) = E(\boldsymbol{r}) e^{i\varphi(\boldsymbol{r})} e^{i\omega t}. \tag{3-18}$$

Where $\varphi(\boldsymbol{r})$ is the phase function. In reality the light source is extended and can be regarded as composition of point sources. Metal-halide light sources are often used as light sources in RICM. Because of the low spatial coherence, the time averaged intensity can be described directly as[155]:

$$I(x,y) = \left\langle \frac{\int \boldsymbol{E}^* \boldsymbol{E} \mathrm{d}\Omega}{\int \mathrm{d}\Omega} \right\rangle_t, \tag{3-19}$$

where $\Omega = (\theta, \varphi)$ denotes the polar angles of incidence at position (x, y). From the low spatial coherence one can assume that only rays from a single point source can interfere. The electric field vector $\boldsymbol{E} = \sum_i \boldsymbol{E}_{r,i}$ is derived as a summation over all electric field vectors of all reflected rays. The corresponding amplitudes can be expressed as functions of the amplitude of the incident light E_0 (Figure 3.13 b):

$$E = r_{01} E_0 + (1 - r_{01}^2) r_{12} E_0 e^{-i\frac{2\pi}{\lambda}\Delta_1} + \cdots + \tag{3-20}$$

$$= R E_0, \tag{3-21}$$

where r_{ij} is the reflection coefficient describing the interface between layers i and j. Please note that the transmission coefficient t_{ij} is replaced by $\left(1 - r_{ij}^2\right) = {t_{ij}}^2$. Furthermore, the characteristic wavelength of illumination denotes to λ and the differences in optical path length to Δ_i. The summation yields the effective reflection coefficient R.

If the refractive indices n_i and n_j of adjacent layers are known, the corresponding reflection coefficients in perpendicular (s) and parallel (p) polarization can be directly derived from Fresnel equations:

$$r_{ij}^{s}(\theta) = \frac{n_i \cos\theta_i - n_j \cos\theta_j}{n_i \cos\theta_i + n_j \cos\theta_j}, \quad 3\text{-}22$$

$$r_{ij}^{p}(\theta) = \frac{n_j \cos\theta_i - n_i \cos\theta_j}{n_j \cos\theta_i + n_i \cos\theta_j}. \quad 3\text{-}23$$

θ is the angle between the rays and the normal to the interface (i, j).

For a multilayer system under quasi-perpendicular illumination and with negligible multi reflection events, the effective reflection coefficient R can be described as:

$$R = r_{01} + \sum_{i=1}^{m}\left[\prod_{s=1}^{i}\left(1 - r_{s-1,s}^{2}\right)e^{-i\frac{2\pi}{\lambda}\Delta_s}\right] r_{i,i+1}, \quad 3\text{-}24$$

$$I(x,y) = R^{*}RE_0^2 = R^{*}RI_0, \quad 3\text{-}25$$

with m denoting the number of layers (substrate $m = 0$). From equation (3-24) one can see that the interference patterns are directly dependent on the traversed layers characterized by their thicknesses d_i and refractive indices n_i:

$$\Delta_i = 2n_i d_i(x,y). \quad 3\text{-}26$$

In many practical applications the characteristics of all but one layer are independent of the position (x, y). From the presented example of a bead close to the substrate (Figure 3.13 b) one can see that only the local object height $h(x, y)$ determines the corresponding layer thickness $\Delta_{\mathrm{Medium}}(x, y)$. Maxima of the effective reflection coefficient R can be observed under the condition:

$$\sum \Delta_i = k\lambda, k = 1, \ldots, \mathrm{n} \quad 3\text{-}27$$

Since, condition 3-27 is fulfilled several times in the case of giant unilamellar vesicles or a spherical bead close to the substrate the RICM image is characterized by the appearance of the well-known Newton fringes (Figure 3.13 c). Please note, that RICM imaging in principle allows the reconstruction of the object shape for such a simple case, if thickness and refractive indices of all traversed layers are known. Yet, the absolute height above the substrate can only be determined utilizing a second wavelength in parallel[156].

A major improvement of the image quality was achieved by Ploem in the 1975 by introducing the Antiflex technique[157] (Figure 3.13 a). In a first step, the incoming rays are linear polarized by inserting a polarizer behind the field stop. After the propagation through the $\lambda/4$-plate inside the Antiflex objective the rays end up with circular polarization. Since the reflection between two layers i, j typically is accompanied by a phase shift of π for the two electrical field components if $n_j > n_i$, reflected rays passing through the objective a second time will end up linear polarized again. Yet, the phase shift causes the linear polarization to be perpendicular to the initial linear polarization. By adding an additional analyzer in front of the camera, one can therefore block the majority of stray lights and record light originating from reflection events.

The addition of a collector lense, an illumination aperture and a field stop allows to achieve Köhler illumination conditions[158] which are necessary to adapt the RICM setup to the objects of interest (Figure 3.13 a). Both the reconstruction of large objects above the substrate and the determination of objects with a large distances to the substrate require large depths of field and therefore rely on a minimization of the illumination aperture $INA = n \sin \alpha$ to create a point like source. Full spatial coherence is limited to an illumination area with a diameter of d[159]:

$$d \leq \frac{0.16\lambda}{n \sin \alpha} = \frac{0.16\lambda}{INA}. \qquad 3\text{-}28$$

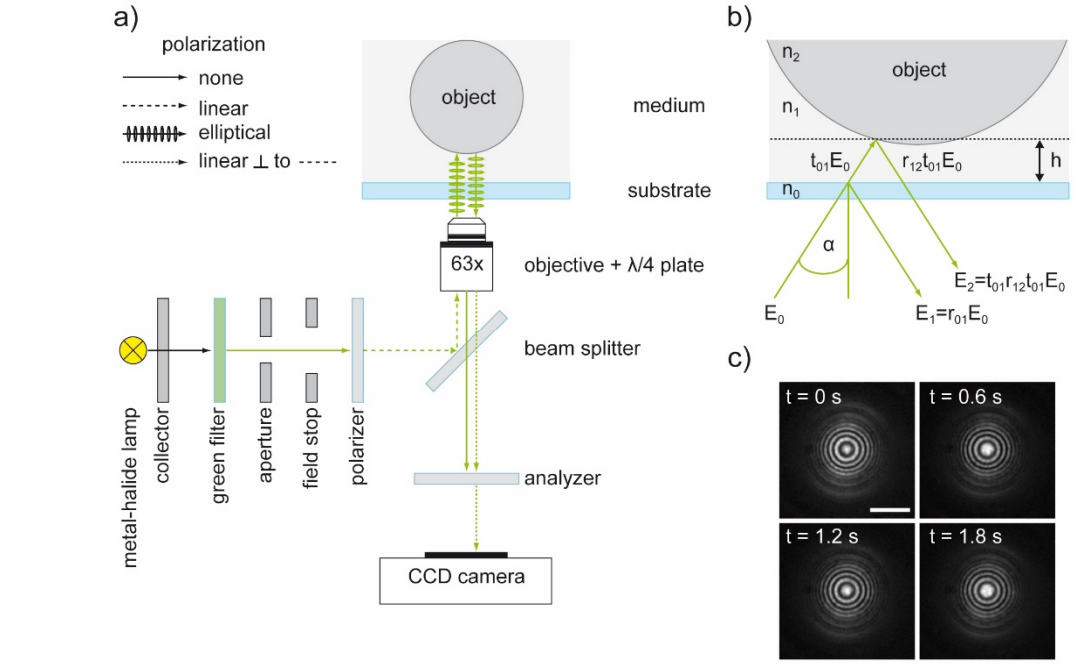

Figure 3.13 | Experimental setup for reflection interference contrast microscopy (RICM). (a) Sample objects are illuminated under quasi-normal incidence by linear polarized, quasi-monochromatic light ($\lambda = 546 \pm 10$ nm) originating from a metal-halide lamp. Incident rays are reflected at the different interfaces depended on their refractive index differences. Reflected light is collected by a CCD camera, while stray lights are largely suppressed using an additional analyzer. (b) Differences in the optical pathway as a function of object height *h* can result in constructive and destructive interference. (c) RICM raw data of a latex particle fluctuating above a substrate. The changes in height over time result in a shift of maxima and minima position, clearly visible as a shift in the so called Newton fringe pattern.

In the case of living cells, the direct interface between the cell membrane and the substrate is often of more interest. In such cases a large INA yields better images, due to the restriction of the depth of field. Thereby, signals from upper layers are suppressed due to the limited coherence length. Additionally it should be noted that the change from low INA to high INA and therefore the change from coherent to incoherent condition also directly impacts the lateral resolution with the respective resolution limits δ following the Rayleigh criterion[159]:

$$\delta_{\text{incoherent}} = \frac{0.61\lambda}{NA} = 266\ \mu\text{m} \qquad \lambda = 546\ \text{nm}, \text{NA} = 1.25 \qquad 3\text{-}29$$

$$\delta_{\text{coherent}} = \frac{0.82\lambda}{NA} = 358\ \mu\text{m} \qquad \lambda = 546\ \text{nm}, \text{NA} = 1.25 \tag{3-30}$$

3.4.2 Experimental realization

3.4.2.1 RICM microscopy

The RICM imaging setup consisted of an Axio Observer Z1 inverted microscope augmented with a mercury-vapor lamp (HXP 120 V, LEJ, Jena, Germany) and a 63x/1.25 Antiflex oil-immersion objective with a built in $\lambda/4$-plate similar to previously reported setups[83, 160]. Due to the insertion of a green filter ($\lambda = 546 \pm 10\,nm$) the light was regarded as quasi-monochromatic since the differences in optical pathways were below $\Delta_S \ll \lambda^2/\Delta\lambda \approx 30$ µm. Schematics resemble Figure 3.13 c). RICM under flow conditions (3.3.2) was performed after 10 min of the respective wash out period up to a shear stress of 1.0 Pa. For each shear stress condition an image sequence consisting of 100 consecutive images with an integration time of 30 ms was collected for at least three different positions.

3.4.2.2 Analysis of RICM image sequences

The process of RICM image sequence analysis is depicted in Figure 3.14 (I-VII). (I-III) In a first step, the image sequence was checked for completeness to exclude detached cells or cells with high lateral drift from the analysis. (IV) For each frame the RICM raw image intensity was normalized to the mean intensity level derived from the cell free area applying a background mask:

$$I_{\text{norm}}(x,y,t) = \frac{I(x,y,t)}{\langle I(x,y,t)\rangle_{\text{Bgr}}} \tag{3-31}$$

The mean contact area or "area of close proximity" was determined from the gradient image of the time averaged intensity image (V). RICM imaging only allows to correctly convert intensity into height, if all layer thicknesses and their respective refractive indices are known. Unfortunately, the cytosolic refractive index is rendered highly inhomogeneous by the infection of *P. falciparum* making it a unknown function of the lateral position x, y[161]. (VI) Instead, the mean square amplitude of intensity was derived over all frames:

$$MSA(x,y) = \frac{1}{n_{\text{frames}}} \sum_{1}^{n_{\text{frames}}} \left(\langle I_{\text{norm}}(x,y,t)\rangle_t - I_{\text{norm}}(x,y,t)\right)^2. \tag{3-32}$$

(VII) Under the assumption that small changes in intensity ΔI_{norm} scale linearly with changes in height Δh, the intensity mean square amplitude was utilized to define an area of adhesion $A_{Adhesion}$ as:

$$A_{Adhesion} = \sum_{1\le x\le x_{\max},1\le y\le y_{\max}}^{MSA(x,y)\le MSA_T} 1. \tag{3-33}$$

By categorizing a pixel as adherent if the corresponding MSA was below an upper threshold limit MSA_T. MSA_T was determined from adherent cells at high shear stress conditions and set

to $MSA_T = 0.02$. In the case of infected erythrocytes, the MSA in the region below the parasite digestive vacuole incorrectly indicated non-adhesion area conditions, since the lateral movement of the heme crystals naturally created large intensity fluctuations. Therefore, pixels inside a manually added circular mask were not subjected to the analysis (c and d, VII). The loss in adhesion area was corrected afterwards under the assumption that the ratio of adhesion to non-adhesion area was homogeneous throughout the cell contact area.

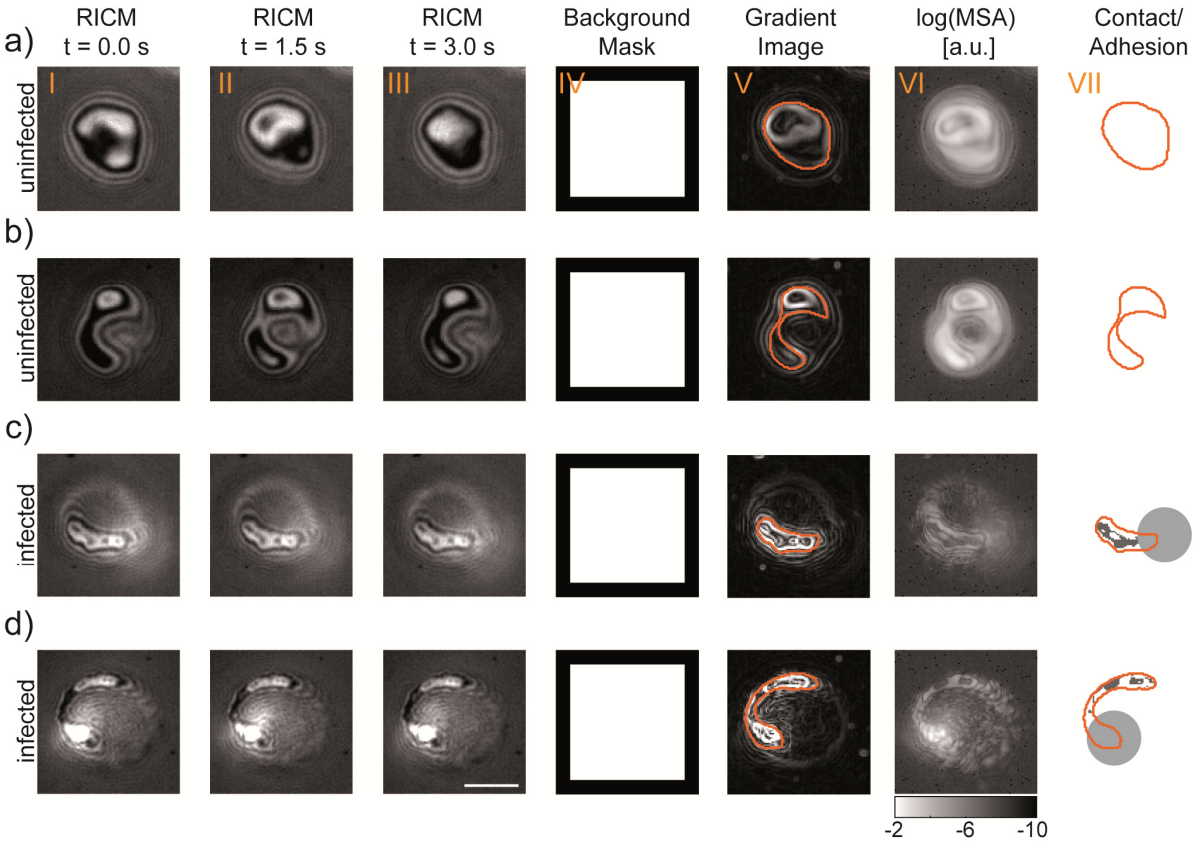

Figure 3.14 | Determination of the contact area and the area of adhesion based on RICM image sequences. (a) and (b) RICM images for different time points (I-III) of uninfected erythrocytes incubated for 30 minutes on a supported bilayer functionalized with CD36 ($\langle d \rangle = 11$ nm). Black region (IV) masks a cell free background area used to normalize the intensity. (V) The area of close contact (orange line) was derived from the intensity gradient of the time average of the image sequence. (VI) The mean square amplitude (MSA) of the intensity is used to identify the area of adhesion based on an threshold value MSD_T. (VII) No area of adhesion for uninfected erythrocytes. (c) and (d) analogue procedure for RICM image sequences obtained for infected erythrocytes at trophozoite stage under comparable experimental conditions. (VII) The adhesion area is depicted in dark grey. The influence of the moving haemozoin inside the parasite digestive vacuole was corrected for, manually, using a circular shade (light grey). Scale bar, 4 µm.

3.4.3 Results

Reflection interference contrast microscopy (RICM) was performed for infected erythrocytes binding to CD36 or ICAM-1 functionalized solid-supported bilayers. RICM image sequences allowed to calculate the area of close cell to substrate contact $\langle A \rangle_{\mathrm{Contact}}$ and the subarea, where the cells displayed firm adhesion $\langle A \rangle_{\mathrm{Adhesion}}$ to the substrate. Both physical quantities were determined for infected erythrocytes as a function of applied shear stress between $\tau = 0.05 - 1.00$ Pa. Probing higher shear stress conditions resulted in micro-level vibrations of

the experimental chamber, leading to the loss of focus during the recording of the image sequence.

The characteristic shape of the contact area changed from partially closed circular rings at $\tau = 0.05$ to drop-like shapes at $\tau = 1.00$ (Figure 3.15), accompanied by a monotonic increase of the size of the contact area. Thereby the average contact area of an infected erythrocyte increased significantly from $\langle A(\tau = 0.05\ \text{Pa})\rangle_{\text{Contact,CD36\&ICAM}-1} \sim 10\mu\text{m}^2$ to $\langle A(\tau = 1.00\ \text{Pa})\rangle_{\text{Contact,CD36\&ICAM}-1} \sim 25\ \mu\text{m}^2$. The data sets for CD36 and ICAM-1 where comparably for both ligand species (Figure 3.16 a, b, χ^2-test, $p = 0.01$).

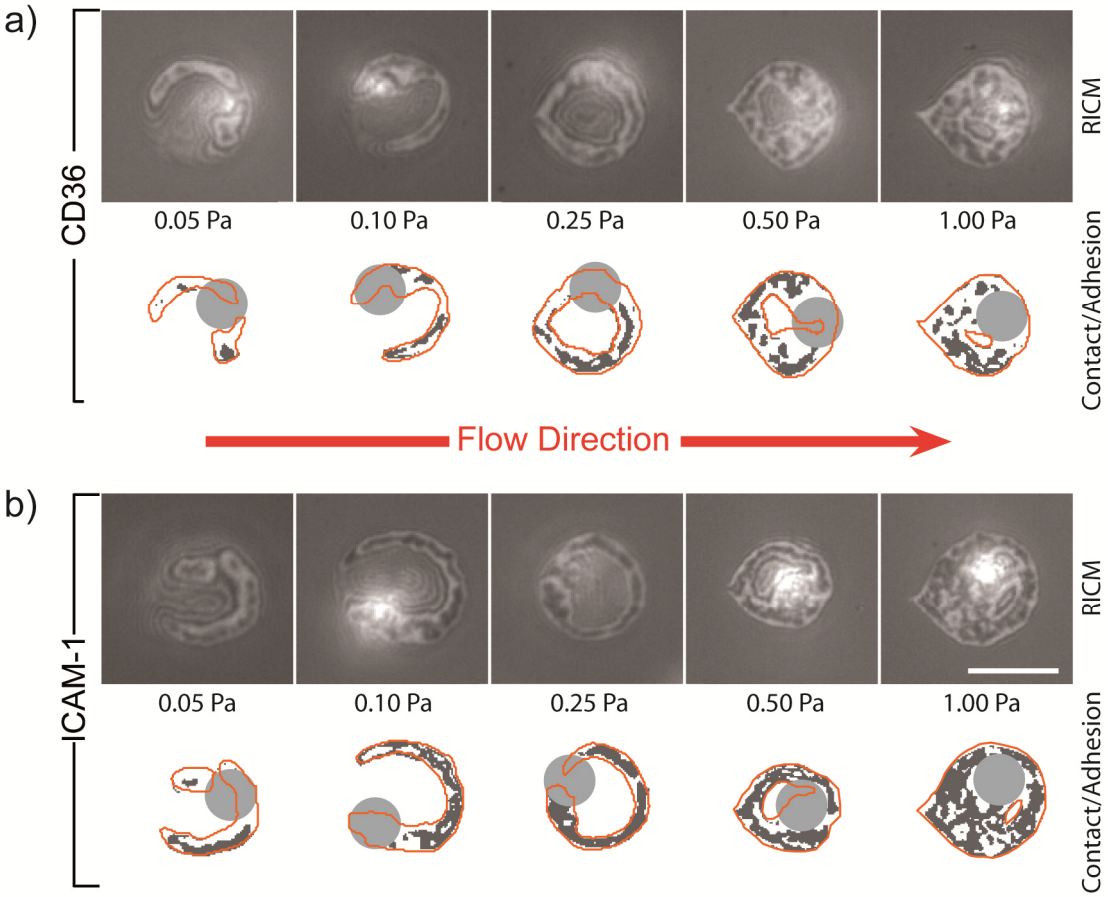

Figure 3.15 | Growth of adhesion area of infected erythrocytes as a function of applied shear stress. (a) Reflection interference contrast microscopy raw images (upper panel) of representative infected wildtype erythrocytes at the trophozoite stage of infection on bilayers functionalized with CD36 ($\langle d\rangle = 11$ nm). The calculated contact area (orange line), area of adhesion (dark grey) and the applied masking of the haemozoin distorted region (grey circle). (b) Corresponding data sets for bilayers functionalized with ICAM-1 ($\langle d\rangle = 11$ nm). Scale bar, 4 µm.

The data were fitted under the assumption of a limited shear dependent adhesion area A_{Max} of $\langle A\rangle_{\text{Contact}}$ and $\langle A\rangle_{\text{Adhesion}}$:

$$\langle A(\tau)\rangle = \langle A\rangle_{\text{Max}} - \langle A\rangle_{\text{Max}} e^{-k\tau} + \langle A(0)\rangle, \qquad 3\text{-}34$$

where $\langle A(0)\rangle$ denotes to the average initial contact/adhesion area (Figure 3.16 a, b). The corresponding fits indicate, that the maximum of $\langle A\rangle_{\mathrm{Contact}}$ might already be reached at $\tau = 1.00$ Pa, for both CD36 and ICAM-1.

Interestingly, the parallel increase in adhesion area $\langle A\rangle_{\mathrm{Adhesion}}$was significantly different between the two ligand species. Although an average adhesion area $\langle A(\tau = 0.05\ \mathrm{Pa})\rangle_{\mathrm{Adhesion,CD36\&ICAM-1}} \sim 4\ \mu m^2$ was found for both CD36 and ICAM-1 at the initial shear stress condition, the shear dependent increase of the adhesion area was more prominent for ICAM-1 leading to $\langle A(\tau = 1.00\ \mathrm{Pa})\rangle_{\mathrm{Adhesion,ICAM-1}} \sim 12\ \mu m^2$ over $\langle A(\tau = 1.00\ \mathrm{Pa})\rangle_{\mathrm{Adhesion,CD36}} \sim 7.5\ \mu m^2$ for CD36 (χ^2-test, $p = 0.01$). Further ligand specific characteristics were revealed, by correlating the average adhesion area $\langle A\rangle_{\mathrm{Adhesion}}$ and the average intensity mean square amplitude $\langle MSA\rangle$ (Figure 3.16 c, d). The average $\langle MSA\rangle_{\mathrm{CD36}}$ calculated for the adhesion area of iHbAA to CD36 was significantly higher compared to the corresponding values $\langle MSA\rangle_{\mathrm{ICAM-1}}$ obtained for ICAM-1 (χ^2-test, $p = 0.01$). Additionally, the negative correlation between $\langle A\rangle_{\mathrm{Adhesion}}$ and $\langle MSA\rangle$ was found to be very weak for CD36 (Pearson correlation coefficient $r = -0.36$) compared to ICAM-1 (Pearson correlation coefficient $r = -0.96$).

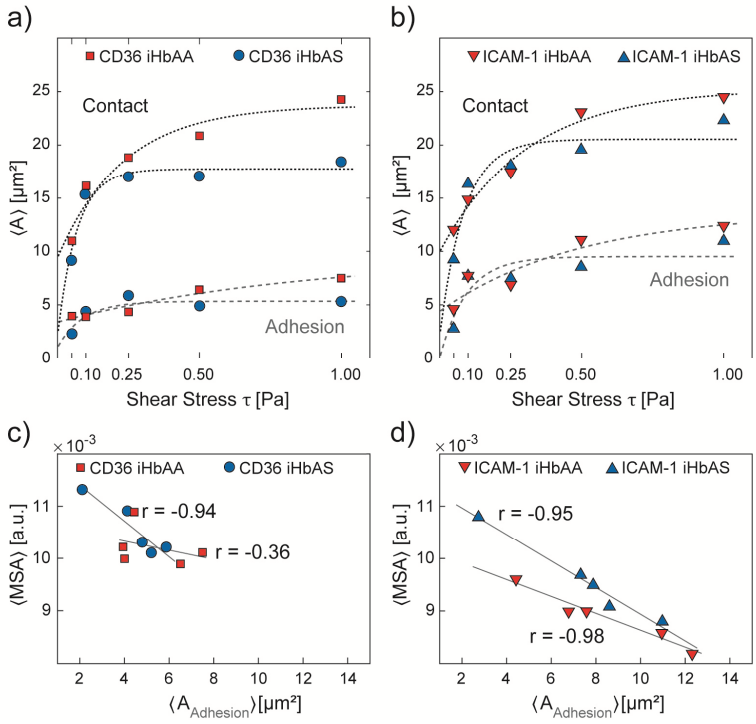

Figure 3.16 | RICM results for infected wildtype HbAA and infected haemoglobinopathic HbAS erythrocytes adhering to CD36 and ICAM-1 functionalized bilayers ($\langle d\rangle = 11\ nm$). Increase in average contact area $\langle A\rangle_{\mathrm{Contact}}$ and average adhesion area $\langle A\rangle_{\mathrm{Adhesion}}$ as function of applied shear stress τ for (a) CD36 and (b) ICAM-1. (c) and (d) Corresponding Pearson correlation coefficients r for the average mean square amplitude as a function of the average adhesion area.

Thereafter, the experiments were performed for infected haemoglobinopathic erythrocytes. Similar to iHbAA, the contact area $\langle A\rangle_{\mathrm{Contact}}$ and the adhesion area $\langle A\rangle_{\mathrm{Adhesion}}$ strongly increased as a function of applied shear stress (Figure 3.16 a, b). Yet, in the case of binding to

CD36 the calculated adhesion areas were significantly reduced compared to the corresponding data obtained for iHbAA (χ^2-test, $p = 0.01$), e.g. $\langle A(\tau = 1.00\ \text{Pa})\rangle_{\text{Contact,CD36}} \sim 18\ \mu\text{m}^2$ corresponds to a decrease by 28%. Consequently, the associated adhesion areas did level off at $\langle A(\tau = 1.00\ \text{Pa})\rangle_{\text{Adhesion,CD36}} \sim 5\ \mu\text{m}^2$, ~30% below the value obtained for iHbAA. In contrast, the results for $\langle A\rangle_{\text{Contact}}$ and $\langle A\rangle_{\text{Adhesion}}$ were comparable for iHbAS and iHbAA on ICAM-1 functionalized bilayers (χ^2-test, $p = 0.01$).

3.4.3.1 Statistics

Data was obtained from at least three independent experiments using blood from at least 3 different donors both for HbAA and HbAS. If not stated otherwise the presented values correspond to mean value and standard deviation.

3.4.4 Discussion

Reflection interference contrast microscopy has been successfully used to investigate how living cells adhere to a variety of substrates, mainly probing the influence of different adhesion motives, the density of stickers and the mechanical properties of the substrate itself[83, 162, 163].

The focus of this study was on the influence of an external shear stress on the adhesion of infected erythrocytes to solid-supported bilayers functionalized with CD36 or ICAM-1.

At the trophozoite stage of infection, the infected erythrocytes are still donut shaped[34]. Therefore, the maximum projection area above the substrate could reach up ~50 μm², depending on the cell orientation and assuming an average radius of ~4 μm. Yet, adherent infected erythrocytes were only in contact with the substrate with a contact area 1/5 of this size. Moreover, the subarea displaying firm adhesion was found to be only ~4 μm², or 8% of the maximum projection area. This finding indicates that a very small adhesion area can mediate firm adhesion under low shear stress conditions of 0.05 Pa and that a further growth of the adhesion area might be energetically unfavorable.

Both the movement of *P. falciparum* infected erythrocytes along planar substrates with uniform ligand densities and the subsequent adhesion process have been studied in great detail[145, 164, 165]. The influence of shear stress on firmly adherent cells has not yet been studied for *P. falciparum* infected erythrocytes. To further elucidate the findings of this study, the results were therefore interpreted within the scope of existing simulations studies based on the adhesion of leukocytes (white blood cell)[166, 167]. However, the comparison seems justified, since the adhesion behavior between leukocytes and iRBCs depicts several similarities[168] e.g. both tend to marginate towards the endothelium due to the higher cell stiffness compared to uninfected erythrocytes[169, 170, 171], both elevate their adhesins by membrane protrusions, microvilli [47, 172]and knobs[173], respectively, and both share the binding capability to ICAM-1[63, 174].

Simulations for adherent leukocytes show a negative effect on the adhesion area with increasing cytoplasmic viscosity and membrane stiffness[166, 167]. The small adhesion area therefore seems reasonable, since both properties were found to be significantly increased during the intraerythrocytic development of *P. falciparum* (Chapter 4.1.4). In their studies, the application of a shear field induced a cell deformation in flow direction, resulting in an increase of contact area[166, 167].

Indeed, the contact area of infected erythrocytes was found to significantly elevated with increasing shear stress, thereby promoting the formation of areas of firm adhesion. The dynamic growth of the contact or adhesion areas was not observed, since the image sequences were taken after 10 min of the respective shear stress conditions. The displayed contact or adhesion area sizes and shapes therefore rather represent the equilibrium state. Yet, one can speculate that an increase in shear stress firstly leads to the closing of the partial circle ring shaped contact areas, characteristic for infected erythrocytes for $\tau < 0.5$ Pa. Thereby, the formation of new ligand receptor pairs might be promoted by shear induced membrane fluctuations at the rim of the adhesion area, resulting in an increase of membrane substrate contact causing the growth of the adhesion area.

Higher shear stress conditions $\tau \geq 0.5$ Pa led to the formation of drop like contact areas, depicting large patches of adhesion area, as predicted from simulations based on deformable capsules[175]. The large adhesion patches, indicate a large number of ligand receptor pairs. The dissociation rate of an individual bond scales exponentially with the applied force (Equation 3-13), which can lead to very short bond life times and promote cell detachment. However, the total lifetime of the adhesion area, acting as a cluster of ligand-receptor pairs, might be several orders of magnitude higher[176, 177]. Importantly, the ligand distance was set to $\langle \mathrm{d} \rangle = 11$ nm, which might enhance the probability for a fast formation of new ligand-receptor pairs, which is mandatory for the stability of the receptor-ligand-bond cluster[176, 177].

The shear induced growth in contact area was comparable between CD36 and ICAM-1, indicating that it is governed mainly by the mechanical properties of the infected erythrocytes. In contrast, the growth in binding area was more pronounced for ICAM-1. Additionally, the average intensity fluctuations inside the adhesion area were also reduced compared to CD36. Both findings suggest a higher adhesion strength of infected erythrocytes adhering to ICAM-1 under high shear stress conditions $\tau \geq 0.5$ Pa, compared to CD36. This finding is supported by the higher critical shear stress observed for ICAM-1 over CD36 (Chapter 3.3.3) at an intermolecular ligand distance of $\langle d \rangle = 11$ nm.

The experiments performed on infected haemoglobinopathic erythrocytes revealed similar characteristics. In fact, the contact area, the adhesion area and the associated average MSA were comparable as a function of shear stress for ICAM-1 functionalized bilayers. This finding seems to promote the idea of a subpopulation of iHbAS previously termed “heavy binders” (Chapter 3.3.4), that could match the subpopulation of iHbAS, exhibiting a similar knob morphology and similar PfEMP1 expression levels as infected wildtype erythroctes[149].

Interestingly, the RICM results for iHbAS on CD36 functionalized bilayers did not support this interpretation. Although the general tendency of shear induced growth of contact area and adhesion area was prominent, both areas were found to be significantly reduced by roughly 30% compared to iHbAA. Yet, this result seems to be reasonable, based on the higher membrane bending modulus derived for iHbAS (Chapter 4.1.3) and the lower critical shear stress of detachment measured for iHbAS (Chapter 3.3.3) compared to iHbAA.

Under the assumption that ICAM-1 acts as the stronger adhesion partner under high shear stress conditions ($\tau \geq 0.5$ Pa), a functionalized bilayer with small ligand distance of only $\langle d \rangle = 11$ nm might not be suitable to detect the influences of different knob morphologies or differences in cell mechanics (Chapter 4.1.3). Moreover, the system was probed below the critical shear stress of detachment $\tau_{\mathrm{crit}} > 1$ Pa observed for both iHbAA and iHbAS.

3.4.5 Summary

Reflection interference contrast microscopy revealed a shear induced growth of contact and adhesion area of infected erythrocytes on CD36 and ICAM-1 functionalized bilayers. As predicted by simulations on leukocytes, the shear induced cell deformation seems to be responsible for the growth in adhesion area, which in turn would explain how infected erythrocytes can sustain high shear stress conditions. Moreover, the results indicate that ICAM-1 acts as the stronger binding partner at high shear stress conditions. For CD36 functionalized bilayers the differences between iHbAA and iHbAS such as knob morphology or cell mechanics, lead to a decrease in both contact and adhesion area, thereby supporting previous presented findings (Chapter 3.3.3). The same experiments performed with CD36 exchanged for ICAM-1, were non-conclusive, possible due to the fact that the experiments were performed below the critical shear stress of detachment (Chapter 3.3.3).

4 Mechanics and structure of infected red blood cells

The following two subchapters focus on the *P. falciparum* induced changes to the mechanics (Chapter 4.1) and the elemental composition (Chapter 4.2) of individual infected erythrocytes derived by non-invasive, label free techniques. The presented studies include wildtype HbAA and haemoglobinopathic erythrocytes HbAS and HBAC. Each subchapter contains a detailed background description of the applied method, an overview of the experimental conditions and the results obtained by the respective studies.

4.1 *P. falciparum* induced changes to the red blood cell mechanics

4.1.1 Background of flicker spectroscopy

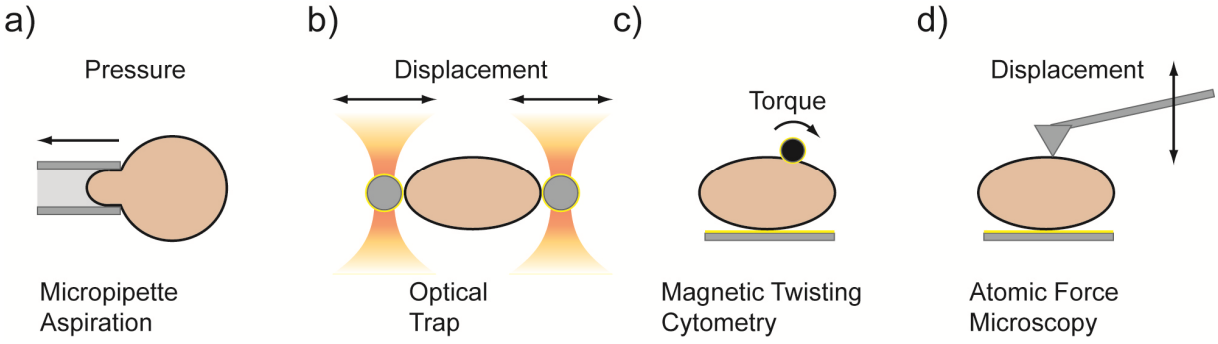

Figure 4.1 | Comparison of techniques used to probe the mechanical characteristics of cells. (a) Micropipette aspiration and (b) optical traps apply forces onto the entire cell body. (c) Magnetic twisting cytometry and (d) atomic force microscopy do probe cells with a high special resolution.

In the field of biological physics, a variety of methods has been applied to determine a coherent description of the mechanical parameters of a cell. Thereby, the majority of methods relies on active mechanical stimulation. Methods like micropipette aspiration and optical traps (Figure 4.1 a and b) allow to characterize large scale deformations yielding the membrane tension and the shear modulus, respectively[114, 178]. Whereas local stimuli applied by magnetic twisting cytometry or by atomic force microscopy (Figure 4.1 c and d) can be used to determine the elastic modulus[179, 180].

Another very elegant approach is the direct characterization of naturally occurring membrane fluctuations. The "membrane flickering phenomena" has been reported for erythrocytes already at the end of the 19th century[181]. The corresponding label and contact free technique termed "flicker spectroscopy" is based on the analysis of the continuous small fluctuations of "quasi-flat" or "planar" membranes under thermal equilibrium conditions.

Based on the early work of Helfrich and Servuss[182] the corresponding Hamiltonian can be formulated as:

$$H[u(x,y)] = \int_A dxdy \left[\frac{\sigma}{2}\left(\nabla u(x,y)\right)^2 + \frac{\kappa}{2}\left(\Delta u(x,y)\right)^2 + \frac{\gamma}{2}u(x,y)^2\right]. \qquad 4\text{-}1$$

The observable undulations for each point in real space $u(x,y)$ of the total membrane area A depend on the membrane tension σ and the membrane bending modulus κ. In the case of the

red blood cell, the anchoring of the membrane to the underlying cytoskeleton network was included in the form of an additional harmonic confinement parameter γ[183, 184].

The undulations of a membrane square patch with $A = L \times L$ can be represented in Fourier space according to:

$$u(\boldsymbol{r}) = \sum_{\boldsymbol{q}} u_{\boldsymbol{q}} e^{i\boldsymbol{q}\cdot\boldsymbol{r}}, \qquad \boldsymbol{q} = \frac{2\pi}{L}\begin{pmatrix} n_x \\ n_y \end{pmatrix}, \qquad n_x, n_y \in \mathbb{Z}. \tag{4-2}$$

The derivatives can be calculated as followed using $u_{-\boldsymbol{q}} = u_{\boldsymbol{q}}^*$:

$$(\nabla u)^2 = \sum_{\boldsymbol{q},\boldsymbol{q}'} u_{\boldsymbol{q}} u_{\boldsymbol{q}'} (-\boldsymbol{q}\cdot\boldsymbol{q}')\, e^{i(q+q')r}, \tag{4-3}$$

$$(\nabla^2 u)^2 = \sum_{\boldsymbol{q},\boldsymbol{q}'} u_{\boldsymbol{q}} u_{\boldsymbol{q}'} (q^2 \cdot q'^{\boldsymbol{2}})\, e^{i(q+q')r}. \tag{4-4}$$

Taking the Fourier representation of the Kronecker-δ into account:

$$\int_{L\times L} dxdy\, e^{-i\boldsymbol{q}\cdot\boldsymbol{r}} = L^2 e^{iqL/2} \frac{sin\left(\frac{qL}{2}\right)}{\frac{qL}{2}} = L^2 \delta_{\boldsymbol{q},\boldsymbol{0}}, \tag{4-5}$$

one can directly derive from equation (4-1):

$$H[u(x,y)] = \int_{L\times L} dxdy \sum_{\boldsymbol{q},\boldsymbol{q}'} u_{\boldsymbol{q}} u_{\boldsymbol{q}'} e^{i(\boldsymbol{q}+\boldsymbol{q}')\boldsymbol{r}} \left[\frac{\sigma}{2}(-\boldsymbol{q}\cdot\boldsymbol{q}') + \frac{\kappa}{2}(q^2 \cdot q'^{\boldsymbol{2}}) + \frac{\gamma}{2}\right] \tag{4-6}$$

$$= \sum_{\boldsymbol{q},\boldsymbol{q}'} u_{\boldsymbol{q}} u_{\boldsymbol{q}'} L^2 \delta_{\boldsymbol{q}+\boldsymbol{q}',\boldsymbol{0}} \left[\frac{\sigma}{2}(-\boldsymbol{q}\cdot\boldsymbol{q}') + \frac{\kappa}{2}(q^2 \cdot q'^{\boldsymbol{2}}) + \frac{\gamma}{2}\right] \tag{4-7}$$

$$= L^2 \sum_{\boldsymbol{q}} \left|u_{\boldsymbol{q}}\right|^2 \left[\frac{\sigma}{2}q^2 + \frac{\kappa}{2}q^4 + \frac{\gamma}{2}\right] \tag{4-8}$$

Now one can apply the equipartition theorem stating that each degree of freedom carries the same amount of energy on average under thermal equilibrium conditions:

$$\frac{1}{2}k_B T = \left[\frac{\sigma}{2}q^2 + \frac{\kappa}{2}q^4 + \frac{\gamma}{2}\right] L^2 \langle \left|u_{\boldsymbol{q}}\right|^2 \rangle. \tag{4-9}$$

This leads us to the well-known result:

$$\langle u(q)^2 \rangle = \frac{k_\mathrm{B} T}{L^2} \frac{1}{\gamma + \sigma q^2 + \kappa q^4}. \tag{4-10}$$

From equation (4-10) one can already roughly estimate the expected total fluctuation amplitude for the simple case of a bending dominated membrane system where σ and γ are negligible:

$$\sum_{\boldsymbol{q}} \langle \left|u_{\boldsymbol{q}}\right|^2 \rangle = \sum_{\boldsymbol{q}} \frac{k_\mathrm{B} T}{L^2} \frac{1}{\kappa q^4} \approx \left(\frac{L}{2\pi}\right)^2 \int_{q_{min}}^{q_{max}} dq 2\pi q \frac{k_\mathrm{B} T}{L^2} \frac{1}{\kappa q^4} \tag{4-11}$$

With $q_{min} = 2\pi/L$ dependent on the macroscopic system size cutoff L, and $q_{max} = 2\pi/a$ the cutoff as defined by the estimation of membrane thickness a.

$$\sum_{\boldsymbol{q}} \langle |u_{\boldsymbol{q}}|^2 \rangle \approx \frac{1}{4\pi} \frac{k_B T}{\kappa} \left[\left(\frac{L}{2\pi} \right)^2 - \left(\frac{a}{2\pi} \right)^2 \right] \overset{a \ll L}{\longrightarrow} \frac{k_B T}{16\pi^3 \kappa} L^2 \qquad 4\text{-}12$$

From equation (4-12) one can see, that fluctuations are proportional to the system temperature T and inverse proportional to the bending modulus κ. Taking the typical regime for the bending modulus of a pure lipid bilayer with $\kappa \sim 10 - 20\ k_B T$[185], one would expect fluctuations in the range of 100 nm for typical cell sizes ($L \sim 10$ µm). For systems with non-negligible membrane tension and harmonic confinement the observable fluctuation amplitudes can be expected to be distinctly lower.

By applying the "spherical harmonics" approach following the work of Milner and Safran[186, 187], one can extract additional information out of the temporal domain of the fluctuation spectrum. In a first step, the cell can be described by the angle dependent radius r:

$$r(\Omega) = \langle r \rangle \left(1 + \sum_{l,m} u_{lm} Y_{lm}(\Omega) \right). \qquad 4\text{-}13$$

Ω denotes to the solid angle, $\langle r \rangle$ to the mean radius of the sphere and $Y_{l,m}$ to the spherical harmonic for each mode l, m with their corresponding fluctuation amplitude u_{lm}. The mean square amplitude for each mode $\langle |{u_{lm}}^2| \rangle$ can be derived from the Hamiltonian presented in equation (4-1):

$$\langle |u_{lm}|^2 \rangle = \frac{k_B T}{\kappa (l+2)(l-1) l(l+1) + \sigma \langle r \rangle^2 (l+2)(l-1) + \gamma \langle r \rangle^4}. \qquad 4\text{-}14$$

For each mode one can solve the Navier-Stokes equation in spherical harmonics resulting in the Lamb solution[188], where each mode shows a characteristic relaxation frequency ω_l:

$$\omega_l = \frac{\kappa (l+2)(l-1) l(l+1) + \sigma \langle r \rangle^2 (l+2)(l-1) + \gamma \langle r \rangle^4}{(\eta)/2 \langle r \rangle^3 Z(l)}. \qquad 4\text{-}15$$

The mean buffer viscosity of outer and inner medium is denoted as η. $Z(l)$ is defined as:

$$Z_l = \frac{(2l+1)(2l^2 + 2l - 1)}{l(l+1)}. \qquad 4\text{-}16$$

The amplitude of each excited mode should decay with a single exponential dissipating the energy into the medium as described by the autocorrelation function:

$$\langle u_{lm}(t) u_{l'm'}(0) \rangle = \delta_{l,l'} \delta_{m,m'} \langle |u_{lm}|^2 \rangle e^{-\omega_l t}. \qquad 4\text{-}17$$

Based on the Wiener-Khinchin theorem[189] the power spectral density (*PSD*) relates to the autocorrelation by Fourier-transformation integrating over all modes u_{lm}:

$$PSD(\omega) = \langle r \rangle^2 \int dt \sum_{l=2,m=-l}^{l_{max},m=+l} \langle |{u_{lm}}^2| \rangle \exp(-\omega_l t) \exp(-i\omega t) \quad 4\text{-}18$$

$$= \langle r \rangle^2 \sum_{l=2}^{l_{max}} \langle |{u_{lm}}^2| \rangle \frac{\omega_l}{\omega_l^2 + \omega^2} \frac{2l+1}{2\pi}. \quad 4\text{-}19$$

Please note that the $l = 0$ mode describes changes to the volume and is excluded under the assumption of incompressible fluids and no fluid exchange throughout the membrane. The $l = 1$ mode simply represents a displacement of the sphere in total and can therefore be neglected as well.

4.1.2 Experimental realization

4.1.2.1 Flicker spectroscopy

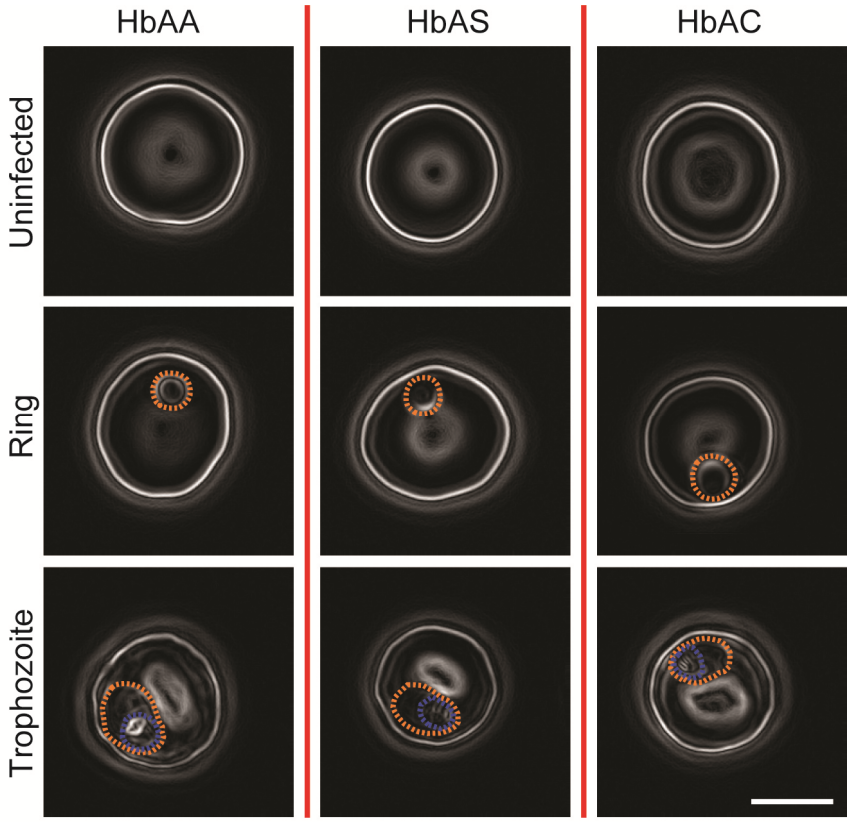

Figure 4.2 | Optical validation of the different stages of infection based on gradient maps derived from phase contrast images. The ring stage (10 to 18 h post invasion) is characterized by the typical ring shaped parasite, while additional compartments like the digestive vacuole are only visible at the later trophozoite stage (24 to 32 h post invasion). The cytoplasmic space occupied by the parasite is highlighted in orange and the digestive vacuole in blue. Scale bar, 5 µm.

Uninfected erythrocytes and infected erythrocytes at the ring and trophozoite stage of infection were resuspended in RPMI-BSA buffer at 37°C (Chapter 3.1.3.1) at a hematocrit of ~0.1%. RPMI-BSA contains 2 mg ml^{-1} D-glucose necessary to assure a constant ATP level for the preservation of the cytoskeletal activity[190]. In a first step, cell suspensions were incubated in petri dishes with glass bottom for 30 minutes placed inside a temperature controlled

chamber mounted to an inverted microscope (Axio Observer Z1, Zeiss, Oberkochen, Germany). Afterwards, a sequence of 500 phase contrast images with an exposure time of 25 ms was recorded for each cell using a 100 × oil-immersion objective lens (NA = 1.4) and an ORCA-Flash4.0 LT (Hamamatsu Photonics, Hamamatsu, Japan) camera. Although cells were kept in synchronized culture, the stage of infection was additionally confirmed from the gradient maps derived from phase contrast images for individual cells (Figure 4.2). Please note, that later parasite stages (schizont stage) of infection did not exhibit visible membrane fluctuations. Furthermore, the overall buckling of the infected erythrocytes membrane did not allow for a determination of the entire cell contour. All analyses were performed using self-written routines in Matlab (R2016b).

4.1.2.2 Analysis of the fluctuation spectra

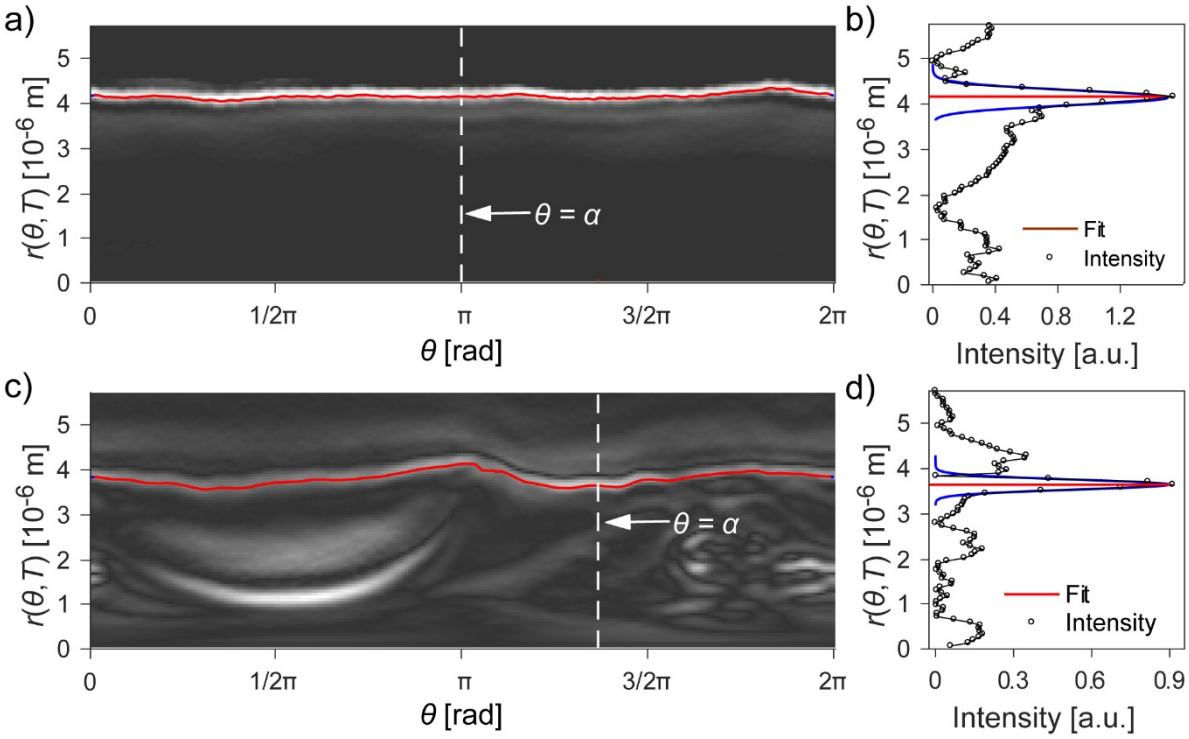

Figure 4.3 | Determination of cell contours from gradient images. (a) Gradient map $r(\theta,T)$ in a polar coordinate for a given time point T for an uninfected wildtype erythrocyte. The calculated rim position $r_{rim}(\theta,T)$ is highlighted in red for $0 < \theta < 2\pi$. (b) As an example the determination of the rim position at a fixed angular position $\theta = \alpha$ (dashed white line in (a)) is presented. The intensity maximum was derived from a Gaussian fit (blue). (c) and (d) The analogue procedure as carried out for a wildtype erythrocyte at the trophozoite stage of infection.

The cell contour as described by $r_{rim}(\theta, t)$ was derived from gradient maps transformed into a polar coordinate of $0 < \theta < 2\pi$ using a step size of $\Delta\theta = 2\pi/256$, with the center of mass of each frame at $r_{rim}(\theta, t) = 0$ (Figure 4.3).

The time dependent deviations of $r_{rim}(\theta, t)$ from the average rim position were Fourier-transformed resulting in the mean square displacement (MSD) as a function of the discrete wave number q_x obtained from experiments:

$$\langle u(q_x)^2\rangle_{Exp} = \left\langle \left| \frac{2}{N} \sum_{n=0}^{N-1} \{r_{\mathrm{rim}}(n\Delta\Theta) - \langle r_{\mathrm{rim}}(n\Delta\Theta)\rangle\} e^{\frac{2\pi i \langle r\rangle q_x n}{N}} \right|^2 \right\rangle. \qquad 4\text{-}20$$

The time average value obtained over the entire image series is denoted by ⟨ ⟩. Microscopic observations of membrane fluctuations are naturally limited to the equatorial plane. To correctly match the theoretically predicted *MSD* spectrum, equation (4-14) had to be inverse Fourier-transformed in regard to the continuous wave number q_y:

$$\langle u(q_x, y=0)^2\rangle_{\mathrm{Theo}} = \frac{k_B T}{L} \sqrt{\frac{\kappa}{2(\sigma^2 - 4\kappa\gamma)}} \left[\left| \frac{1}{\sqrt{2\kappa q_x^2 + \sigma - \sqrt{\sigma^2 - 4\kappa\gamma}}} - \frac{1}{\sqrt{2\kappa q_x^2 + \sigma + \sqrt{\sigma^2 - 4\kappa\gamma}}} \right| \right]. \qquad 4\text{-}21$$

Here the cell contour length $L = 2\pi\langle r\rangle$ was estimated from the mean cell radius $\langle r\rangle$. In the low q_x regime the difference between the *MSD* of a planar and a spherical membrane is ≥ 15%[191, 192], therefore the fitting of the experimentally obtained *MSD* to equation (4-21) was performed only above mode $n \geq 4$ corresponding to $q_x \geq \frac{2\pi n}{L} \sim 1 \times 10^6\ \mathrm{m}^{-1}$.

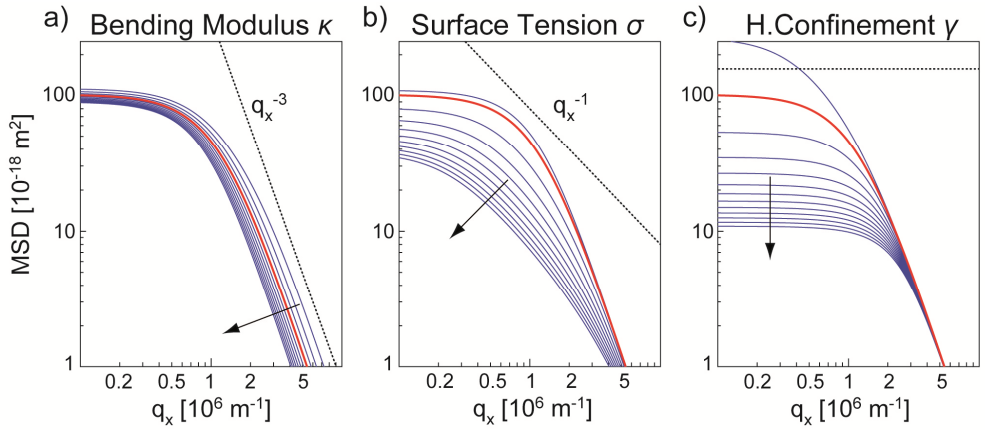

Figure 4.4 | Mechanical properties influence the mean square displacement at different q_x regimes. Changes to the mean square displacement as a function of (a) the bending modulus κ,(b) the membrane tension σ and (c) the harmonic confinement γ according to equation (4-21). Red lines correspond to the *MSD* calculated for an uninfected wildtype erythrocyte with $\kappa = 2.7 \times 10^{-19}$N m, $\sigma = 0.7 \times 10^{-6}$ N m^{-1} and $\gamma = 0.5 \times 10^6$ N m^{-3}. The arrows indicate the typical dampening of the MSD dependent on the mechanical parameter increasing. Dotted lines correspond to the power law scaling the MSD obeys at different q_x regimes.

Please note, that the observed *MSD* should exhibit different power law dependencies according to equation (4-21). In the tension dominated region ($\sigma \gg \kappa q_x^2$) the *MSD* should follow $\langle u(q_x, y=0)^2\rangle \sim q_x^{-1}$ while in the bending dominated region ($\sigma \ll \kappa q_x^2$) it should obey $\langle u(q_x, y=0)^2\rangle \sim q_x^{-3}$[191]. Additionally, one would expect the MSD to level of for $q_x \to 0$ (Figure 4.4).

Due to limited temporal resolution and total recording time (25 ms, 12500 ms, respectively) of the microscopic observations, only a small region of the frequency domain is accessible after Fourier-transformation. To determine the red blood cell viscosity η_{RBC} using equation (4-19) with $\eta = 1/2(\eta_{\mathrm{RBC}} + \eta_{\mathrm{buffer}})$, the bending modulus κ, the membrane tension σ and the harmonic confinement γ were fixed using their previously determined values obtained by equation (4-21). Analogue to the *MSD*, the *PSD* should exhibit different power law regimes. According to equation (4-19) one can expect a tension σ dominated domain at low frequencies and a bending modulus κ dominated regime for high frequency, as described by a power law of f^{-1} and $f^{-5/3}$, respectiely[186].

4.1.3 Results

4.1.3.1 Elevation of mechanical parameters in wildtype erythrocytes by *P. falciparum*

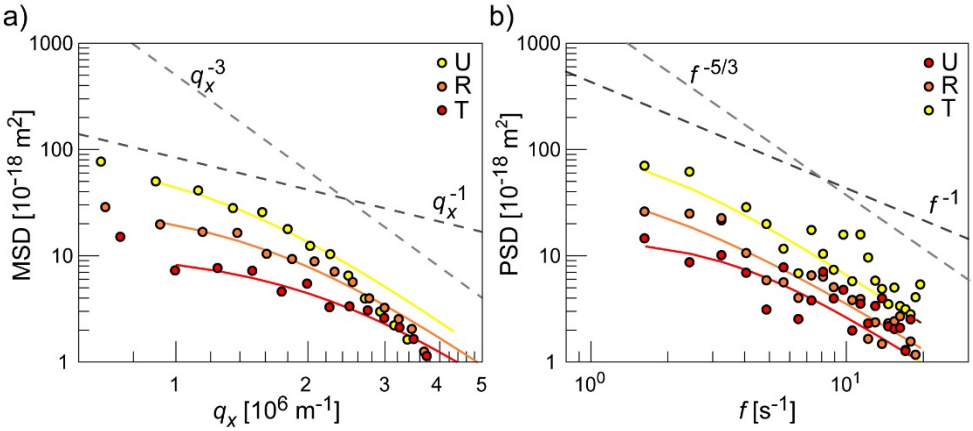

Figure 4.5 | Membrane fluctuation spectra derived for uninfected wildtype erythrocytes and corresponding *P. falciparum* infected cells at the ring and trophozoite stage of infection. (a) Mean square displacement (*MSD*) as a function of the wavenumber q_x and (b) power spectrum density (*PSD*) as a function of the frequency f. Data points and fits obtained by equations 4-21 and 4-19 correspond to individual representative wildtype cells (uninfected (U, yellow), ring (R, orange) and trophozoite (T, red)). The power law dependencies for tension and bending dominated regimes are presented to guide the eye (dotted lines).

In a first step, flicker spectroscopy was applied to uninfected wildtype erythrocytes (HbAA) to establish a point of reference. The obtained mean square displacement spectra (Figure 4.5 a) do exhibit the power law dependencies as predicted from the theoretical argumentation. Although no convergence level at low values of q_x is prominent. In general, the fluctuation amplitude of individual modes was found to be below 10 nm. Fitting equation (4-21) to the *MSD* spectra yielded a average bending modulus of $\langle\kappa\rangle = 2.7 \pm 0.6 \times 10^{-19}$N m, a mean membrane tension of $\langle\sigma\rangle = 0.7 \pm 0.2 \times 10^{-6}$ N m^{-1}and a mean harmonic confinement of $\langle\gamma\rangle = 0.5 \pm 0.2 \times 10^{6}$ N m^{-3} based on a total of $n = 42$ cells. These values are consistent with previous determinations based on flicker spectroscopy[191, 192]. Note that the confinement parameter γ relates to the shear modulus μ by $\mu = \gamma r^2$. With a mean red blood cell radius of $\langle r\rangle \sim 4$ µm and the flicker spectroscopy derived harmonic confinement one can calculate $\langle\mu\rangle \sim 8 \times 10^{-6}$ N m^{-1} , which is comparable to values obtained by classical methods like micropipette aspiration[1, 165]. It is noteworthy that the high bending modulus of $\langle\kappa\rangle \sim 2.7 \times$

10^{-19}N m is three to five times higher than typical values for a simple bilayer system, accounting for the complex composition of the erythrocytes membrane [185].

The analysis of the temporal domain yielded the power spectrum density (Figure 4.5) as a function of the frequency $f = 2\pi\omega$. The spectra also obeyed the theoretically expected power law dependencies following equation (4-18). The mean red blood cell viscosity was found to be $\langle\eta_{\mathrm{RBC}}\rangle = 1.2 \pm 0.7 \times 10^{-2}\mathrm{N\,m^{-2}s}$. This value is in good agreement with other flicker spectroscopy based determinations[191].

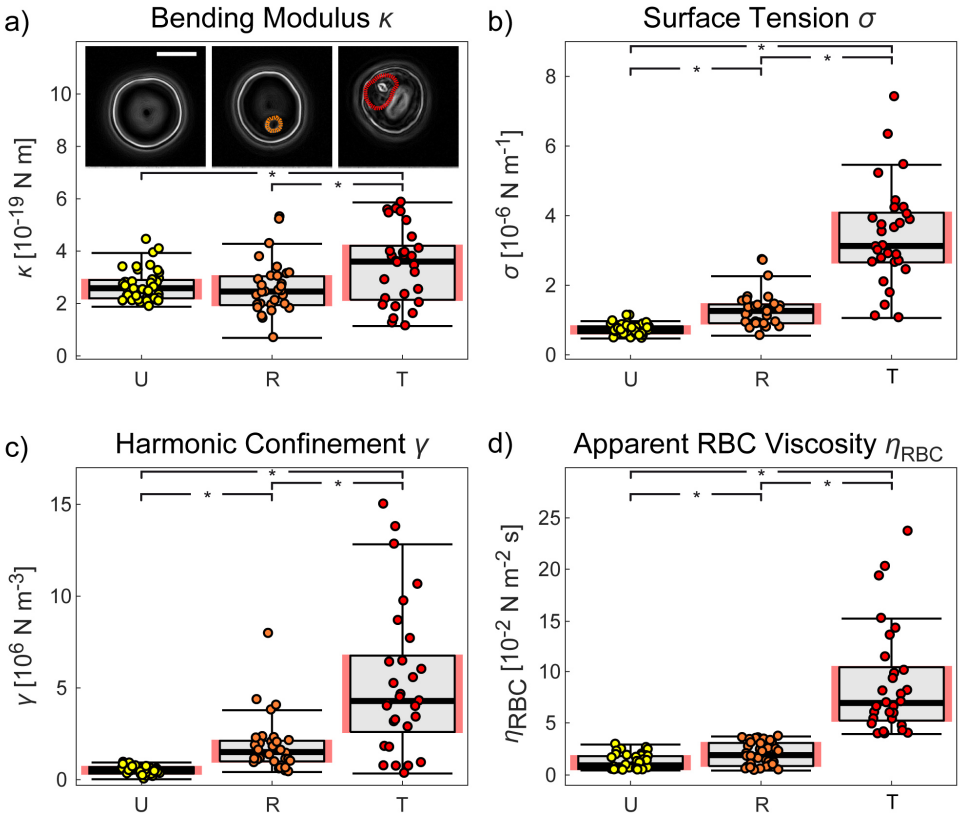

Figure 4.6 | *P. falciparum* induces changes to the erythrocyte mechanics. Infection with *P. falciparum* results in a significant alteration of all biomechanical parameters accessible by flicker spectroscopy. A representative gradient image for each observed stage is presented as an inset in panel (a) with the parasite occupied cytoplasmic space highlighted by a dotted line. Each data point for (a) the bending modulus κ, (b) the membrane tension σ, (c) the harmonic confinement γ and (d) the apparent red blood cell viscosity η_{RBC} represents a determination for individual cells from four different donors (uninfected (U, yellow), ring (R, orange) and trophozoite (T, red)). The $25-75$ percentile range obtained for each boxplot (grey) is highlighted in red and replotted in figure (Figure 4.7) and (Figure 4.8) to allow for a visual comparison. *, $p < 0.01$ according to Welch t-test. Scale bar, 5 µm.

Next, wildtype erythrocytes infected with *P. falciparum* at the ring stage (10 to 18 h post invasion) and the trophozoite stage (24 to 32 h post invasion) of infection were investigated. The dramatic changes by *P. falciparum* are directly visible by eye (Figure 4.2) as a change from a smooth erythrocyte surface at the uninfected stage to an increasingly rougher surface appearance at infectious stages. This trend was reflected in the Gaussian surface roughness (RMS) increasing from 90 ± 34 nm for uninfected erythrocytes to 137 ± 44 nm for the ring

stage up to 169 ± 47 nm at the trophozoite stage. The intracellular parasite maturation was correlated with a progressive dampening of membrane fluctuations (Figure 4.5) from the ring stage (R) to the trophozoite stage (T).

In fact, all mechanical parameters significantly increased gradually during the observed time window (Figure 4.6, Table 4-1). Although the time interval from uninfected to ring stage is similar to the time interval from ring stage to trophozoite stage, the changes in mechanics are predominantly observed in the second time window. The bending modulus was found reach to $\langle\kappa\rangle = 3.4 \pm 1.4 \times 10^{-19}$N m at the trophozoite stage, equal to a mild increase of ~25% from the uninfected stage. In contrast, the membrane tension reached $\langle\sigma\rangle = 2.7 \pm 1.2 \times 10^{-6}$ N m^{-1}and the harmonic confinement $\langle\gamma\rangle = 5.3 \pm 4.0 \times 10^{6}$ N m^{-3} during the same time window, corresponding to a 4-fold and 10-fold increase from the uninfected values, respectively. Additionally, the apparent red blood cell viscosity was found to increase 7-fold to $\langle\eta_{\mathrm{RBC}}\rangle = 8.8 \pm 5.2 \times 10^{-2}$N m^{-2}s. The overall stiffening of erythrocytes caused by *P. falciparum* has been observed before, applying other techniques[193, 194], yet the analysis using flicker spectroscopy identified that this effect is based predominantly on the increase of the membrane-cytoskeleton coupling.

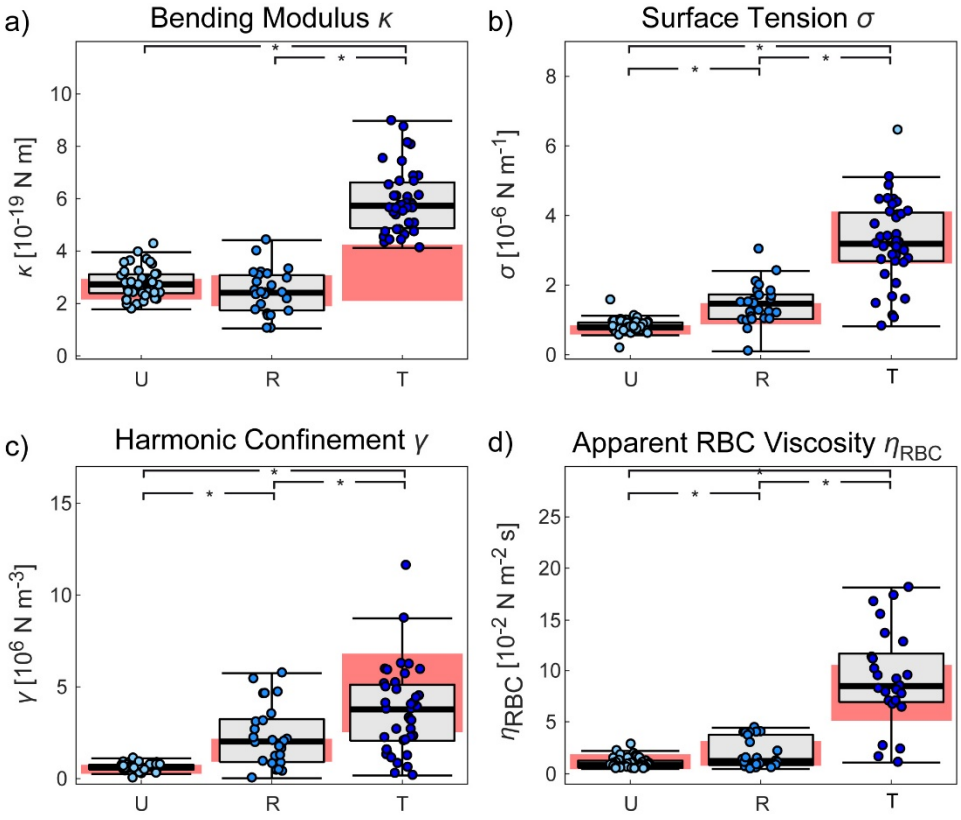

Figure *4.7* | *P.falciparum* induces changes to the mechanics of haemoglobinopathic blood of type HbAS. Each data point represents a single cell determination of the (a) the bending modulus κ, (b) the membrane tension σ, (c) the harmonic confinement γ and (d) the apparent red blood cell viscosity η_{RBC} for erythrocytes of three different donors (uninfected (U, light blue), ring (R, blue) and trophozoite (T, dark blue)). The $25-75$ to percentile range for the wildtype HbAA as presented in figure (Figure 4.6) is highlighted in red for each parameter to allow for a direct visual comparison. *, $p < 0.01$ according to Welch t-test.

4.1.3.2 Strain hardening effect in uninfected haemoglobinopathic erythrocytes & *P. falciparum* infected HbAS and HbAC excel in membrane bending modulus

Flicker spectroscopy was then applied to uninfected haemoglobinopathic erythrocytes and *P. falciparum* infected erythrocytes at the same stages of infection based on synchronized cultures. Interestingly, uninfected haemoglobinopathic erythrocytes displayed significantly higher values of membrane tension σ and harmonic confinement γ compared to uninfected wildtype erythrocytes (Figure 4.7, Figure 4.8 and Table 4-1).

The bending modulus κ and the apparent viscosity η_{RBC} were comparable. With the latter finding concurring with recent reports on similar mean corpuscular haemoglobin concentrations for HbAA, HbAS and HbAC[34].

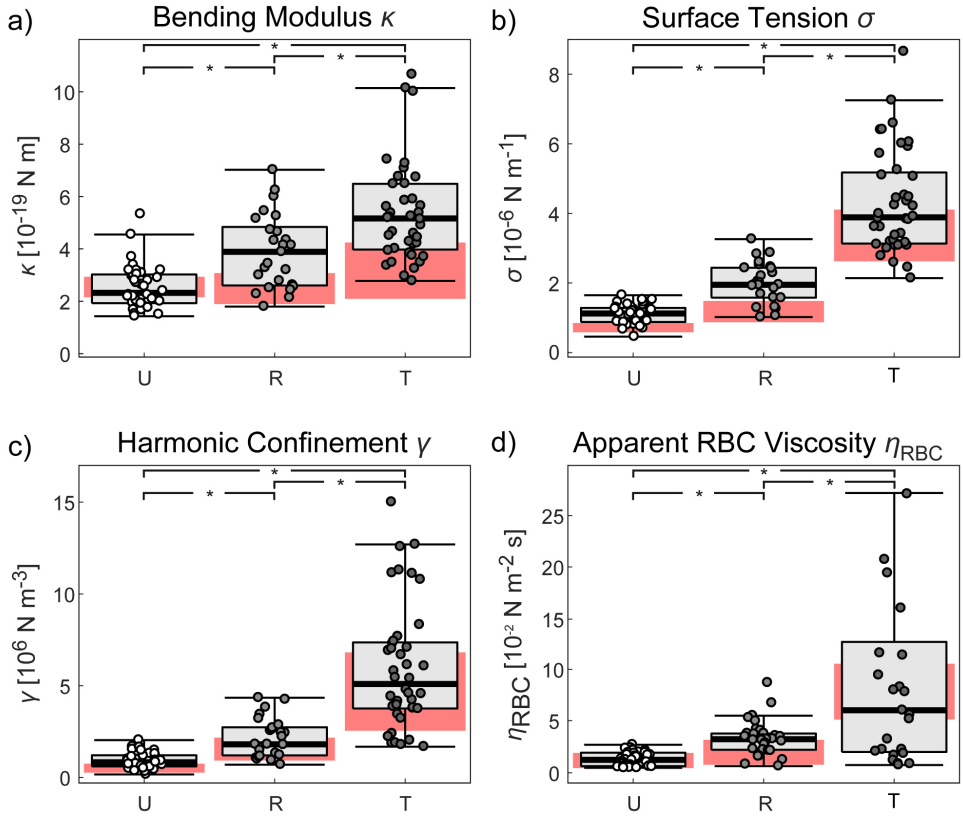

Figure 4.8 | *P.falciparum* induces changes to the mechanics of haemoglobinopathic blood of type HbAC. Each data point represents a single cell determination of the (a) the bending modulus κ, (b) the membrane tension σ, (c) the harmonic confinement γ and (d) the apparent red blood cell viscosity η_{RBC} for erythrocytes of three different donors (uninfected (U, white), ring (R, light grey) and trophozoite (T, dark grey)). The $25-75$ to percentile range for the wildtype HbAA as presented in figure (Figure 4.6) is highlighted in red for each parameter to allow for a direct visual comparison. *, $p < 0.01$ according to Welch t-test.

The intraerythrocytic maturation of *P. falciparum* in haemoglobinopathic blood caused a gradual increase of all mechanical parameters (Figure 4.7 and Figure 4.8), comparable to the trend observed for infected wildtype erythrocytes. Yet flicker spectroscopy revealed differences between the haemoglobinopathies and the wildtype and among the haemoglobinopathies themselves. The bending modulus κ was found to be significantly higher for HbAS with $\langle\kappa\rangle = 5.9 \pm 1.2 \times 10^{-19}$N m and HbAC with $\langle\kappa\rangle = 5.5 \pm 2.2 \times 10^{-19}$N m,

corresponding to an increase of 70% and 60%, respectively compared to the wildtype at the same infection stage ($p < 0.01$). The harmonic confinement of HbAC at the trophozoite stage of $\langle\gamma\rangle = 6.0 \pm 3.4 \times 10^6$ N m^{-3} was comparable to HbAA, while it was significantly lower in the case of HbAS with $\langle\gamma\rangle = 3.7 \pm 2.4 \times 10^6$ N m^{-3}. In contrast, there were no differences found in the apparent viscosity $\langle\eta_{\mathrm{RBC}}\rangle$.

4.1.3.3 Reduction of membrane to cytoskeleton coupling in knobless parasites

To further investigate the mechanical impact of knobs, a knobless phenotype grown in wildtype HbAA erythrocytes was subjected to flicker spectroscopy. Thereby the knobless phenotype was derived from a FCR3 strain by a chromosomal breakage and healing event within the knob associated histidine rich protein (KAHRP) gene, resulting in a truncated non-functional KAHRP gene[195]. Scanning electron microscopy images confirmed the absence of knob structures at the trophozoite stage of infection (Figure 4.9 a). The corresponding surface roughness was found to be 114 ± 31 nm, comparable to the values derived for uninfected wildtype erythrocytes of HbAA. Flicker spectroscopy revealed a twofold lower harmonic confinement of $\langle\gamma\rangle = 2.3 \pm 1.2 \times 10^6$ N m^{-3} and a significantly lower membrane tension σ, compared to the knobby FCR3 strain (Figure 4.9). Yet, the bending modulus κ and the apparent viscosity η_{RBC} were found to be comparable

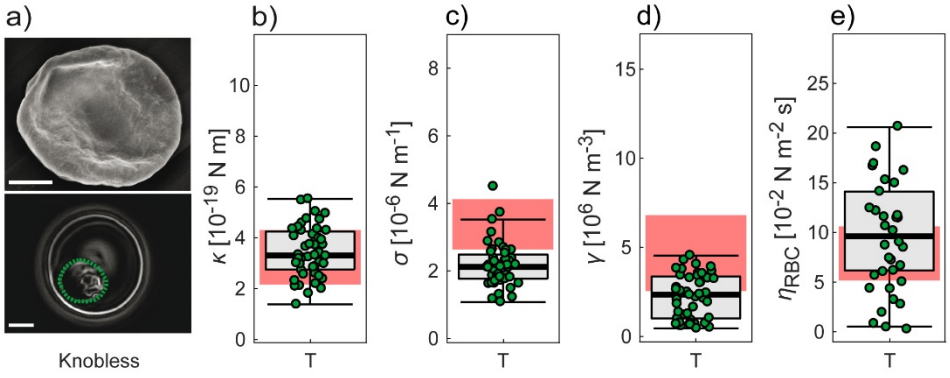

Figure 4.9 | Wildtype HbAA erythrocytes infected with a knobless FCR3-phenotype at the trophozoite stage. (a) Scanning electron micrograph (SEM, upper panel) and gradient image obtained from a phase contrast image (lower panel) of a representative infected erythrocyte. Each data point for (b) the bending modulus κ, (c) the membrane tension σ, (d) the harmonic confinement γ and (e) the apparent red blood cell viscosity η_{RBC} represent a single cell determination for erythrocytes of three different donors (trophozoite (T, green)). The $25-75$ to percentile range for the wildtype HbAA as presented in figure (Figure 4.6) is highlighted in red for each parameter to allow for a direct visual comparison. (SEM imaging was performed by Dr. Marek Cyrklaff, Center for Infectious Diseases, Heidelberg University Hospital). Scale bar, 5 µm.

4.1.3.4 Statistics

Data was obtained from at least three independent experiments using blood from at least 3 different donors both for HbAA/HbAS/HbAA. If not stated otherwise the presented values correspond to mean value and standard deviation.

4.1.4 Discussion

The intraerythrocytic maturation of *P. falciparum* leads to drastic changes in the structure of the host cell leading to alterations in the mechanical properties. Thereby, the understanding of the causative biological processes is important, since many disease-related processes, like splenic clearance, endothelial adhesion or obstruction of the micro vascularity are directly linked to the mechanical properties of the infected erythrocytes[36, 196]. Flicker spectroscopy not only allows for a contact free quantification of distinct mechanical parameters as a function of parasite stage and blood type, but further allows for a direct interpretation of the underlying biological causes.

The elevated bending modulus κ for both wildtype and haemoglobinopathic erythrocyte at the trophozoite stage of infection, reflecting a change in membrane composition, in fact, coincides with the reports of the in cooperation of parasite synthesized proteins into the membrane[197, 198]. At the same time, the increased amount of membrane cross-linked, irreversibly oxidized haemichromes, characteristic for infected HbAS and HbAC[73], could explain the additional increase in bending modulus κ observed solely for the haemoglobinopathies.

Table 4-1 | Summary of all biomechanical parameters obtained by flicker spectroscopy. Numbers correspond to the mean value and standard deviation obtained from (n) independent determination.

		Bending modulus κ [10^{-19} N m]	**Membrane tension σ [10^{-6} N m^{-1}]**	**Harmonic confinement γ [10^{6} N m^{-3}]**	**Apparent RBC viscosity η_{RBC} [10^{-2} N m^{-2} s]**
Uninfected	HbAA	2.7 ± 0.6 (42)	0.7 ± 0.2 (42)	0.5 ± 0.2 (42)	1.2 ± 0.7 (42)
	HbAS	2.8 ± 0.6 (41)	0.8 ± 0.2 (41)*	0.6 ± 0.2 (41)*	0.9 ± 0.5 (41)
	HbAC	2.5 ± 0.8 (36)	1.1 ± 0.3 (36)$^{*,\#}$	0.9 ± 0.4 (36)$^{*,\#}$	1.3 ± 0.6 (36)
Ring	HbAA	2.6 ± 1.0 (30)	1.3 ± 0.5 (30)$^{\$}$	1.9 ± 1.5 (30)$^{\$}$	1.9 ± 1.1 (30)$^{\$}$
	HbAS	2.5 ± 0.8 (25)	1.4 ± 0.6 (25)$^{\$}$	2.3 ± 1.7 (25)$^{\$}$	1.9 ± 1.4 (25)$^{\$}$
	HbAC	3.9 ± 1.4 (25)$^{\$,\S,\&}$	2.0 ± 0.6 (25)$^{\$,\S,\&}$	2.2 ± 1.1 (25)$^{\$,\S}$	3.3 ± 1.7 (25)$^{\$,\S,\&}$
Trophozoite	HbAA	3.4 ± 1.4 (29)$^{\$}$	2.7 ± 1.4 (29)$^{\$}$	5.3 ± 4.0 (29)$^{\$}$	8.8 ± 5.2 (29)$^{\$}$
	HbAS	5.9 ± 1.2 (39)$^{\$,\S}$	3.2 ± 1.2 (39)$^{\$}$	3.7 ± 2.4 (39)$^{\$,\S}$	9.2 ± 4.6 (39)$^{\$}$
	HbAC	5.5 ± 2.2 (40)$^{\$,\S}$	4.3 ± 1.4 (40)$^{\$,\S,\&}$	6.0 ± 3.4 (40)$^{\$,\&}$	10.4 ± 12.2 (40)$^{\$}$
knobless Trophozoite	HbAA	3.4 ± 1.0 (42)$^{\$}$	2.2 ± 0.7 (42)$^{\$,\S}$	2.3 ± 1.2 (42)$^{\$,\S}$	9.2 ± 5.3 (34)$^{\$}$

*, $p < 0.01$ compared with uninfected HbAA erythrocytes; $^{\#}$, $p < 0.01$ compared with uninfected HbAS erythrocytes; $^{\$}$, $p < 0.01$ compared with the corresponding uninfected erythrocyte variant. §, $p < 0.01$ compared with age-matched parasitized HbAA erythrocytes; $^{\&}$, $p < 0.01$ compared with age-matched parasitized HbAS erythrocytes; $^{\&}$, $p < 0.01$ compared with age-matched parasitized HbAS erythrocytes; Statistical significance was determined using Welch t-test.

The analysis of the temporal domain of the membrane fluctuations yielded the apparent viscosity η_{RBC}. Although the value was found to be comparable to previous determinations based on flicker spectroscopy[191], it was in fact two times larger than the viscosity values derived for a homogeneous haemoglobin solution (0.32 mg/mL)[199]. A peculiar phenomenon since 95% of the erythrocyte dry mass corresponds to just haemoglobin. Yet, one can argue that this discrepancy is based on the semi-crystalline character of haemoglobin reported in vivo, that might not be reproducible ex vivo[200].

The analyses of the power spectrum density of infected erythrocytes yielded unreasonably high values for the apparent viscosity η_{RBC}, countering the fact the large amounts of haemoglobin are digested during parasite maturation[201]. Safran *et al*. argued that the spectrin-actin cytoskeleton can be considered as a rigid wall in regard to the fluid flow in-between the membrane and the cytoskeleton. This assumption is based on the fact, that the typical rearrangement time of spectrin fibers was found in the µs regime, while typical membrane fluctuations decay on a timescale of ms. One can assume that this description does not hold for *P. falciparum* infected erythrocytes and that their cytoplasm no longer resembles a homogeneous haemoglobin solution. However one can only speculate how the apparent viscosity η_{RBC} is influenced by the rigidity of the parasite or parasite structures like Maurer's clefts[37, 202].

The increase in harmonic confinement γ in uninfected erythrocytes of both haemoglobinopathies can be attributed to their abnormal cytoskeleton structure. The abnormal display of actin filaments in terms of length and arrangement (Figure 1.5) demand for a higher mean end-to-end length of spectrin filaments, leading to a spring hardening effect[203]. Therefore, propagating changes to the cytoskeleton caused by the parasite driven actin mining and spectrin rearrangement[194, 204, 205], might be responsible for the additional increase in harmonic confinement γ observed for all infected erythrocytes at the trophozoite stage. The increase in γ also coincided with the formation of knob structures, that can provide additional anchoring between the plasma membrane and the cytoskeleton (Figure 3.2). The investigation of a knobless phenotype allowed to estimate the contribution of the two different biological causes. In fact, the harmonic confinement γ only increased five-fold for the knobless variant compared to a ten-fold increase observed for knob developing types, compared to the value for uninfected erythrocytes.

Interestingly, there was a clear difference between HbAS and HbAC found for the harmonic confinement γ. Since scanning electron microscopy revealed similar knob sizes and knob densities for HbAS and HbAC (Figure 1.6, Supporting Figure 8.4), the differences in harmonic confinement γ require extended discussion. From simulations[206] one can deduce that few but large knobs, characteristic for HbAS and HbAC, create a similar harmonic confinement as many small knobs, characteristic for HbAA. This compensatory effect might account for comparable values of the harmonic confinement for HbAA and HbAC. Additionally, one can derive from simulations that the harmonic confinement correlates with the strength of

individual connectors[206]. The low harmonic confinement γ found in HbAS therefore could be explained by an overall weaker anchoring of individual knobs, although the underlying biological process is unknown and demands further studies.

At last, it should be noted that the changes observed for the membrane fluctuations in infected erythrocytes, were interpreted based solely on the basis of parasite driven changes of membranous and cytoskeletal structures, assuming thermal equilibrium conditions. However, the fluctuation spectrum is in fact influenced also by non-thermal (or active) processes[207]. Yet, flicker spectroscopy does not allow to deconvolute the active and thermal causes of fluctuation due to the limitation in time resolution. Active processes like the transfer of ions through the membrane via ion-pumps or the phosphorylation of the spectrin-actin network do contribute to the membrane fluctuation[208] and one cannot exclude that *P. falciparum* directly tempers with these processes. In fact it is well established that ionic currents are strongly altered by the induction of additional transporters and the increase permeability of the membrane, both of which are altered by *P. falciparum*[209].

4.1.5 Summary

Flicker spectroscopy revealed a continuous increase of host cell mechanical parameters during the intraerythrocytic development of *P. falciparum* in HbAA, HbAS and HbAC. The results suggested that the stiffening of infected erythrocytes, is predominantly based on the increase of membrane to cytoskeleton coupling by the knobs, visible as a suppression of membrane fluctuations in the low q regime. Therefore, all infected erythrocytes at the trophozoite stage should be exposed to splenic clearance. The membrane bending modulus was found to be significantly higher in haemoglobinopathic variants, possibly due to increased amounts of irreversibly oxidized haemichromes bound to membranes, which should have a negative effect on their cytoadhesion capabilities.

4.2 Biochemical composition of infected red blood cells

4.2.1 Background of quantitative scanning X-ray fluorescence microscopy

When a X-ray photon ($E_{\text{Photon}} > 100$ keV) passes through matter, it can interact with the electrons of an atom in several ways (Figure 4.10 a). Generally, one distinguishes scattering processes (elastic—Rayleigh, inelastic—Compton) from absorption processes (photoelectric effect). Interaction processes at higher photon energies ($E_{\text{Photon}} > 1.022$ MeV) can additionally lead to electron-positron pair production (not shown).

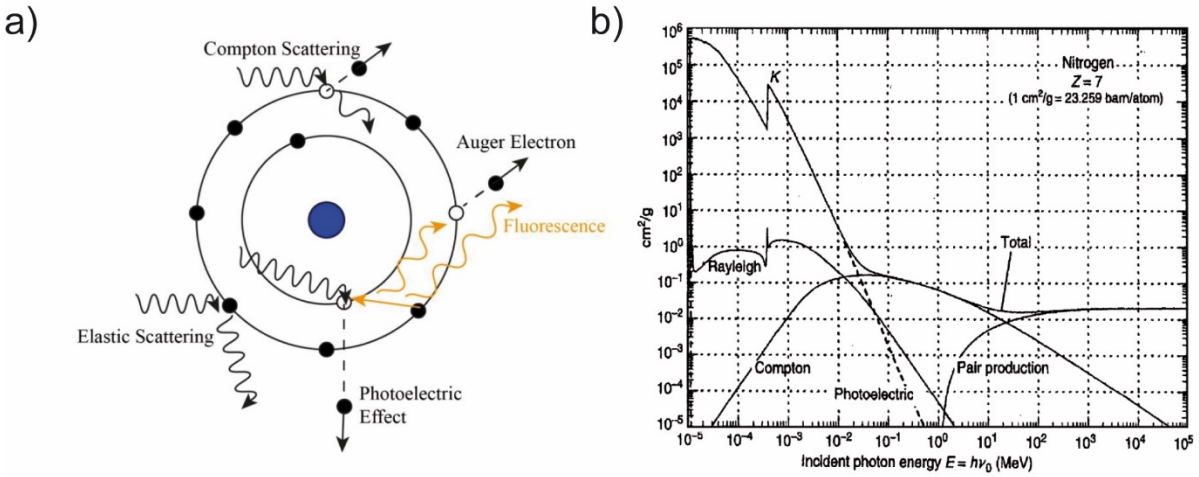

Figure 4.10 | X-ray photon interaction with electrons. (a) Schematic overview of interaction types between incident X-ray photons and the electrons of an atom (reproduced from Korytowski, 2016)[210]. (b) Mass attenuation coefficient μ/ρ as a function of the incident photon energy for nitrogen (reproduced from Carron, 2007)[211].

A mono energetic beam of photons with incident intensity I_0 traversing through a sample with thickness t and a material density of ρ will emerge with an intensity I_t following the Beer-Lambert law:

$$I_t = I_0 \cdot e^{-(\mu t)} = I_0 \cdot e^{-(\mu/\rho\, \rho t)}, \qquad 4\text{-}22$$

where μ denotes to the linear attenuation coefficient and the ratio μ/ρ defines the mass attenuation coefficient. The mass attenuation coefficient is related to the total cross section σ_{Total} per atom:

$$\mu/\rho = \sigma_{\text{Total}} \frac{N_A}{uA}, \qquad 4\text{-}23$$

where u ($= 1.66 \times 10^{-27}$kg) is the atomic mass unit, A is the relative atomic mass of the element, and N_A($= 6.022 \times 10^{-23}$ mol^{-1}) is Avogrado's number. The total interaction cross section σ_{Total} and therefore the mass attenuation coefficient is a function of the incident photon energy (Figure 4.10 b). The total cross section σ_{Total} is the superposition of the cross section of the different interaction paths:

$$\sigma_{\text{Total}} = \sigma_{\text{Photoelectric}} + \sigma_{\text{Compton}} + \sigma_{\text{Rayleigh}} + \sigma_{\text{Pair production}}\,. \qquad 4\text{-}24$$

X-ray fluorescence is a by-product of the photoelectric effect. Once an electron is removed from an inner shell (high binding energy), it can be replaced by an electron from an outer shell (low binding energy). The energy difference is compensated for by the generation of a characteristic fluorescence photon (Figure 4.10 a). Thereby, the energy of the fluorescence photon is a function of the element, and the participating energy states[212, 213, 214]. To be able to identify elements and their corresponding local densities a setup for "quantitative scanning X-ray fluorescence microscopy" typically requires:

- a highly brilliant X-ray source (high intensity and highly monochromatic)[215]
- a narrow beam size to increase spatial resolution[216, 217]
- a detector with high energy resolution and temporal resolution[212]
- a movable high precision sample stage

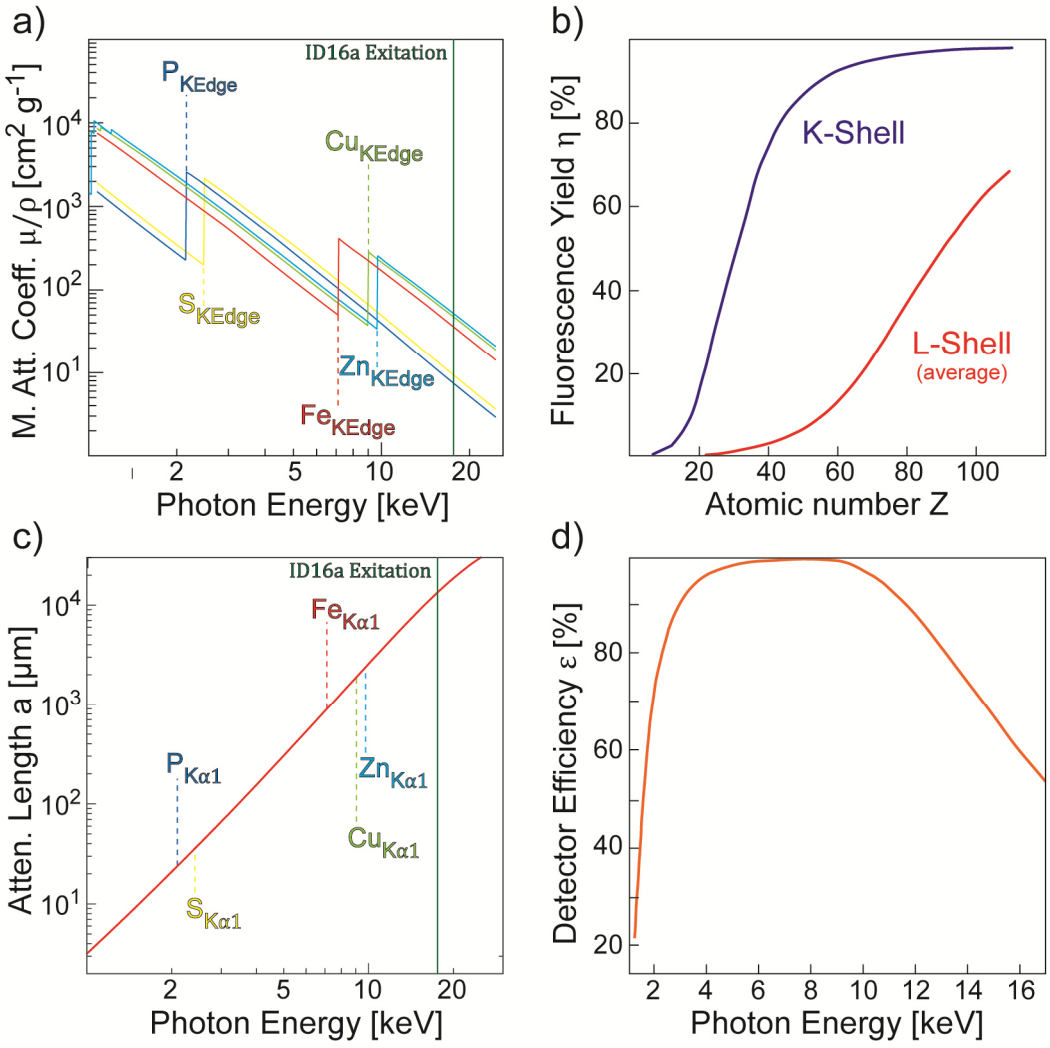

Figure 4.11 | Quantitative X-ray fluorescence. (a) Mass attenuation coefficient μ/ρ as a function of incident photon energy. The excitation beam energy for scanning X-ray fluorescence at ID16a was set to 17.05 keV[213, 214]. (b) Fluorescence yield η as a function of atomic number Z[218].(c) Attenuation length L for ice at a density of $\rho = 0.9167$ g cm^{-3} as a function of traversing photon energy[213, 214]. (d) Detector efficiency ε as a function of photon energy as given by the manufacturer.

In quantitative scanning X-ray fluorescence, a sample is continuously illuminated by a narrow beam. The sample movement speed, the dwell time/integration time and the beam size determine the resulting pixel size for the system. The detector signal formation for each element C^Z, denoted by the superscript Z, can be expressed for each pixel position (i, j) as:

$$C^Z(i,j) = I_0 \cdot \left(\frac{\mu}{\rho}\right)^Z \cdot uA \cdot \eta^Z \cdot e^{-\frac{L(i,j)}{a^Z}} \cdot \left(\frac{\Delta\Omega}{4\pi}\right) \cdot \varepsilon^Z \cdot \rho^Z(i,j) \cdot t(i,j), \qquad 4\text{-}25$$

where I_0 is the incident photon intensity, measured in parallel during the experiment. The number of fluorescent photons is proportional to the mass attenuation coefficient for each element $(\mu/\rho)^Z$ (Figure 4.11 a). Please note that although the photoelectric interaction is dominant at 17.05 keV (used during the experiment), the resulting detector counts need to be corrected for scattering events[219]. The creation of Auger electrons (Figure 4.10 a) acts as a parasitic process to the fluorescence emission, expressed by the fluorescence yield η^Z (Figure 4.11 b). The self-attenuation of generated fluorescent photons propagating a total length L through the ice matrix to reach the detector is expressed by the characteristic attenuation length a^Z. (Figure 4.11 c). Note, that the attenuation length for photons of the incident beam with an energy of 17.05 keV is several orders of magnitude higher than the sample thickness. The detector specific information are denoted by the solid angle $\Delta\Omega$ subtended by the detector and the element specific detector efficiency ε^Z (Figure 4.11 d).

4.2.2 Experimental realization

4.2.2.1 Sample preparation and cryo fixation

Synchronized infected erythrocytes at the trophozoite stage were enriched by magnetic column isolation (Chapter 2.7). Red blood cells were washed three times with phosphate buffered saline (PBS) supplemented with 10% (v/v) glycerol at pH 7.4. Droplets of cell suspension were applied onto silicon framed 5×5 mm^2 Si_3N_4 membrane grids (Silson Ltd, Southam, United Kingdom) followed by immediate freeze plunging into liquid ethane and transfered in liquid nitrogen[220]. Thereafter, grids were kept under cryo conditions for the whole experiment duration.

4.2.2.2 Quantitative scanning X-ray fluorescence microscopy

Quantitative scanning X-Ray Fluorescence (SXRF) microscopy was performed at the Nano-Imaging beamline ID16A-NI at the European Synchrotron Radiation Facility (ESRF, Grenoble, France). The beam was focused down to a beam size of about 30×30 nm^2 by a multilayer coated crossed Kirkpatrick-Baez mirror system 185 m distant from the source (Figure 4.12 a). The beamline was operated at a discrete energy of 17.05 keV provided by the multilayer monochromator setup with a high flux of $\sim 2 \times 10^{11}$ photons s^{-1}. Samples were measured under high vacuum (10^{-7} mbar) and cryogenic conditions. Quantitative SXRF microscopy was carried out with equivalent step sizes between 25-400 nm and dwell times of 50 ms or 100 ms. Fluorescence signals were recorded by a pair of 6-element silicon drift detectors (Ray

Spec Ltd., UK) positioned at an angle of α = 6° (Figure 4.12). Data were analyzed using the PyMCA software package developed at ESRF[219].

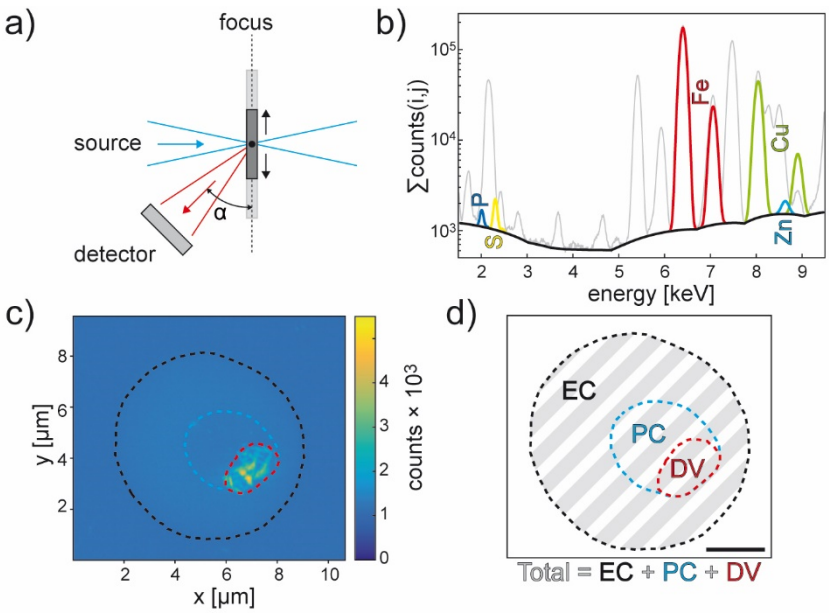

Figure 4.12 | Quantitative scanning X-ray fluorescence microscopy. (a) Samples are positioned inside the beam focus to minimize the size of the illumination footprint. Samples are screened by moving the sample in the plane perpendicular to the direction of illumination. (b) Summarized energy spectrum as determined by integrating the entire scanned area depicted in (c). Peaks correspond to the K_α and K_β lines for to the elements phosphorus (P), sulfur (S), iron (Fe), copper (Cu) and zinc (Zn). (d) Element counts are presented as a function of erythrocyte and parasite compartments, erythrocyte cytosol (EC, black), the parasite cytosol (PC, blue) and the parasite digestive vacuole (DV, red). Scale bar, 2 µm.

In a first step, the thickness of the matrix of vitrified ice was determined using the ratio of incident intensity I_0 and the transmitted intensity I_t (Equation 4-22) by illuminating a cell free area close to the cell of interest. The ice thickness was found to be below 5 µm for all samples.

The summarized energy spectra, detector counts as a function of photon energy (Figure 4.12 b), obtained for the entire scan area (Figure 4.12 c) were fitted using a polynomial-fit to confirm fit quality for the K-lines, L-lines and M-lines for all elements assumed to naturally occur in the sample or as part of the experimental setup (Al, P, Si, K, Ca, Cl, Co, Ni, Cr, Br and Au). Thereafter, the energy spectra were fitted pixel by pixel, including background correction, detector pile-up and element specific scattering. The element maps (Figure 4.12 c) allowed to determine the different erythrocyte and parasite compartments (Figure 4.12 d).

To convert detector counts per element into element density, the setup at ID16A NI was calibrated beforehand by the beam line staff using a XRF reference sample (RF7-200-S2371, AXO DRESDEN GmbH, Dresden, Germany) consisting of a thin silicon substrate covered with 1-3 atomic layers of different elements. Thereafter, the element specific density per pixel $\rho^Z(i,j)$ was calculated based on equation (4-25). To convert to absolute number $N(i,j)$ of atoms per pixel, $\rho^Z(i,j)$ had to be multiplied by the pixel area size. Finally, the absolute

number of atoms inside the cell was determined by subtracting the average number of atoms obtained from the cell free background $N_{\mathrm{cell}}(i,j) = N(i,j) - \langle N(i,j)\rangle_{\mathrm{bgr}}$.

4.2.3 Results

4.2.3.1 *P. falciparum* induced remodeling of wildtype erythrocytes

In a first step, the element composition of an uninfected wildtype erythrocyte was investigated. The corresponding element maps (Figure 4.13 a-d, upper panel) reveal a uniformly distribution of iron (Fe), sulfur (S), phosphorus (P) and zinc (Zn) throughout the erythrocyte cytosol. To allow for easier visual comparison of parasite induced alterations to the uniform element distributions, the percentage element counts are presented as a function of cell compartments (Figure 4.13 a-d, lower panel).

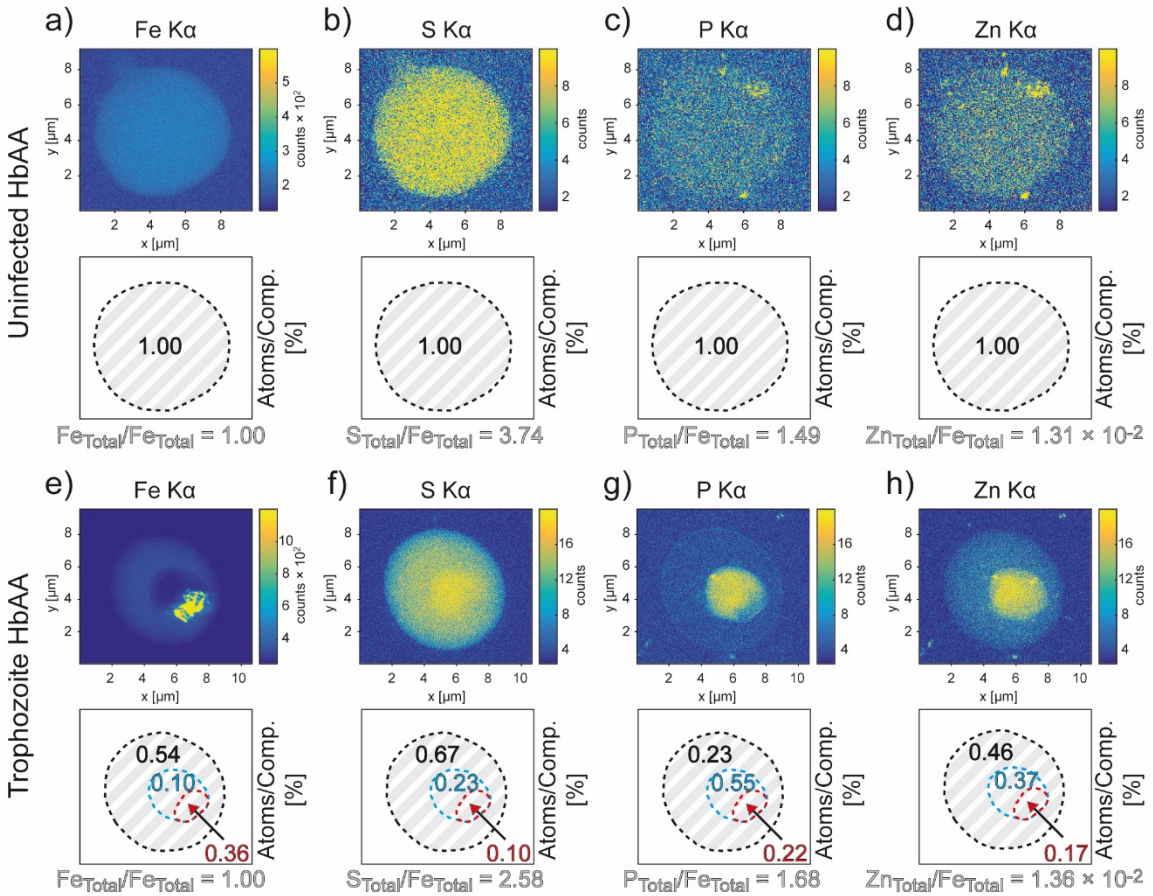

Figure 4.13 | Scanning X-ray fluorescence of uninfected and *P. falciparum* infected wildtype erythrocytes. Element maps for an uninfected erythrocyte (a-d, upper panel, pixel size 50 nm) and an infected erythrocyte at the trophozoite stage of infection (e-h, upper panel, pixel size 25 nm). The corresponding percentage element counts as a function of the cell compartment are depicted in the lower panels (erythrocyte cytosol (black), the parasite cytosol (blue) and the parasite digestive vacuole (red)).

Haemoglobin (Hgb) is the most abundant erythrocyte protein accounting for > 90% of the red blood cell dry mass[221]. Theoretically, each haemoglobin unit contributes 12 sulfur atoms, divided between methionine and cysteine with a ratio of 2:1, and 4 iron atoms, each complexed in a porphyrin group, to the fluorescence signal, resulting in an expected element

ratio of S_{Hgb}/Fe_{Hgb} ~3. The ratio of sulfur to iron inside the uninfected erythrocyte was in fact found to be higher with S_{EC}/Fe_{EC} = 3.74, attributed to other sulfur containing protein species and the level of free cytosolic cysteine [222]. Under the general assumption that the total iron count per cell Fe_{Total} is not affected by *P. falciparum* it can be used as a normalization factor, accounting for naturally occurring variations in cell size and as a tracker of element uptake or release. The absolute element counts are presented in Table 4-2).

Table 4-2 | Absolute element counts *N* as a function of cell compartment. The total element count *N* (Total) as determined for the entire projected cell area for (U) uninfected erythrocytes and (T) infected erythrocytes at the trophozoite stage. The element counts are presented for the erythrocyte cytosol (EC), the complete parasite occupied area (Parasite) and the corresponding subsections termed parasite cytosol (PC) and parasite digestive vacuole (DV)

Element	Compartment	HbAA		HbAS		HbAC	
N (×10⁶)		U	T	U	T	U	T
Fe	Total	818	1035	959	913	1001	761
	▶ EC	818	562	959	523	1001	355
	▶ Parasite	-	473	-	390	-	406
	▶ PC	-	104	-	28	-	63
	▶ DV	-	369	-	362	-	343
S	Total	3066	2675	3448	2758	3604	2457
	▶ EC	3066	1797	3448	1840	3604	1272
	▶ Parasite	-	878	-	919	-	1185
	▶ PC	-	608	-	558	-	486
	▶ DV	-	270	-	361	-	698
P	Total	1223	1742	423	2667	765	3438
	▶ EC	1223	402	423	676	765	500
	▶ Parasite	-	1340	-	1991	-	2938
	▶ PC	-	965	-	1277	-	1014
	▶ DV	-	375	-	714	-	1924
Zn	Total	10.7	14.1	5.9	12.9	10.1	8.0
	▶ EC	10.7	6.5	5.9	7.0	10.1	1.4
	▶ Parasite	-	7.6	-	6.0	-	6.6
	▶ PC	-	5.2	-	3.8	-	1.6
	▶ DV	-	2.4	-	2.2	-	5.0
Cu	Total	2.5	2.0	3.3	2.7	3.2	-
	▶ EC	2.5	1.2	3.3	1.5	3.2	-
	▶ Parasite	-	0.8	-	1.2	-	2.0
	▶ PC	-	0.4	-	0.6	-	0.7
	▶ DV	-	0.4	-	0.7	-	1.3

Remarkably, the cytosolic ratio of phosphorus to iron P_{EC}/Fe_{EC} = 1.49 was distinctly higher than the expected ratio calculated from literature values of $P_{EC, Lit}/Fe_{EC, Lit}$ = 0.9, indicating an additional uptake of phosphate from the culture medium[223, 224]. However, the ratio of zinc to iron of $Zn_{EC}/Fe_{EC} = 1.31 \times 10^{-2}$ was in good agreement with previous determinations of $Zn_{EC, Lit}/Fe_{EC, Lit} = 1.40 \times 10^{-2}$ [225]. The detection and quantification of intraerythrocytic copper posed a challenge. Thereby, the expected copper to iron ratio of only $Cu_{EC, Lit}/Fe_{EC, Lit} = 0.10 \times 10^{-2}$ was faced off against a large offset in the detector counts caused by several copper based components of the experimental setup[226]. As a consequence, the copper element maps do not show clear difference between background and cell occupied area (Supporting Figure 8.5). Nevertheless, the iron ratio of $Cu_{EC}/Fe_{EC} = 0.30 \times 10^{-2}$ was found to be comparable.

In clear contrast to the uninfected erythrocyte, the element maps of a wildtype erythrocyte at the trophozoite stage of infection exhibit clear differences in the element distribution in regard to the cell compartment (Fig 2. e-h). The iron signal was dominated by the haemozoin crystals containing roughly one third of the total number of iron atoms. Thereby, the level of haemoglobin digestion was comparable to trophozoite stage erythrocytes observed in previous studies[227].

Most amino acids stripped of each haemoglobin unit must have ended up outside the digestive vacuole resulting in a low ratio of sulfur to iron of S_{DV}/Fe_{DV} = 0.73, equivalent to a decrease of 80% compared to the reference values measured inside the uninfected erythrocyte cytosol. Indeed, amino acids were enriched inside the parasite vacuole, manifesting itself in a sulfur to iron ratio of S_{PC}/Fe_{PC} = 5.82. It should be noted that the changes to the total sulfur to iron ratio of S_{Total}/Fe_{Total} = 2.58, equal to a loss of ~31% amino acids, can be taken as a measure for the parasite driven amino acid efflux into the extracellular space. This efflux concurred with a reduced copper to iron signal of $Cu_{Total}/Fe_{Total} = 0.19 \times 10^{-2}$, equal to a loss of 28% of total copper. The change in element distribution was also prominent in the cases of phosphorus and zinc inside the parasite vacuole, reflected in the ~6 times higher phosphorus to iron ratio of P_{PC}/Fe_{PC} = 9.25 and the ~4 times higher zinc to iron ratio of $Zn_{PC}/Fe_{PC} = 4.98 \times 10^{-2}$, compared to values for the uninfected erythrocyte cytosol.

4.2.3.2 *P. falciparum* development in haemoglobinopathic erythrocytes

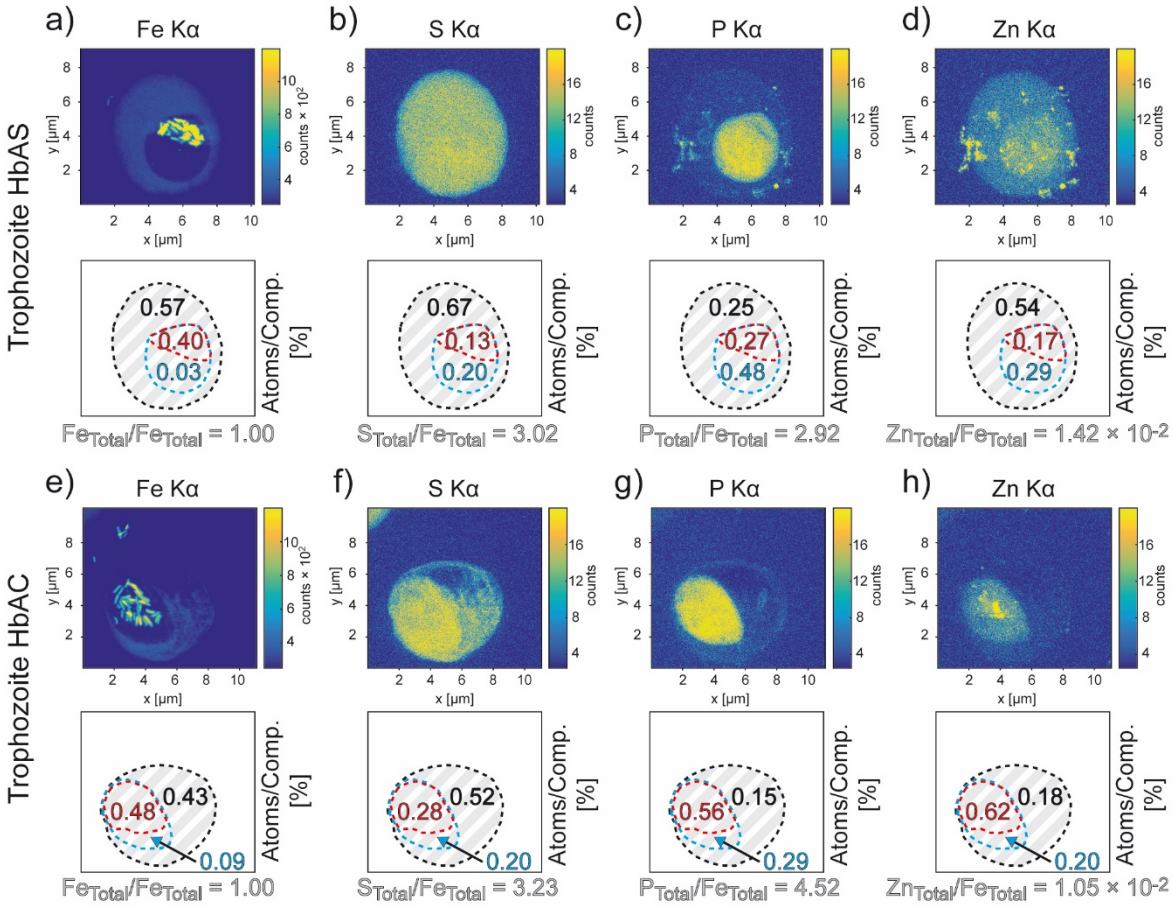

Figure 4.14 | Scanning X-ray fluorescence of infected haemoglobinopathic erythrocytes at the trophozoite stage. Element maps for HbAS (a-d, upper panel, pixel size 25 nm) and HbAC (e-h, upper panel, pixel size 25 nm). The corresponding percentage element counts as a function of the cell compartment are depicted in the lower panels (erythrocyte cytosol (black), the parasite cytosol (blue) and the parasite digestive vacuole (red)).

To assess the influence of haemoglobinopathies on the development of *P. falciparum*, firstly the differences between uninfected HbAS and HbAC and the wildtype erythrocyte were investigated. As expected, the element maps for both uninfected HbAS and HbAC depict the same homogeneous distribution for all considered elements (Supporting Figure 8.6). In fact, the calculated sulfur to iron ratios of S_{EC}/Fe_{EC} = 3.60 for both haemoglobinopathies were comparable to the wildtype, hinting towards specific element ratios for uninfected cells independent of size and blood type. This assumption was supported by the copper to iron ratios determined for HbAS of $Cu_{EC}/Fe_{EC} = 0.32 \times 10^{-2}$ and that of HbAC of $Cu_{EC}/Fe_{EC} = 0.34 \times 10^{-2}$. Surprisingly, further analysis revealed that the ratios of phosphorus to iron were strongly reduced for HbAS and HbAC in comparison to the wildtype erythrocyte, reaching down to a ~70% and ~50% lower value, respectively, although the cells were cultivated under identical conditions. Furthermore, the ratios of zinc to iron were found to be reduced with $Zn_{EC}/Fe_{EC} = 0.61 \times 10^{-2}$ for HbAS and $Zn_{EC}/Fe_{EC} = 1.12 \times 10^{-2}$ for HbAC.

In general, the element maps of infected erythrocytes of type HbAS (Fig. 3a-d) and HbAC (Fig.3 e-h) reveal similar changes to the element distribution as a function of cell compartment as observed for an infected wildtype erythrocyte (Fig. 2 e-h). The iron uptake into the digestive vacuole was comparable to that of the wildtype erythrocyte, confirming the temporal synchronicity of the parasite cultures. Interestingly, the haemozoin crystals were found to be loosely packed in the case of HbAS, a phenomenon even more pronounced in the case of HbAC. At the same time, the local ratios of sulfur to iron, accounting for the remaining amount of partially or undigested haemoglobin and free amino acids inside the digestive vacuole, were elevated for HbAS with S_{DV}/Fe_{DV} = 1.00 and for HbAC with S_{DV}/Fe_{DV} = 2.03. Additionally, the amount of released amino acids into the extracellular space was significantly lower for both HbAS and HbAC, reflected in the loss of total sulfur atoms of only ~11% and ~7%, respectively. In this context it is noteworthy, that in contrary to the wildtype trophozoite, the ratios of iron to sulfur inside the infected haemoglobinopathic erythrocytes cytosol were still comparable to their corresponding uninfected erythrocytes. This delayed efflux of amino acids coincides with the lower amount of released copper into the extracellular space. Additionally, both haemoglobinopathic trophozoites featured a high uptake of phosphate from the culture medium, resulting in a ~174% higher total phosphorus to iron ratio for HbAS of P_{Total}/Fe_{Total} = 2.92 and a ~269% higher value for HbAC of P_{Total}/Fe_{Total} = 4.52, than previously determined for the wildtype trophozoite.

4.2.4 Discussion

Quantitative scanning X-ray fluorescence microscopy allows to visualize the element composition of biological cells and tissues with high spatial resolution and trace level sensitivity[93, 94]. By embedding the target material into a thin layer of vitrified ice, using freeze plunging sample preparation, their native internal structures are preserved[228]. The synchrotron X-ray source provides a high-brilliance beam with an energy of 17.05 keV to be able to penetrate the entire sample thickness while minimizing the radiation damage.

The element composition of an uninfected wildtype erythrocytes was investigated to act as reference to validate the quantification process. As expected the elements iron, sulfur, phosphorus, zinc and copper were homogenously distributed throughout the erythrocyte cytosol. The absolute element counts, obtained by integrating the entire projected cell area, were in good agreement with literature values determined from population studies. Remarkably, phosphorus was found significantly increased, which suggested an additional uptake from cell medium. Erythrocyte phosphorus is mainly in cooperated in 2,3-Biphosphoglyceric acid and adenosine di-/triphosphate (ADP/ATP)[223]. The cell culture medium RPMI 1640 provides an additional phosphorus source in the form of 0.8 g/L Na_2HPO_4, in high abundance when compared to native serum phosphorus level that typically ranges between 0.03 and 0.06 g/L[229]. Moreover, additional Na_2HPO_4 supplementation was found to correlate positively with erythrocyte phosphorus and 2,3-Biphosphoglyceric acid levels[230].

Quantitative scanning X-ray fluorescence microscopy provided a snapshot of the complex intraerythrocytic metabolism of *P. falciparum* (Figure 4.15). Thereby, the iron amount stored in haemozoin crystals was used to determine a reference time point of parasite development[227]. The results indicate that liberated amino acids (sulfur marker), were transported out of the digestive vacuole either into the extracellular space or into the parasite cytosol, where they could act as raw material for the parasite driven protein synthesis[231]. Moreover, the high amount of phosphorus in the parasite vacuole suggested DNA/RNA or ADP/ATP, all of which are essential for the protein synthesis. The high sensitivity of the setup further provided quantitative data for the levels of zinc and copper inside the parasite vacuole. Both dietary elements act as enzymatic cofactors and are vital for the proliferation of the parasite[225, 232]. The reports on the possible toxic effect of excess copper for *P. falciparum* and the subsequent release of copper into the extracellular space were also confirmed by this study[226].

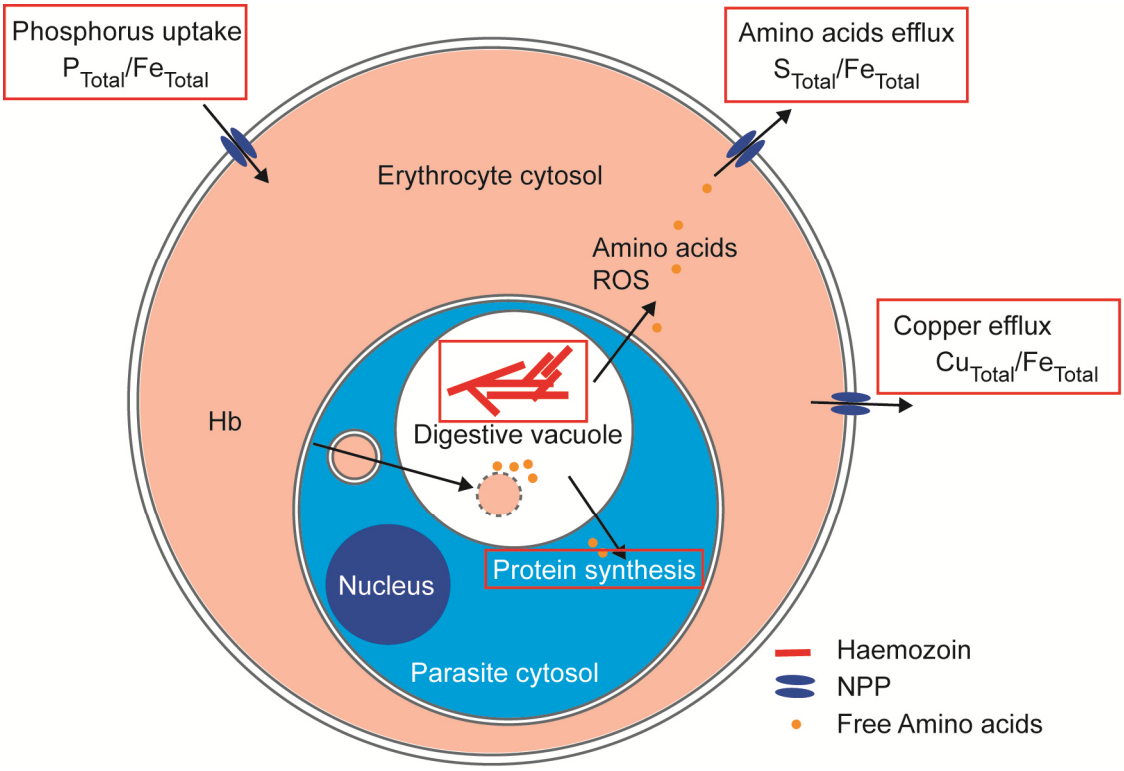

Figure 4.15 | *P. falciparum* intraerythrocytic metabolism. Quantitative scanning electron microscopy allows to track the digestion of haemoglobin and subsequent formation of haemozoin crystals inside the digestive vacuole. Colocalization of amino acids (sulfur marker), ATP/RNA (phosphor marker) and enzymatic cofactors (Zn, Cu) inside the parasite cytosol indicate parasite mediated protein synthesis. Comparison with uninfected erythrocytes allows to approximate different element uptakes and effluxes.

The analysis of uninfected haemoglobinopathic erythrocytes HbAS and HbAC revealed comparable cytosolic element values to uninfected wildtype erythrocytes except for a lower level of phosphorus and zinc. Unfortunately, the origin of these low values could not be conclusively identify within the scope of this thesis.

The results obtained for infected haemoglobinopathic erythrocytes confirmed the findings of a delayed protein expression and a delayed implementation of new permeation pathways across the infected erythrocyte membrane in iHbAS and iHbAC[34, 92]. Furthermore, the findings indicate, that the delay is already caused at the level of haemoglobin digestion. Although comparable amounts of haemoglobin were ingested into the digestive vacuole, reflected in comparable iron amounts, more amino acids, reflected in the higher sulfur amount, were still present. This finding raised the question, if haemoglobin is up taken but not digested efficiently, or if haemoglobin is digested but the amino acids are not transported into the parasite or the erythrocyte cytosol. Since the haemoglobin digestion is accompanied with high amounts of reactive oxygen species (ROS)[233] that might interfere with parasite metabolism, and large amounts of liberated amino acids, that exert osmotic pressure[34, 35], the first scenario seems more plausible to sustain parasite proliferation. Moreover, the undigested haemoglobin around individual haemozoin crystals might be responsible for their loose packing observed for iHbAS and iHbAC.

Interestingly, the phosphorus amounts were dramatically increased inside the digestive vacuole of both iHbAS and iHbAC compared to iHbAA. The parasites intraerythrocytic development relies on the uptake of inorganic phosphate from the host cytosol[234]. Yet, the amount of phosphate in iHbAS and iHbAC clearly exceeds the native supply available, as measured from the corresponding uninfected erythrocytes. A possible explanation would be an oxidative stress induced increase in the passive permeability of the host erythrocyte membrane[235, 236], which seems reasonable since both uninfected HbAS and HbAC generate higher quantities of reactive oxygen species[73].

4.2.5 Summary

Quantitative scanning X-ray fluorescence microscopy based on a synchrotron radiation source is a unique tool to investigate complex biological systems like the *P. falciparum* infected erythrocyte. Although many aspects of the parasite metabolism, like the haemoglobin digestion and subsequent storage of heme as haemozoin crystals, the parasite mediated uptake of enzymatic cofactors like zinc and copper, or the release of excess amino into the extracellular space, have been studied individually, the approach of this study allowed to develop a comprehensive quantitative snapshot of the metabolism without further chemical labeling.

The results clearly indicated a delayed digestion of HbAS and HbAC haemoglobin by the parasite and consequently a delayed development of new permeation pathways in the host erythrocyte membrane.

5 Conclusions

The aim of this thesis was the quantification of the cytoadhesive capabilities and the cell mechanical properties of *Plasmodium falciparum* infected human wildtype and haemoglobinopathic erythrocytes, to improve the understanding of the protective mechanism against severe malaria provided by haemoglobin polymorphisms.

The cytoadhesion of infected erythrocytes was probed using *in vitro* models of endothelial cell membranes on the basis of solid supported lipid bilayers functionalized with a well-defined density of ligands expressed by the average intermolecular ligand distances $\langle d \rangle$. This study shed light on the role of two ligand species, CD36 and ICAM-1, receptors that have been associated with severe cases of malaria.

In Chapter 3.2, the adhesion strength of infected wildtype (iHbAA) and infected sickle-trait erythrocytes (iHbAS) was quantified by the critical pressure of detachment $P_{\mathrm{crit}}(\langle d \rangle)$ through the application of picosecond laser pulse induced pressure waves. The experiments revealed cooperative binding characteristics for CD36/ICAM-1 and PfEMP1 and a binding-unbinding transition at low intermolecular ligand distances of $\langle d \rangle \sim 21 - 37$ nm. Since the native ligand distances of CD36 and ICAM-1 on endothelial cells are significantly higher with $\langle d \rangle > 110$ nm, the results suggested that parasite induced endothelial cell activation is necessary to generate firm adhesion conditions. In the case of CD36 by local clustering of CD36 and in the case of ICAM-1 by raising the expression levels of ICAM-1. Remarkably, the adhesion strength of iHbAS to CD36 was reduced compared to iHbAA, while the adhesion strength to ICAM-1 was comparable.

In Chapter 3.3, the adhesion of iHbAA and iHbAS was probed under physiological shear conditions between 0.03 and 0.3 Pa, mimicking the post capillary venules. The decrease in binding events with increasing shear stress suggested slip-bond behavior for both CD36 and ICAM-1. More importantly, the number of binding events was strongly reduced for iHbAS compared to iHbAA for both ligand species in the range of $\langle d \rangle = 7 - 67$ nm at shear stresses below 0.1 Pa. Furthermore, the adhesion strength of iHbAS to CD36 and ICAM-1, quantified by the critical shear stress of detachment τ_{crit}, was found to be significantly lower compared to iHbAA. Especially beyond $\langle d \rangle \sim 35$ nm, where τ_{crit} of iHbAS was in the range of physiological relevant shear stresses. Both findings suggested, that the number of binding events of iHbAS to human endothelial cells is not only strongly reduced but that the adhesion strength is too weak to sustain firm adhesion conditions under physiological relevant shear stresses, making them susceptible to splenic clearance.

In Chapter 3.4, label and contact free reflection interference contrast microscopy (RICM) was performed on adherent cells at $\langle d \rangle = 11$ nm for CD36 and ICAM-1 up to a shear stress of 1 Pa. RICM revealed a subpopulation of “heavy binders” in iHbAS, that resemble the binding characteristics of iHbAA, namely a shear induced growth in contact and adhesion area. This subpopulation might be responsible for similar parasitemia reported for HbAS children

suffering from malaria infection. Comparisons with publications of simulations performed on the adhesion characteristics of leukocytes led to the conclusion that shear induced cell deformations seem to be responsible for the growth in adhesion area. The results further suggested, that ICAM-1 acts as the stronger binding partner to PfEMP1 at high shear stress conditions beyond 0.5 Pa.

The mechanical properties of uninfected and infected erythrocytes at the ring and trophozoite stage of infection were probed using label-free and contact-free flicker spectroscopy for HbAA, HbAS and HbAC. The study was extended using a genetically altered knobless parasite strain.

In Chapter 4.1, the analysis of the thermally or non-thermally induced membrane fluctuations in Fourier space revealed a significant increase in the membrane bending modulus, the membrane tension, the harmonic cytoskeletal membrane confinement and the apparent cytosolic viscosity during parasite maturation. These fundamental alterations to the cell mechanics should lead to splenic clearance for all infected erythrocytes at the trophozoite stage. The combined results of iHbAA/iHbAS/iHbAC and the knobless parasite suggested that the confinement of membrane fluctuations in the low q regime is caused by the spectrin strain hardening effect due to cytoskeleton distortions and due to the additional anchoring of the membrane to the cytoskeleton via knobs. Interestingly, the bending modulus for iHbAS and iHbAC was found to be significantly higher compared to iHbAA, possibly due to irreversible membrane bound haemichromes. This higher bending modulus should have a negative contribution to the cytoadhesive capabilities of infected haemoglobinopathic erythrocytes.

In Chapter 4.2. the scope of this thesis was extended including quantitative scanning X-ray fluorescence microscopy of iHbAA, iHbAS and iHbAC at the trophozoite stage of infection. The quantification of element concentrations in different cell compartments of the infected allowed to track the uptake and efflux of key elements, thereby generating a comprehensive snapshot of the complex biochemical metabolism of *Plasmodium falciparum*. The results suggested a delay in haemoglobin digestion in HbAS and HbAC erythrocyte and a delayed development of new permeation pathways in the corresponding host cell membrane. The subsequent distorted protein trafficking has been associated with abnormal knob development and reduced PfEMP1 expression levels, and consequently reduced cytoadhesion, as observed in this study.

The results presented in this thesis demonstrate that *in vitro* cell membrane models are a powerful tool to quantify cell adhesion processes on the population level. Together with label-free and contact-free single cell techniques like reflection interference microscopy, flicker spectroscopy or quantitative scanning X-ray fluorescence microscopy, they provide a comprehensive picture of the protection mechanism of haemoglobin polymorphisms.

6 Perspectives

The presented study highlights the benefit of using *in vitro* endothelial cell membrane models based on functionalized lipid bilayers to study the interaction of infected erythrocytes with key ligands. Future design adaptations of the performed experiments might help to further understand the complex adhesion process.

An adhesion based microfluidic cell sorting experiment (Figure 6.1) might allow to further investigate the subpopulation of "heavy binders" (Chapter 3.3). The design is based on the experiments performed on neutrophils[237] and the theoretical sorting capability has already been investigated by Dasanna *et al*[238].

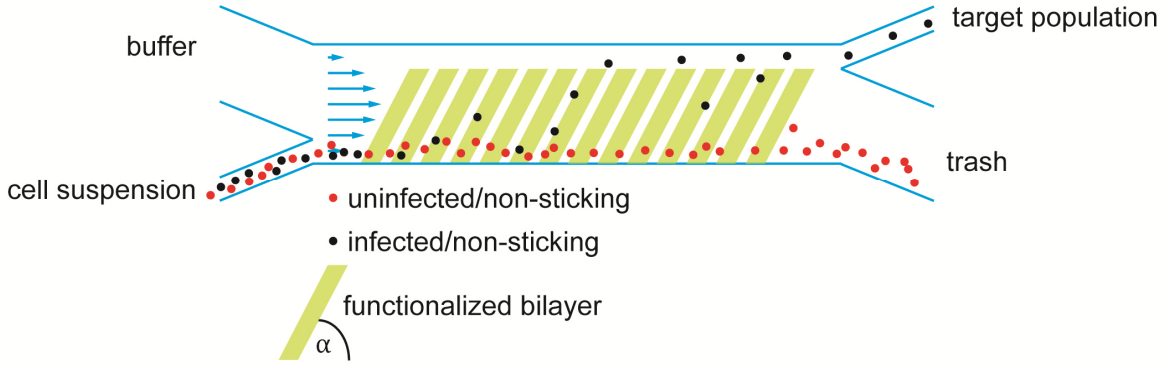

Figure 6.1 | Adhesion based cell sorting. Small patches of functionalized bilayer allow to sort sticking from non-sticking population as a function of intermolecular ligand distance $\langle d \rangle$, applied shear stress τ and inclination angle α. Non-sticking/non-interacting cells do not undergo displacement, while sticking cells are displaced stochastically by rolling along the stripe edges and therefore can reach the target population outlet.

The sorting system consists of a microfluidic chamber made from polydimethylsiloxane (PDMS) glued to a microscopy grade glass slide. Beforehand, specific areas of the glass are passivated by micro contact printing of BSA. Upon connection of channel and glass, stripes functionalized lipid bilayers are created as described earlier (Chapter 3.1).

The obtained results of this thesis indicated that firm adhesion conditions for infected erythrocytes have to be generated by the upregulation of ICAM-1 expression, based on the endothelial cell activation originating from loosely bound or shortly interacting infected erythrocytes.

Recent experiments performed on endothelial cells and corresponding computer simulations confirmed an increase interaction footprint of iHbAA compared to iHbAS or iHbAC[134], yet a direct quantification of the cell contact or adhesion footprint is not available. Reflection interference contrast microscopy has been successfully applied during this study to investigate the shear dependent change in adhesion area. The combination of an ultra-fast camera and a super luminescent diode might allow to record the contact and adhesion footprint of infected erythrocytes propagating along functionalized bilayers under physiological shear stress conditions.

7 Appendix I

7.1 Probing the effective interfacial interaction potential of zwitterionic polymer brushes based on reflection interference contrast microscopy of cell size particles

7.1.1 Introduction

Zwitterionic molecules feature both positive and negative charges and are of high abundancy in nature. Zwitterionic phospholipids like phosphatidylcholine and sphingomyelin-phosphocholine do in fact make up more than 50% of total lipids in a variety of animal tissues[239, 240]. Recently, zwitterionic polymers have gained importance in the field of material science as replacements for oligoethylene, since they provide excellent self-cleaning and antifouling capabilities, highly interesting properties for industrial applications[241, 242, 243]. Thereby, the surface-initiated controlled chain growth ("grafting from" method) can be used to create highly dense, defect-free polymer brush layers [244]. The antifouling properties of zwitterionic polymer brushes can be attributed to the excluded volume effect, the reduced gain in free energy observed during foulant adsorption and the strongly reduced dynamic friction coefficients[245, 246, 247].

One promising candidate to create these unique surface properties are polymer brushes presenting the zwitterionic molecule sulfobetaine as side chains. They provide unique hydration behaviors due to the intrinsic inter-chain pairing of zwitterions, termed anti-electrolyte effect. Moreover, their hydration radius was found to be tunable by the buffer concentration of NaCl, an effect also reported for different anions[248, 249]. These unique hydration characteristics are thought to be the origin of their excellent anti-fouling capabilities. Yet, little is understood how the interfacial potential of zwitterionic brushes is modulated in the presence of ions.

This study is based on the observation of cell size latex particles and osmotically tensed human erythrocytes performing vertical Brownian motion above glass substrates coated with poly(sulfobetaine) brushes. The height fluctuations were recorded based on label and contact free reflection interference contrast microscopy (RICM)[250, 251, 252]. The fluctuation amplitudes were analyzed assuming thermal equilibrium conditions to calculate the harmonic effective interfacial potential $V(\Delta h)$[253]. The aim of this study is the precise quantification of the ion specific modulation of $V(\Delta h)$ caused by Na^+, K^+ and $N(CH_3)_4^+$ and Ca^{2+} at different concentrations, keeping Cl^- as a constant counter ion. The salts were chosen following the classical Hofmeister series[254]:

$$CO_3^{2-} < SO_4^{2-} < H_2PO_4^- < F^- < Cl^- < Br^- < NO_3^- < I^- < ClO_4^- < SCN^-,$$

$$N(CH_3)_4^+ < NH_4^+ < Cs^+ < Rb^+ < K^+ < Na^+ < Li^+ < Mg^{2+} < Ca^{2+}.$$

With $N(CH_3)_4^+$ exhibiting kosmotrope character (left side) and Na^+, K^+ being more chaotropic in nature and Ca^{2+} acting as a representative of extremely chaotropic ion specimens (right

side). To shed light on the pairing of sulfobetaine side chains, the vertical Brownian motion of beads was also tracked dependent on an increasing concentration of dissolved free sulfobetaine molecules acting as “competitors” identical to the structure of the side chains.

7.1.2 Probing the effective interfacial potential with cell size spherical particles

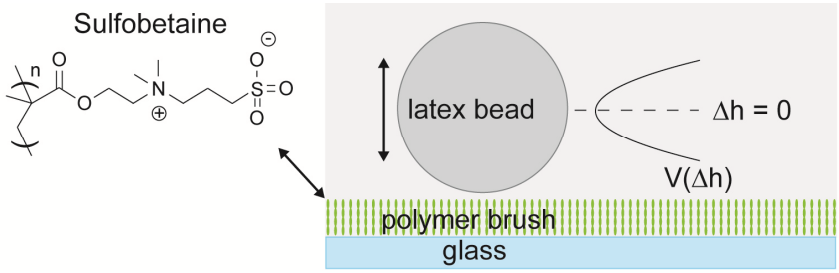

Figure 7.1 | Probing the effective interfacial potential $V(\Delta h)$ based on the height fluctuation Δh analysis of cell size spherical particles. The polymer brush constitutes of monomers carrying zwitterionic sulfobetaine sidechains.

The equation of motion for a particle undergoing vertical Brownian motion (Figure 7.1) in an effective interfacial potential $V(\Delta h)$ can be described by a Langevin equation:

$$m\frac{\partial^2\Delta h}{\partial t^2}+\gamma\frac{\partial\Delta h}{\partial t}+\frac{\partial V}{\partial\Delta h}=F_{\text{stoch}}, \qquad 7\text{-}1$$

where m is the particle mass, γ the hydrodynamic friction coefficient, Δh the relative particle position, and F_{stoch} the representation of the thermally driven stochastic forces acting on the particle. The second term describes the frictional force F_{fric} and can be expressed by the Reynolds equation[255]:

$$F_{\text{fric}}=\gamma\frac{\partial\Delta h}{\partial t}, \text{and } \gamma=6\pi\eta_{\text{eff}}\frac{R^2}{h}, \qquad 7\text{-}2$$

where η_{eff} is the effective shear viscosity of the system, h the absolute distance between the particle and the surface and R the radius of the latex particle. From the radius of the used latex beads $R = 5$ µm, the observed average bead velocity of $\partial\Delta h/\partial t \approx \frac{10^{-8}}{0.03}\,\text{ms}^{-1}$, the density of the latex particle $\rho = 1.04\ \text{g cm}^{-3}$and the viscosity of water $\eta_{\text{w}} = 1\ \text{mN m}^{-2}\text{s}$, one can estimate the Reynolds number Re of the system to be $Re \leq R(\partial\Delta h/\partial t)\rho\eta_w^{-1} \sim 10^{-4}$ [255]. Since $Re \ll 1$ one can assume the particle movement to be overdamped, therefore the first term in equation (7-1) can be neglected[256].

Since typically only small height fluctuations in the range of $\Delta h \leq 30$ nm are observed , the effective interfacial can be approximated in first order as harmonic [257]:

$$V(\Delta h)=\frac{1}{2}\frac{\partial^2 V}{\partial\Delta h^2}\bigg|_{\langle h\rangle_t}(\Delta h-\langle\Delta h\rangle)^2=\frac{1}{2}V''\Delta h^2 \qquad 7\text{-}3$$

The corresponding autocorrelation function of the height fluctuation can be calculated within the framework of the fluctuation dissipation theorem to be:

$$\langle \Delta h(\delta t)\Delta h(0)\rangle \approx \langle \Delta h^2(0)\rangle e^{-\frac{\delta t}{\tau}}, \text{where } \tau = \frac{\gamma}{V''} = \frac{6\pi\eta_{\text{eff}}R^2}{\langle h\rangle V''} \quad 7\text{-}4$$

The mean square amplitude of fluctuation can be expressed under thermal equilibrium conditions:

$$\langle \Delta h^2(0)\rangle = \frac{k_{\text{B}}T}{V''}. \quad 7\text{-}5$$

The probability function of fluctuation $P(\Delta h)$ should follow a Boltzmann's distribution [250, 251, 252]:

$$P(\Delta h) \propto e^{\left(-\frac{V(\Delta h)}{k_{\text{B}}T}\right)}, \text{or } V(\Delta h) = -k_{\text{B}}Tln\big(P(\Delta h)\big) + \text{const} \quad 7\text{-}6$$

7.1.3 Experimental realization

7.1.3.1 Materials

Throughout this study ultra-pure water (Millipore Inc, Billerica, MA) was used for all experimental conditions. Chemicals were purchased from Wako Pure Chemical Industries (Osaka, Japan), Merck (Darmstadt, Germany), Carl Roth (Karlsruhe, Germany) or Sigma-Aldrich (Neu-Ulm, Germany) unless stated otherwise. Latex particles ($R \approx 5$ µm, $\rho = 1.04$ g/cm^3) were purchased from Macherey-Nagel (Düren, Germany). Poly (sulfobetaine) (poly[3-(N-2-methacryloyloxyethyl-N,N-dimethyl)ammonatopropanesulfonate]) brushes were prepared by surface-initiated atom transfer radical polymerization on glass plate and characterized using atom force microscopy by Dr. Yuji Higaki (Kyushu University, Fukuoka, Japan) [152, 258]. Adult blood was obtained from healthy donors following the ethical guidelines of the Joint Ethics Committee of IFLMS, iCeMS and CiRA, Kyoto University, Japan. RICM observations of tensed erythrocytes were exclusively performed by Dr. Akihisa Yamamoto and Dr. Ryo Murakami, Kyoto University, Japan.

7.1.3.2 Reflection contrast interference microscopy

Latex particles were incubated in bovine serum albumin (BSA, 1mg/mL) for 15 min prior to avoid non-specific adhesion. Human erythrocytes were deformed into "osmotic spherocytes" using osmotic pressure imbalance (83 mM NaCl, pH 6.4). Experiments were performed at room temperature. The utilized RICM setup was described in detail in Chapter (3.4.2.1). Quasi-perpendicular illumination was obtained by setting the Illumination Numerical Aperture (INA) to 0.48, thereby increasing the contrast for higher order minima and maxima. Images sequences consisting of 1000-2000 frames at an exposure time of 30 ms were recorded and subjected to the analyses. All analyses were performed using self-written routines in Matlab (R2014b)

7.1.3.3 Determination of the height fluctuation profiles based on reflection interference contrast microscopy

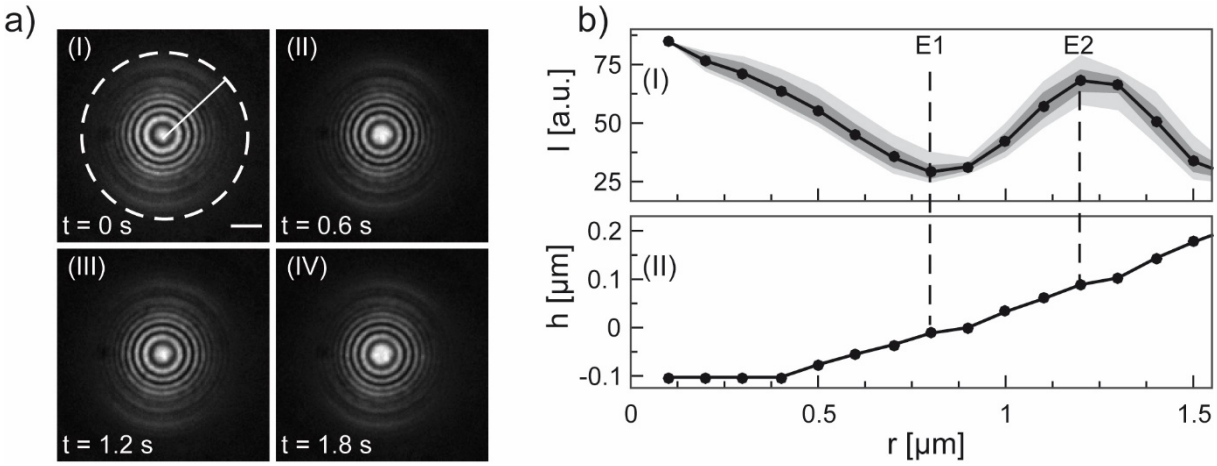

Figure 7.2 | Determination of height fluctuations of a spherical object. (a I-IV) Successive RICM images of a latex particle hovering on the surface of a poly(sulfobetaine) brush (15 mM NaCl, buffered with 10 mM HEPES, pH 7.4). (a I) Radial intensity profiles were obtained along the indicated solid line followed by an azimuthal integration (dashed circle). (b I) The mean radial intensity (data points and black line) and the intensity values within the standard deviation (dark grey) after integration for a single frame. The total range of observed intensity values is depicted in light grey. (b II) Conversion of the mean radial intensity profile into the corresponding height profile based on equation (7-7). Scale bar, 5 µm.

The center of mass for each frame was calculated applying an edge detection filter to correct for lateral drifts. For each frame, two consecutive maximum/minimum positions of the mean radial intensity profile (E1, E2) closest to the center were selected (Figure 7.2). Due to the quasi-perpendicular illumination the simplified theory of RICM can be applied, allowing the conversion of radial intensity I to relative height Δh_{pp} for all pixel positions (pp) between E1 and E2:

$$\frac{2I_{\mathrm{pp}} - (I_{\mathrm{E1}} + I_{\mathrm{E2}})}{I_{\mathrm{E1}} - I_{\mathrm{E2}}} = \cos\left(4\pi n_{\mathrm{buffer}} \frac{\Delta h_{\mathrm{pp}}}{\lambda}\right) \qquad 7\text{-}7$$

The relative bead position $\Delta h(t) = \Delta h_{\mathrm{pp}}(t) - \langle \Delta h_{\mathrm{pp}} \rangle_t$ was calculated for all frames. Thereafter, equation (7-6) was applied to derive the effective interfacial interaction potential $V(\Delta h)$.

7.1.4 Results

7.1.4.1 Influence of mono- and divalent ions on the effective interfacial interaction potential

In a first step, the interfacial potential was probed as a function of the concentration of monovalent salts Na^+, K^+ and $N(CH_3)_4^+$. The observed mean square amplitude of the height fluctuation monotonically decreased for all ion species with increasing salt concentrations from 1.5 mM up to 150 mM (Figure 7.3 a-c, (I-III), Table 7-1). The global shapes of the resulting normalized effective interfacial potentials $V(\Delta h)/k_{\mathrm{B}}T$ were well approximated harmonically (Figure 7.3 a-c, (IV)), Table 7-1) confirming the validity of Derjaguins's

approximation for weak interactions.[257] As predicted by equation (7-6) the decrease in fluctuation amplitudes was inversely correlated to the sharpening of $V(\Delta h)$, expressed by the significant increase in the spring constant V'' (Table 7-1). Additionally, the corresponding autocorrelation functions decreased faster with increasing salt concentrations (Figure 7.3 a-c, (V), Table 7-1) and were all well fitted as a single exponential function following equation (7-4).

Although the general observed tendencies were similar for all ion species, the mean square amplitude of fluctuation (MSA) in $N(CH_3)_4^+$ were 2-3 times smaller than the corresponding values obtained for Na^+, K^+. Consequently, the spring constants of $V''_{N(CH_3)_4Cl} \sim 20 \times 10^{-22}$ J nm^{-2} were found to be nearly an order of magnitude higher than the corresponding values for Na^+, K^+ (Table 7-1). Additionally, the characteristic decay times τ reached down to the experimental resolution limit of $\tau_{RL} \approx 0.01$ s.

Table 7-1 | Summary of values for the spring constant V'', the characteristic decay time τ, and the hydrodynamic friction coefficient γ for NaCl, KCl and $N(CH_3)_4Cl$.

	c [mM]	MSA [nm^2]	V''[10^{-22} J/nm^2]	τ [s]	γ [10^{-22} Js/nm^2]
NaCl	1.5	210 ± 89	2 ± 1	0.13 ± 0.07	0.28 ± 0.17
	15	86 ± 49	3 ± 1	0.08 ± 0.03	0.27 ± 0.11
	150	8 ± 3	7 ± 1	0.05 ± 0.02	0.30 ± 0.18
KCl	1.5	160 ± 80	1 ± 0.5	0.20 ± 0.01	0.23 ± 0.05
	15	130 ± 72	1 ± 0.5	0.16 ± 0.03	0.19 ± 0.04
	150	75 ± 33	4 ± 1	0.03 ± 0.01	0.11 ± 0.03
$N(CH_3)_4Cl$	1.5	6 ± 4	17 ± 4	0.01 ± 0.01	0.15 ± 0.12
	15	3 ± 2	21 ± 4	<0.01	<0.1
	150	3 ± 2	23 ± 4	<0.01	<0.1

Table 7-2 | Summary of values for the spring constant V'', the characteristic decay time τ, and the hydrodynamic friction coefficient γ for $CaCl_2$ and Sulfobetaine.

	c [mM]	MSA [nm^2]	V''[10^{-22} J/nm^2]	τ [s]	γ [10^{-22} Js/nm^2]
$CaCl_2$	1.5	2 ± 1	25 ± 5	<0.01	<0.1
	15	3 ± 1	15 ± 4	<0.01	<0.1
	150	5 ± 2	10 ± 2	0.01 ± 0.01	0.10 ± 0.10
Sulfobetaine	1.5	10 ± 4	6 ± 2	0.04 ± 0.01	0.18 ± 0.15
	15	10 ± 4	7 ± 3	0.04 ± 0.01	0.20 ± 0.09
	150	6 ± 3	12 ± 4	0.03 ± 0.01	0.28 ± 0.14

In clear contrast, the experiments performed as a function of divalent ion concentrations using Ca^{2+}, revealed an opposite behaviour (Figure 7.4 a,Table 7-2). The fluctuation amplitudes increased as a function of salt concentration, while the harmonic confinement

were broadened. The range of spring constants of $V''_{CaCl_2} \sim 20 \times 10^{-22}\,\mathrm{J\,nm^{-2}}$ was comparable to that of $N(CH_3)_4Cl$. Similar to the case of $N(CH_3)_4Cl$, the characteristic decay times τ were below the resolution limit of the setup.

7.1.4.2 Influence of Zwitterionic Pairing

Experiments were performed at different concentrations of free sulfobetaine, to see the effect of the zwitterionic pairing in the presence of competitors. The vertical Brownian motion was strongly influenced by the presence of non-detergent sulfobetaine in solution. The mean square amplitudes of the height fluctuation were found to be almost an order of magnitude smaller than those in the presence of NaCl or KCl at the corresponding concentrations. Analogue to the monovalent ions, the MSA decreased with increasing sulfobetaine concentration. Accordingly, the spring constant reached as high as $V''_{\mathrm{Sulfobetaine}} \sim 12 \times 10^{-22}\,\mathrm{J\,nm^{-2}}$ at 150 mM sulfobetaine. The autocorrelation function showed only minor dependencies on the sulfobetaine concentration, yet the hydrodynamic friction coefficient γ calculated from equation (7-4) significantly increased with increasing concentration of non-detergent sulfobetaine up to $\gamma_{\mathrm{Sulfobetaine}} = 0.28 \times 10^{-22}\,\mathrm{Js\,nm^{-2}}$ at 150 mM sulfobetaine.

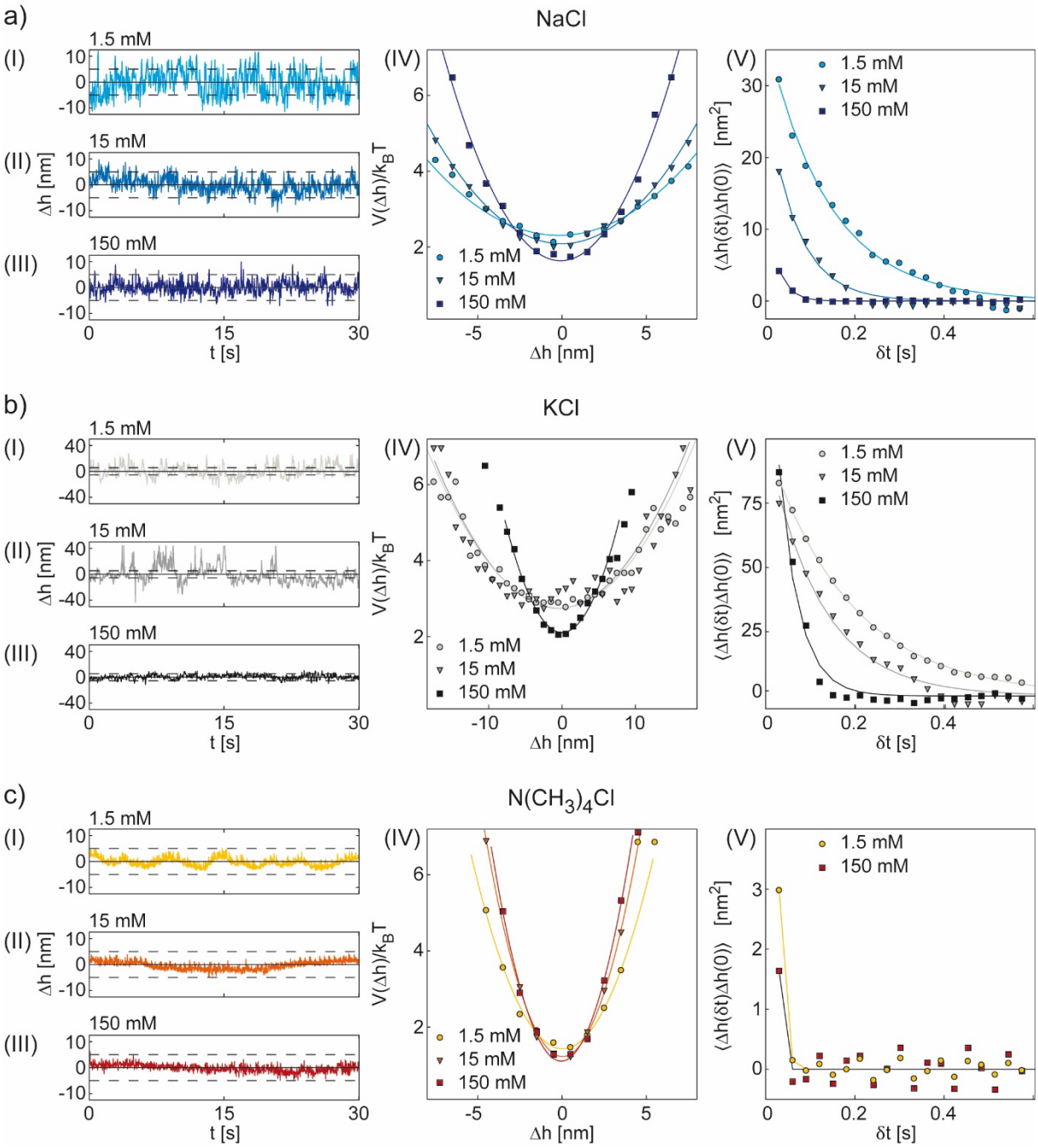

Figure 7.3 | Changes in the effective surface potential as a function of mono-valent ion concentrations. (a I-III) Height fluctuations $\Delta h(t)$ of representative latex particles calculated for 1.5 mM, 15 mM and 150 mM concentrations of NaCl. (a IV) Normalized interfacial potentials $V(\Delta h)/k_BT$ and fits based on the harmonic assumption described by equation (7-3).(a V) Autocorrelation function of the height fluctuation $\langle \Delta h(\delta t)\Delta h(0)\rangle$ and corresponding single exponential fits following equation (7-4).(b I-V) Corresponding figures for a representative data set for different concentrations of KCl. Please note the different axis ranges. (c I-V) Corresponding figures for a representative data set for different concentrations of $N(CH_3)_4Cl$.

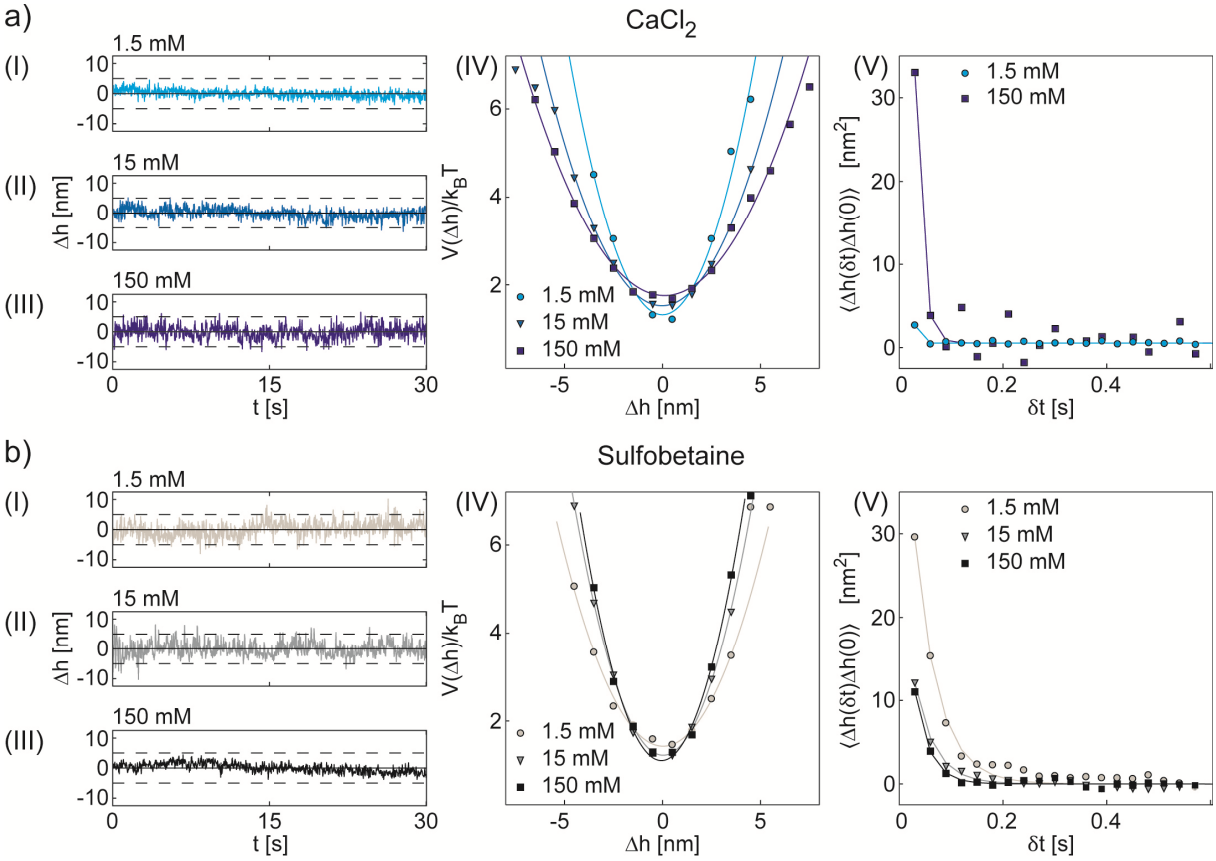

Figure 7.4 | Changes in the effective surface potential as a function of $CaCl_2$ and sulfobetaine concentrations. (a I-III) Height fluctuations $\Delta h(t)$ of representative latex particles calculated for 1.5 mM, 15 mM and 150 mM concentrations of $CaCl_2$. (a IV) Normalized interfacial potentials $V(\Delta h)/k_BT$ and fits based on the harmonic assumption described by equation (7-3).(a V) Autocorrelation function of the height fluctuation $\langle \Delta h(\delta t)\Delta h(0)\rangle$ and corresponding single exponential fits following equation (7-4).(b I-V) Figures for a representative data set for different concentrations of free sulfobetaine.

7.1.4.3 Probing the effective interfacial potential using osmotic spherocytes

The excellent antifouling capability of zwitterionic polymers leads to the suppression of nonspecific interactions with proteins and lipid vesicles[259, 260]. To quantify this capability for zwitterionic sulfobetaine brushes, the experiments were conducted using human erythrocytes.

Healthy erythrocytes are highly deformable cell types and naturally show large thermally and non-thermally driven membrane fluctuations. In order to decouple these fluctuations from the vertical Brownian motion, erythrocytes were tensed under hypotonic conditions to create osmotic spherocytes (OS) with strongly reduced membrane fluctuations. The observed height fluctuations on poly(sulfobetaine) brushes were distinctly higher than those recorded during the reference measurements on pure glass substrates (Figure 7.5 (I), Table 7-3).

In fact, the osmotic spherocytes were only very loosely confined on the polymer brush as indicated by the low spring constant of $V''_{\mathrm{OS,brush}} \sim 1 \times 10^{-22}$ J nm^{-2} (Figure 7.5 (II), Table 7-3). Moreover, a very slow decay of the autocorrelation was observed (Figure 7.5 (III), Table

7-3), leading to a hydrodynamic friction coefficient $\gamma_{OS,sulfobetaine}$ below the resultion limit of the setup.

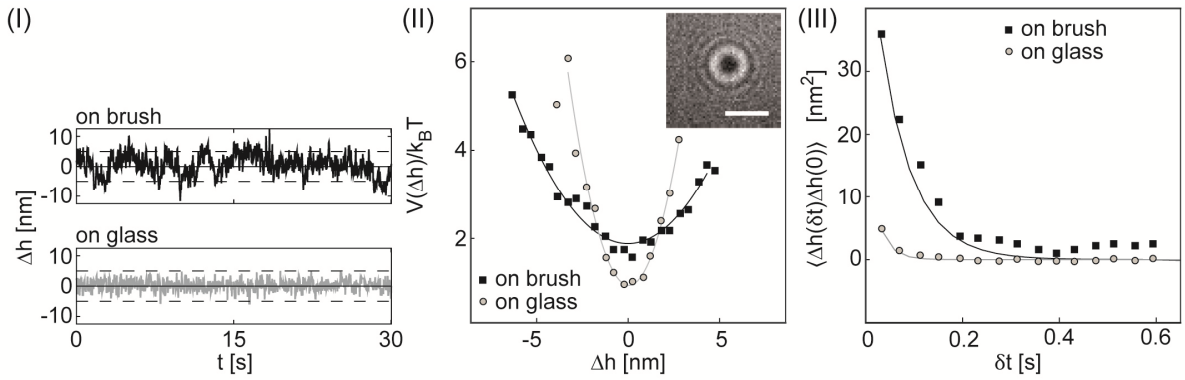

Figure 7.5 | Osmotic spherocytes on poly(sulfobetaine) brushes and bare glass substrates passivated with BSA. (I) Height fluctuations $\Delta h(t)$ of representative osmotic spherocytes. (II) Normalized interfacial interaction potential $V(\Delta h)/k_BT$ and fits based on the harmonic assumption described by equation (7-3). Inset depicts a raw data image obtained by RICM of an osmotic spherocytes on glass. (III) Autocorrelation function of the height fluctuation $\langle \Delta h(\delta t)\Delta h(0)\rangle$ and corresponding single exponential fits following equation (7-4).

Table 7-3 | Summary of values for the spring constant V'',the characteristic decay time τ, and the hydrodynamic friction coefficient γ for osmotic spherocytes.

substrate	MSA [nm²]	V''[10^{-22} J/nm²]	τ [s]	γ [10^{-22} Js /nm²]
poly(sulfobetaine) brush	97 ± 103	1 ± 1	0.14 ± 0.09	<0.1
glass	7 ± 4	10 ± 5	0.02 ± 0.02	0.20 ± 0.19

7.1.5 Discussion

Previous studies based on light scattering suggest an monotonic increase in the hydrodynamic radius of poly(sulfobetaine) as a function [NaCl] beyond a critical concentration $c^* = 74$ mM [261]. Experiments based on specular neutron reflectivity further revealed an increase in the brush to electrolyte interface diffusivity beyond [NaCl] $> c^*$ [244] Corresponding density profiles of poly(sulfobetaine) brushes reveal a poorly swollen inner layer and a highly swollen diffusive outer layer.

Interestingly, brushes based for example on poly(phosphocholine) exhibit neither changes in hydrodynamic radius nor in density profiles in the range of [NaCl] $= 74$ mM $-$ 5mM, thereby emphasizing the unique properties of poly(sulfobetaine) brushes. Unfortunately, the underlying molecular mechanisms that evoke such differences are not explained up to date.

V'' was found to monotonically increase for increasing [NaCl] in the range of 1.5 mM to 150 mM (Figure 7.6, Table 7-1). In fact, the change was most prominent up to [NaCl] $=$ 150 mM clearly beyond $c^* = 74$ mM. Both $N(CH_3)_4Cl$ and KCl exhibited a similar tendency (Figure 7.6, Table 7-1), and the resulting V'' provide a clear sequence:

$$V''_{KCl} < V''_{NaCl} \ll V''_{N(CH_3)_4Cl},$$

with $V''_{N(CH_3)_4Cl}$ being almost an order of magnitude larger than those for KCl and NaCl. $N(CH_3)_4^+$ is in the kosmotrope regime according to the Hofmeister series. If the ion specificity is based solely on difference in solvation entropy, one would expect direct neighbours such as K^+ and Na^+ to show similar properties. Indeed the observed V'' were comparable at all considered salt concentrations for K^+ and Na^+. Therefore, one would expect that specimen with even higher chaotropic character such as $CaCl_2$ to continue the observed trends.

Yet, the spring constant V''_{CaCl_2} for $CaCl_2$ showed the opposite behaviour, significantly decreasing with increasing salt concentration (Figure 7.6, Table 7-2). Moreover, the observed range of $V''_{CaCl_2} = 10 - 21 \times 10^{-22}$ J nm^{-2} was more than double than the range obtained for KCl and NaCl. Therefore, one can conclude that monovalent cations and Ca^{2+} must interact differently with the sulfobetaine side chains, possibly by cross-bridging of anionic sulfate moieties by Ca^{2+}. A further extension of the study to include other divalent cation species, or ions with even higher valence might provide deeper insight into the underlying physical mechanism.

To shed light on the anti-electrolyte effect, the effective interfacial interaction potential was probed as a function of free sulfobetaine. The confinement due to free sulfobetaine was found to be higher than that of NaCl or KCl but lower than that of $N(CH_3)_4Cl$ at corresponding concentrations. Remarkably, the characteristic decay time τ did not change significantly as a function of [sulfobetaine]. Yet, the hydro dynamic friction coefficient strongly increased with higher concentrations of free sulfobetaine reaching $\gamma_{Sulfobetaine} = 0.28 \times 10^{-22}$ Js nm^{-2}. Such a tendency was only observed for sulfobetaine, suggesting the intercalation of sulfobetaine molecules into the poly(sulfobetaine) brush, disturbing the zwitterionic pairing.

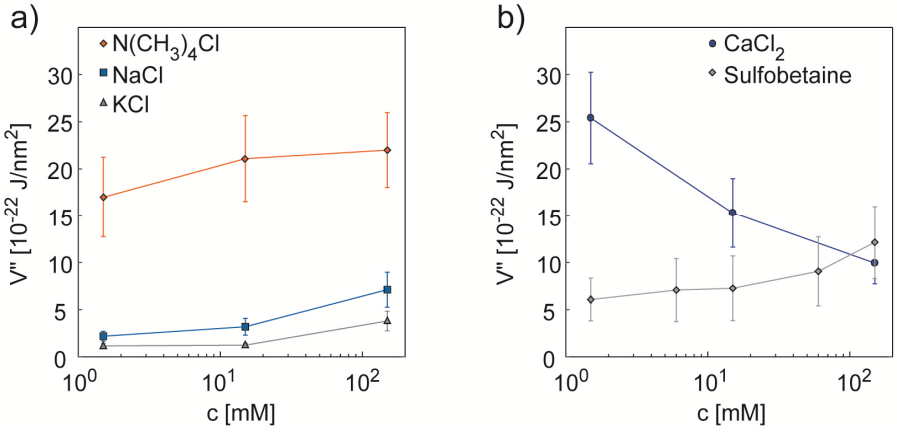

Figure 7.6 | Summarized values for the spring constant V''as a function of ion concentration. (a) Increase in V'' with increasing concentration of monovalent ions (Na^+, K^+ and $N(CH_3)_4^+$. (b) Decrease in V'' with increasing concentration of divalent ions (Ca^{2+}).

The excellent anti-fouling capability of zwitterionic-polymers prevents non-specific interactions with proteins and lipid vesicles [259, 260]. This property has been attributed to the

hydration with “freezing-bound” or “intermediate” water molecules [262, 263]. Yet, the cell-surface interactions modulated by zwitterionic polymer brushes were not quantified yet. The obtained results on osmotic spherocytes confirm that zwitterionic polymer brushes significantly soften the interfacial interaction potential and strongly reduce the hydrodynamic friction (Table 7-3). In contrast, the control experiments on bare glass revealed a strong vertical confinement with a roughly one order higher spring constant of $V''_{\mathrm{OS,glass}} \sim 10 \times 10^{-22}\ \mathrm{J\,nm^{-2}}$ and a hydrodynamic friction coefficient of $\gamma_{\mathrm{OS,glass}} = 0.20 \times 10^{-22}\ \mathrm{Js\,nm^{-2}}$. The unique properties determined for zwitterionic polymer brushes seem to provide the physical explanation of their previously reported blood repulsion capability [259].

7.1.6 Summary

The effective interfacial potential was probed with cell sized latex beads and approximated as harmonic. The corresponding spring constants increased according to the increase in monovalent cation concentration always following the sequence: $V''_{\mathrm{KCl}} < V''_{\mathrm{NaCl}} \ll V''_{\mathrm{N(CH_3)_4Cl}}$, suggesting the dependency on the Hofmeister series. For $CaCl_2$ the opposite behavior was observed, indicating a unique influence of divalent ions on zwitterionic brushes. The inter chain interactions were examined using free sulfobetaine solutions, resulting in sharply confined potentials with increasing spring constants for higher concentrations. In clear contrast to all other ions, the friction coefficient significantly increased with increasing free sulfobetaine concentrations, indicating an intercalation effect. The excellent anti fouling capability was demonstrated using osmotic spherocytes. Indeed, the effective interfacial potential was found to be shallow with a very low hydrodynamic friction exerted on the cells. Further detailed studies of the ion distribution and water structure within the brush layers could help to understand and improve the unique properties of zwitterionic polymer brushes.

8 Appendix II

8.1 Abbreviations

AFM	Atomic force microscopy
BSA	Bovine serum albumin
CD36	Cluster of differentiation 36
CIDR	Cysteine rich domain region
CO_2	Carbon dioxide
CSA	Chondroitin sulfate A
DBL	Duffy binding like
DOGS-NTA	1,2-dioleoyl-sn-glycero-3-[(N-(5-amino-1-carboxypentyl)iminodiacetic acid)succinyl] (nickel salt)
DOPC	1,2-dioleoyl-sn-glycero-3-phosphocholine
EDTA	Ethylenediaminetetraacetic acid
FCR3	*Plasmodium falciparum* adapted Lab strain
FWHM	Full width at half maximum
Hb	Haemoglobin
HBS	HEPES buffered saline
HDMEC	Human dermal microvascular endothelial cells
HEPES	2-[4-(2-hydroxyethyl)piperazin-1-yl] ethanesulfonic acid
HUVEC	Human umbilical vein endothelial cells
ICAM-1	Intercellular adhesion molecule 1
iRBC	Infected red blood cell
KAHRP	Knob Associated Histidine Rich Protein
MACS	Magnetic activated cell sorter
MSA	Mean square amplitude
NA	Numerical Aperture
NPP	New permeation pathways
O_2	Oxygen
OS	Osmotic spherocytes
P.	Plasmodium
PBS	Phosphate buffered saline
PfEMP1	*Plasmodium falciparum* erythrocyte membrane protein 1
RBC	Red blood cell
rpm	Revolutions per minute
RPMI	Roswell Park Memorial Institute
ROS	Reactive oxygen species
RT	Room temperature
SD	Standard deviation
SUV	Small unilammelar vesicles

SXRF	Scanning X-ray fluorescence
uRBC	Uninfected red blood cell
WHO	World Health Organization

8.2 Measuring units and symbols

%	Percent
°C	Degree Celsius
A	Area
a.u.	Arbitrary units
γ	Harmonic confinement
E	Electric field
η	Viscosity, Fluorescence yield
g	Gramm
h	Hours, height
H_A	Hamaker constant
I	Intensity
k	Kilo
κ	Bending rigidity, prolongation factor
λ	Wavelength
L, l	Liter
M	Molar
m	Meter or milli
σ	Membrane tension, repeller density, cross section
P	Pressure
r	Distance, Pearson correlation coefficient
t	Transmission coefficient
τ	Shear stress, characteristic decay time
ω	Frequency

8.3 Supporting information

8.3.1 SI Chapter (1.2)-Introduction

Supporting Table 8-1 | Classification as severe form of malaria if patients display one or more symptoms [264, 265].

symptoms	medical proof
cerebral malaria	coma and seizures
respiratory distress	plasma bicarbonate < 15 mmol/l
pulmonary edema	radiologically confirmed
jaundice	plasma bilirubin > 3 mg/dl
severe anemia	haemoglobin < 5 g/dl
hypoglycemia	blood glucose < 40 mg/dl
renal failure	plasma creatinine > 3 mg/dl
hyperparasitaemia	parasitaemia (> 10%)

8.3.2 SI Chapter (3.1)-Functionalized solid-supported lipid bilayers

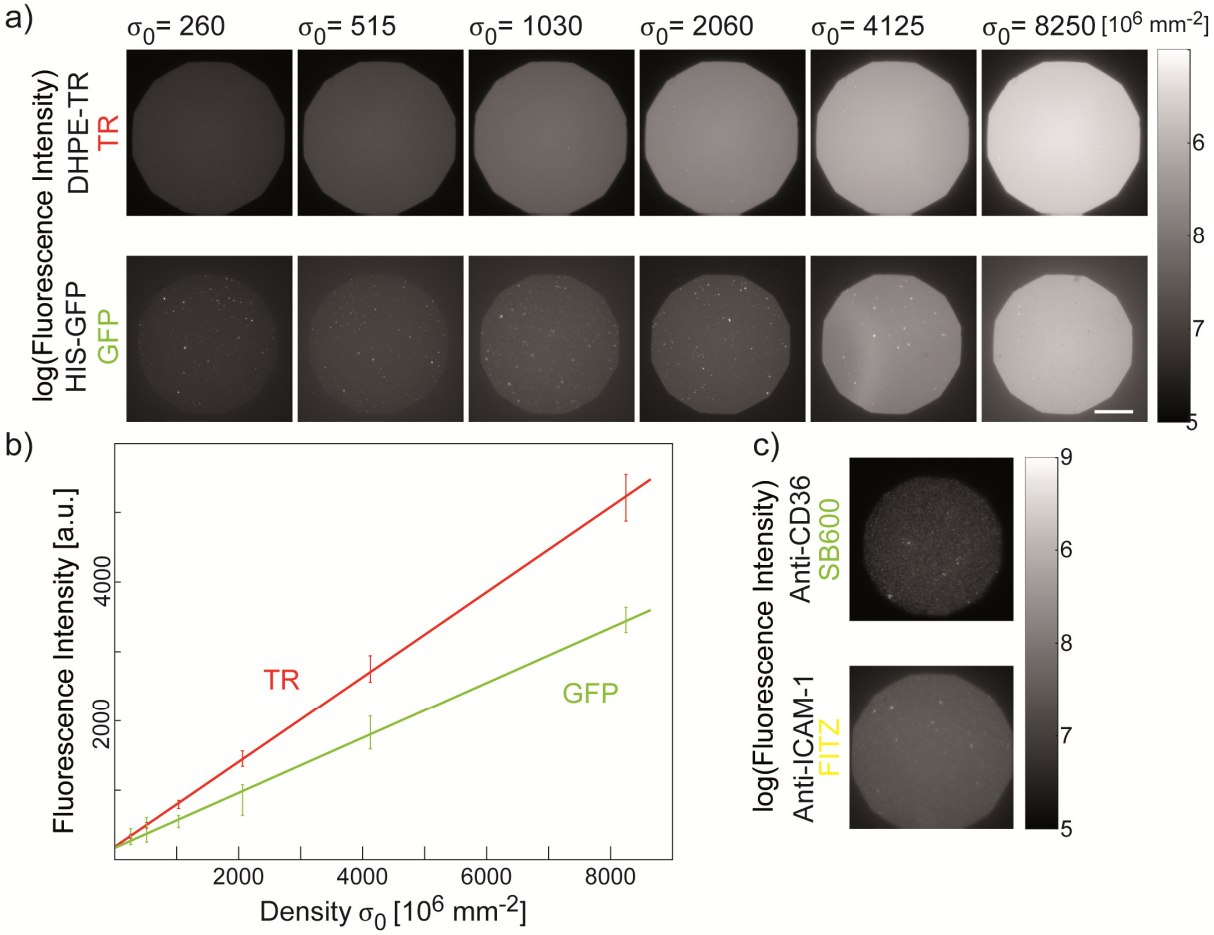

Supporting Figure 8.1 | Membrane quality control. (a) Fluorescence maps of solid-supported membranes incooperating different densities $\sigma_0$of Texas Red™ 1,2-Dihexadecanoyl-sn-Glycero-3-Phosphoethanolamine (DHPE-TR) instead of DOGS-NTA (Ni^{2+}) (upper panel). Fluorescence maps of solid-supported membranes incooperating different densities σ_0 of DOGS-NTA (Ni^{2+}) after the incubation with histidine tagged GFP (HIS-GFP). (b) The corresponding fluorescence intensity as a function of density σ_0 of DHPE-TR and HIS-GFP does exhibit a clear linear trend. (c) Solid-supported membrane with of DOGS-NTA (Ni^{2+}) at $\sigma_0 = 1030$ [10^6 mm^{-2}] functionalized with CD36 (upper panel) or ICAM-1 (lower panel). Fluorescence maps after the incubation with 5 µg/ml Anti-CD36 (super bright 600, SB600) and Anit-ICAM-1 (Fluorescein isothiocyanate, FITC). All presented maps show highly uniform fluorescence yield. Scale bar, 50 µm.

8.3.3 SI Chapter (3.2)-Pressure wave based evaluation of cell adhesion strength

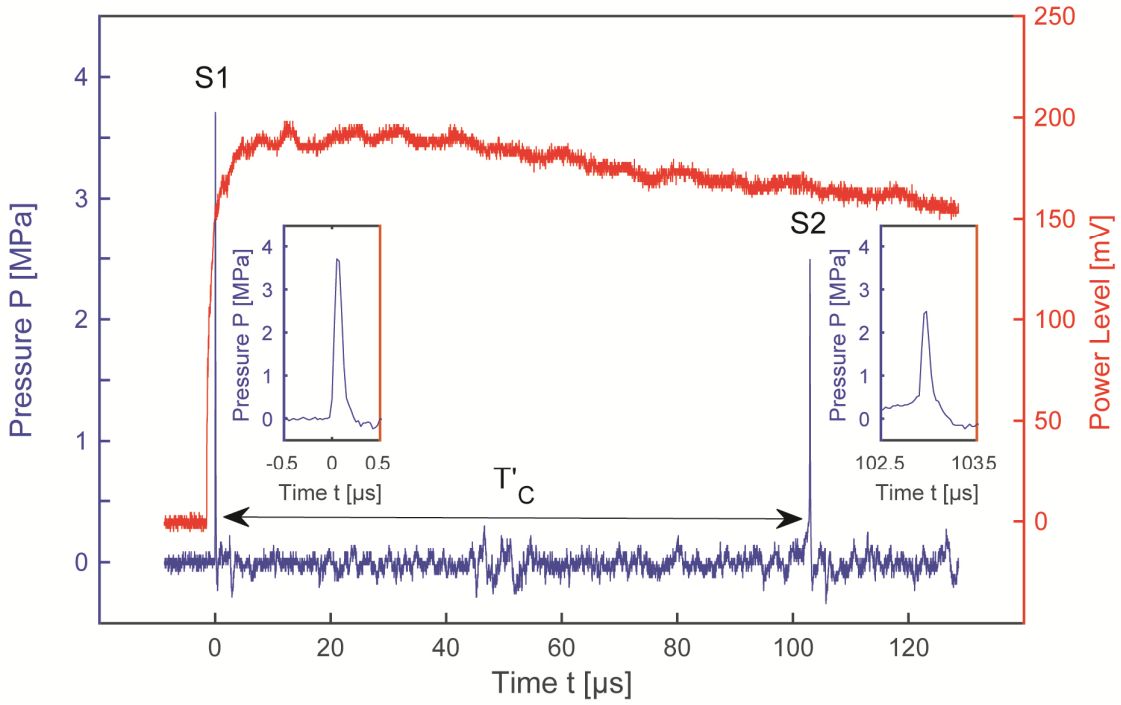

Supporting Figure 8.2 | Oscillogram of the pressure and power level recorded during a calibration session. Single laser pulses were registered by a power meter (red). The piezo hydrophone at a focus distance of 2 mm registers a peak caused by the creation of a cavitation bubble (blue, S1) followed by a second peak (blue, S2) due to the collapse of the cavitation bubble.

Following the modified Rayleigh equation, the maximum radius of the cavitation bubble in an infinite fluid reservoir can be estimated to[266]:

$$R_{Max} = \frac{T_C}{0.915}\sqrt{\frac{P_{stat} - P_V}{\rho}}, \qquad 8\text{-}1$$

where T_C denotes to the collapse time, ρ the fluid density (for aqueous medium one can assume $\rho = 1000\ \mathrm{kg/m^3}$), P_{stat} to the static pressure ($P_{stat} \approx 10^5\mathrm{Pa}$) and P_V to the vapor pressure inside the bubble ($P_V \approx 2300$ at RT)[267]. The substrates acts as a boundary prolonging the cavitation bubble collapse described by a prolongation factor κ:

$$\kappa = \frac{T'_C}{T_C} = 1 + 0.41\frac{1}{2\left(\frac{h}{R_{Max}}\right)}, \qquad 8\text{-}2$$

Where h denotes to the focus height above the substrate. Substituting equation (8-1) into equation (8-2) one derives:

$$R'_{Max} = \frac{T'_C}{0.915\kappa}\sqrt{\frac{p_{stat} - p_V}{\rho}}, \qquad 8\text{-}3$$

with the measured cavitation bubble decay time of $T'_C \approx 100$ µs, one can therefore calculate the maximum radius for the cavitation bubble to be $R'_{Max} \approx 980$ µm, assuming $h = 500$ µm.

8.3.4 SI Chapter (3.4)-Quantification of cell adhesion by micro interferometry

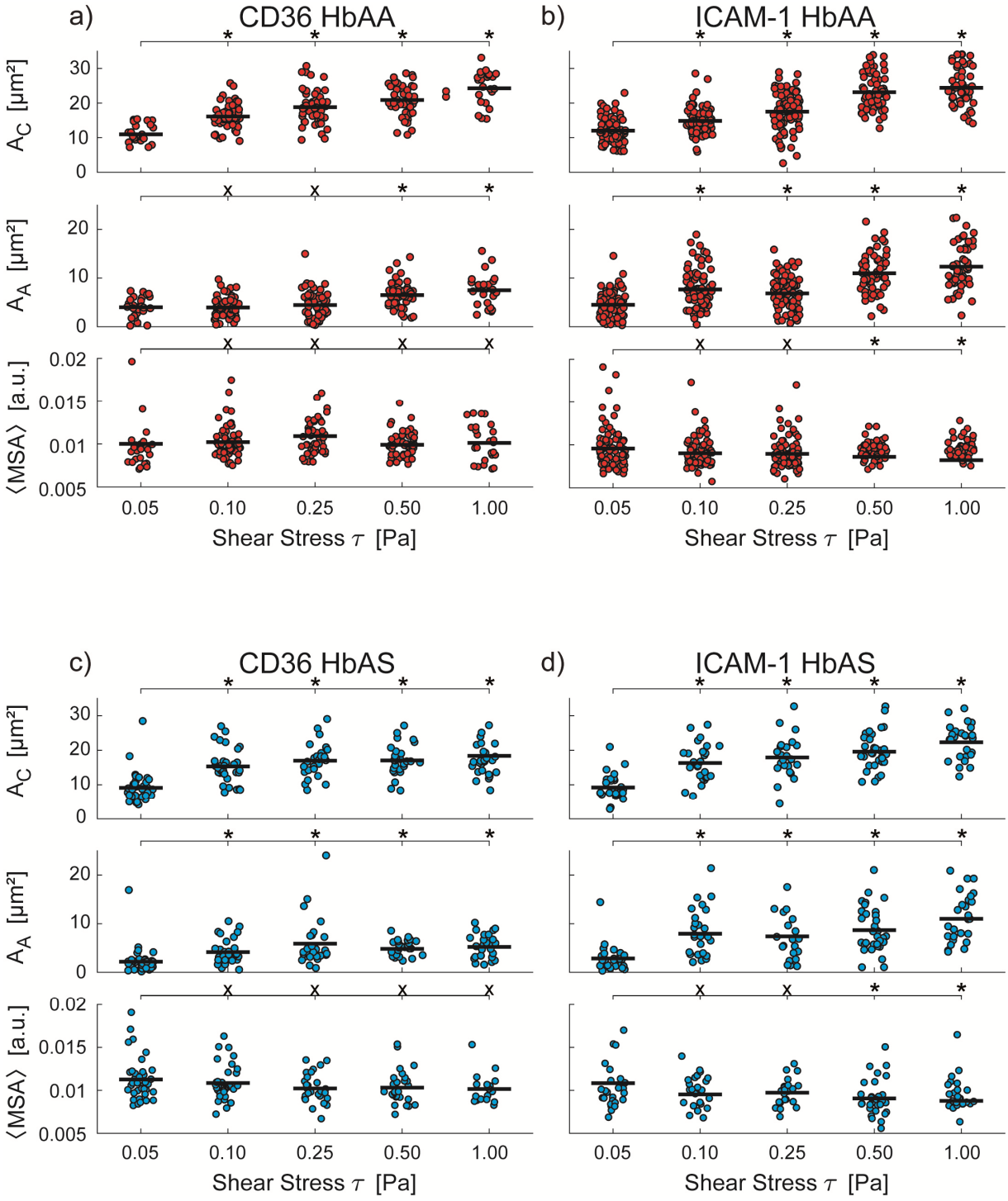

Supporting Figure 8.3 | Summary of data obtained by reflection interference contrast microscopy as presented in Chapter (3.4). (a)-(d) Contact area A_C, adhesion area A_A, and average mean square amplitude of intensity fluctuation $\langle MSA \rangle$ as determined by RICM. Data points represent single determinations for individual cells of at least three different donors. *, $p < 0.01$ according to Welch t-test.

8.3.5 SI Chapter (4.1)-*P. falciparum* induced changes to red blood cell mechanics

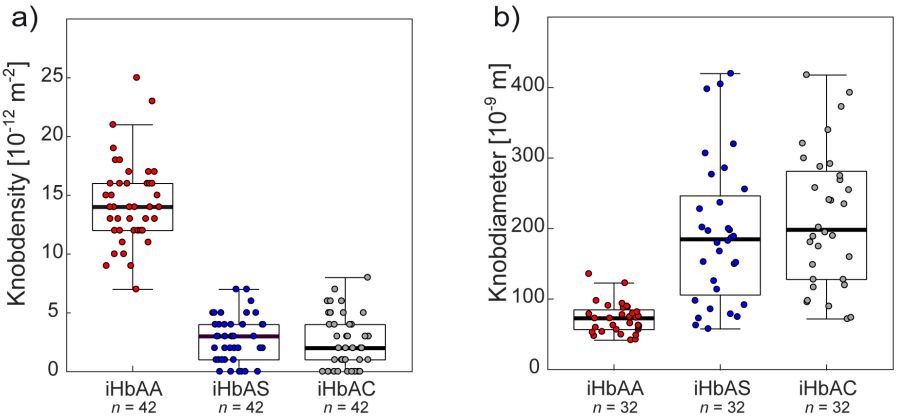

Supporting Figure 8.4 | Knob density and knob diameter of infected erythrocytes at the trophozoite stage obtained from SEM images. (SEM imaging and knob analysis was performed by Dr. Marek Cyrklaff, Center for Infectious Diseases, Heidelberg University Hospital)

Supporting Table 8-2 | Gaussian roughness (RMS) as a function of infectious stage. RMS determined from a Gaussian fit to histograms of the fluctuation amplitude $d = r_{rim}(\theta, T) - \langle r_{rim}(\theta, T) \rangle_{\theta,T}$ for each individual cell.

Stage of infection	Type	Gaussian roughness RMS [nm]
Uninfected	HbAA	90 ± 34 (42)
	HbAS	94 ± 33 (41)
	HbAC	103 ± 27 (36)
Ring	HbAA	137 ± 44 (30)
	HbAS	134 ± 49 (25)
	HbAC	136 ± 65 (25)
Trophozoite	HbAA	169 ± 47 (29)
	HbAS	164 ± 77 (39)
	HbAC	152 ± 55 (40)
knobless Trophozoite	HbAA	114 ± 31 (42)

8.3.6 SI Chapter (4.2)-Biochemical composition of infected red blood cells

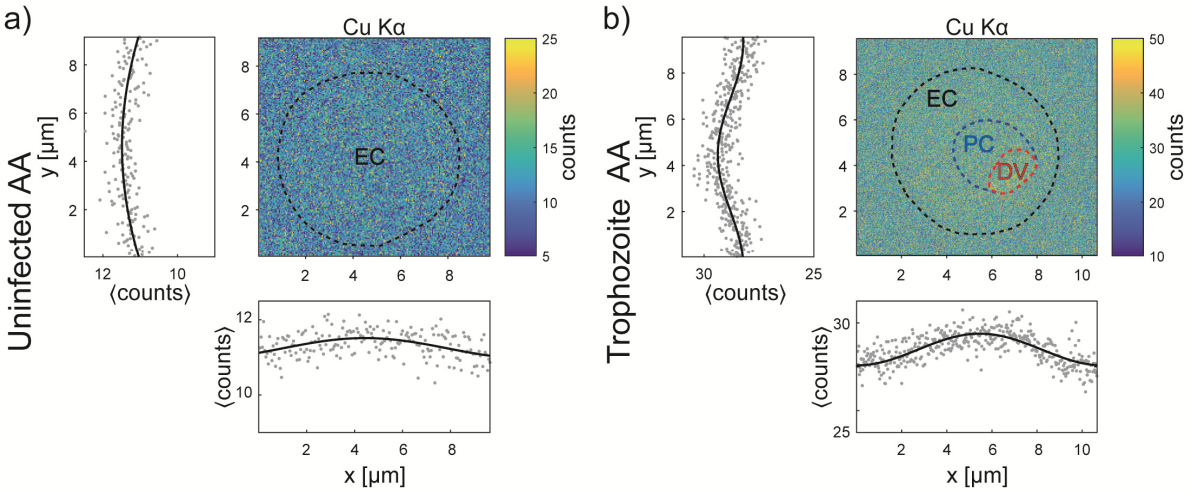

Supporting Figure 8.5 |Copper (Cu) distribution for (a) an uninfected wildtype erythrocyte and (b) an infected wildtype erythrocyte at the trophozoite stage (see Figure 4.13). Adjacent plots to the left and to the bottom denote to the average detector counts along the x and y axes, respectively. Black lines included to guide the eye.

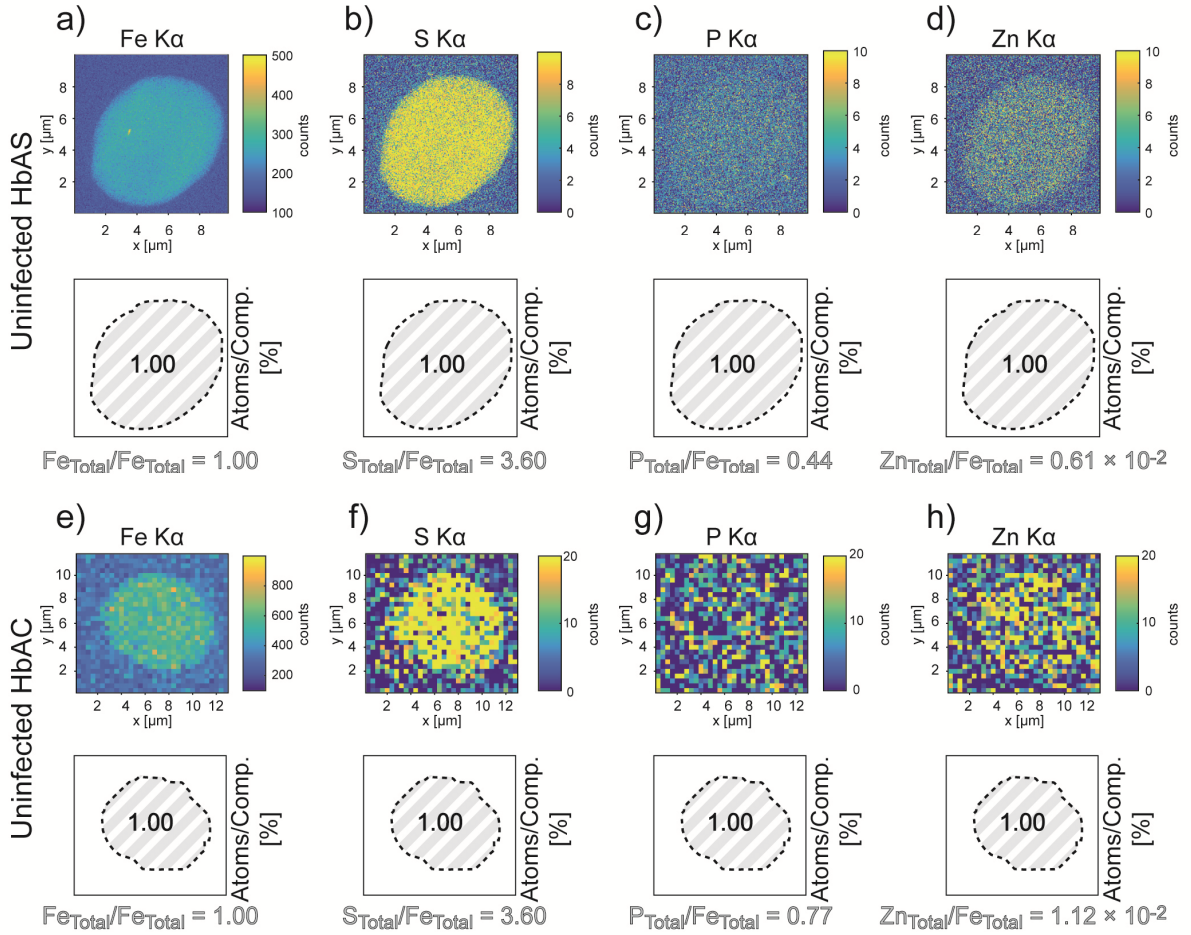

Supporting Figure 8.6 | Elemental maps of uninfected haemoglobinopathic erythrocytes. (a-d, upper panel, pixel size 50 nm) Element distributions for an uninfected HbAS erythrocyte. (e-h, upper panel, pixel size 400 nm) Element distributions for an uninfected HbAC erythrocyte. Lower panels depict the percentage ratios calculated for the erythrocyte cytosolic area (black).

9 Publications

The following publications resulted from this work:

Benjamin Fröhlich, Julia Jäger, Christine Lansche, Cecilia P. Sanchez, Marek Cyrklaff, Bernd Buchholz, Serge Theophile Soubeiga, Jacque Simpore, Hiroaki Ito, Ulrich S. Schwarz, Michael Lanzer, and Motomu Tanaka, **"Haemoglobin S and C affect biomechanical membrane properties of *P. falciparum* infected erythrocytes,"** Manuscript reviewed by Communications Biology (2019).

Christine Lansche, Anil K. Dasanna, Katharina Quadt, **Benjamin Fröhlich**, Dimitris Missirlis, Marilou Tétard, Benoit Gamain, Bernd Buchholz, Cecilia P. Sanchez, Motomu Tanaka, Ulrich S. Schwarz, and Michael Lanzer, **"The sickle cell trait affects contact dynamics and endothelial cell activation of *Plasmodium falciparum*-infected erythrocytes,"** Communications Biology 1, Article number: 211 (2018).

Federico Amadei, **Benjamin Fröhlich**, Wolfgang Stremmel, and Motomu Tanaka, **"Nonclassical Interactions of Phosphatidylcholine with Mucin Protect Intestinal Surfaces: A Microinterferometry Study,"** Langmuir 2018, 34, 14046−14057 (2018).

Viktoria Frank, Yuriy Chushkin, **Benjamin Fröhlich**, Wasim Abuillan, Harden Rieger, Alexandra S. Becker, Akihisa Yamamoto, Fernanda F. Rossetti, Stefan Kaufmann, Michael Lanzer, Federico Zontone and Motomu Tanaka, **"Lensless Tomographic Imaging of Near Surface Structures of Frozen Hydrated Malaria-Infected Human Erythrocytes by Coherent X-Ray Diffraction Microscopy,"** Scientific Reports 7, Article number: 14081 (2017).

Yuji Higaki, **Benjamin Fröhlich**, Akihisa Yamamoto, Ryo Murakami, Makoto Kaneko, Atsushi Takahara, and Motomu Tanaka, **"Ion-Specific Modulation of Interfacial Interaction Potentials between Solid Substrates and Cell-Sized Particles Mediated via Zwitterionic, Super-Hydrophilic Poly(sulfobetaine) Brushes,"** J. Phys. Chem 2017. B,121, 6, 1396-1404 (2017).

10 Bibliography

1. Tomaiuolo G. Biomechanical properties of red blood cells in health and disease towards microfluidics. *Biomicrofluidics* **8**, 051501 (2014).

2. Rodak BF, Fritsma GA, Keohane E. *Hematology-E-Book: Clinical Principles and Applications*. Elsevier Health Sciences (2013).

3. Fung Y, Skalak R. Biomechanics: mechanical properties of living tissues. (ed^(eds). American Society of Mechanical Engineers (1981).

4. Lux SE. Anatomy of the red cell membrane skeleton: unanswered questions. *Blood* **127**, 187-199 (2016).

5. Lux SE. Anatomy of the red cell membrane skeleton: unanswered questions. *Blood*, blood-2014-2012-512772 (2015).

6. Gokhin DS, Fowler VM. Feisty filaments: actin dynamics in the red blood cell membrane skeleton. *Current opinion in hematology* **23**, 206 (2016).

7. An X, Lecomte MC, Chasis JA, Mohandas N, Gratzer W. Shear-response of the spectrin dimer-tetramer equilibrium in the red blood cell membrane. *Journal of Biological Chemistry* **277**, 31796-31800 (2002).

8. Swihart A, Mikrut J, Ketterson J, Macdonald R. Atomic force microscopy of the erythrocyte membrane skeleton. *Journal of microscopy* **204**, 212-225 (2001).

9. Nans A, Mohandas N, Stokes DL. Native ultrastructure of the red cell cytoskeleton by cryo-electron tomography. *Biophysical journal* **101**, 2341-2350 (2011).

10. Shotton DM, Burke BE, Branton D. The molecular structure of human erythrocyte spectrin: biophysical and electron microscopic studies. *Journal of molecular biology* **131**, 303-329 (1979).

11. Bennett V, Baines AJ. Spectrin and ankyrin-based pathways: metazoan inventions for integrating cells into tissues. *Physiological reviews* **81**, 1353-1392 (2001).

12. Eylar EH, Madoff MA, Brody O, Oncley J. The contribution of sialic acid to the surface charge of the erythrocyte. *Journal of Biological Chemistry* **237**, 1992-2000 (1962).

13. Werre J, Willekens F, Bosch F, Bosman G. The red cell revisited--matters of life and death. *Cellular and molecular biology (Noisy-le-Grand, France)* **50**, 139-145 (2004).

14. Bosman GJCGM, Werre J, Willekens F, Novotný V. Erythrocyte ageing in vivo and in vitro: structural aspects and implications for transfusion. *Transfusion Medicine* **18**, 335-347 (2008).

15. Miller LH, Baruch DI, Marsh K, Doumbo OK. The pathogenic basis of malaria. *Nature* **415**, 673-679 (2002).

16. Organization WH. *World malaria report 2015*. World Health Organization (2016).

17. Maier AG, Cooke BM, Cowman AF, Tilley L. Malaria parasite proteins that remodel the host erythrocyte. *Nature Reviews Microbiology* **7**, 341 (2009).

18. Cowman AF, Healer J, Marapana D, Marsh K. Malaria: biology and disease. *Cell* **167**, 610-624 (2016).

19. Bruce M, Alano P, Duthie S, Carter R. Commitment of the malaria parasite Plasmodium falciparum to sexual and asexual development. *Parasitology* **100**, 191-200 (1990).

20. Storm J, Craig AG. Pathogenesis of cerebral malaria—inflammation and cytoadherence. *Frontiers in cellular and infection microbiology* **4**, (2014).

21. Bannister L, Hopkins J, Fowler R, Krishna S, Mitchell G. A brief illustrated guide to the ultrastructure of Plasmodium falciparum asexual blood stages. *Parasitology today* **16**, 427-433 (2000).

22. Marsh K*, et al.* Indicators of life-threatening malaria in African children. *New England journal of medicine* **332**, 1399-1404 (1995).

23. Dondorp AM*, et al.* Direct in vivo assessment of microcirculatory dysfunction in severe falciparum malaria. *The Journal of infectious diseases* **197**, 79-84 (2008).

24. Miller LH, Ackerman HC, Su X-z, Wellems TE. Malaria biology and disease pathogenesis: insights for new treatments. *Nature medicine* **19**, 156-167 (2013).

25. Molyneux M, Taylor T, Wirima J, Borgsteinj A. Clinical features and prognostic indicators in paediatric cerebral malaria: a study of 131 comatose Malawian children. *QJM: An International Journal of Medicine* **71**, 441-459 (1989).

26. Waller D*, et al.* Clinical features and outcome of severe malaria in Gambian children. *Clinical infectious diseases* **21**, 577-587 (1995).

27. MacPherson G, Warrell M, White N, Looareesuwan S, Warrell D. Human cerebral malaria. A quantitative ultrastructural analysis of parasitized erythrocyte sequestration. *The American journal of pathology* **119**, 385 (1985).

28. Jorde LB, Carey JC, Bamshad MJ. *Medical genetics*, Fifth edition. edn. Elsevier (2016).

29. Liu J, Istvan ES, Gluzman IY, Gross J, Goldberg DE. Plasmodium falciparum ensures its amino acid supply with multiple acquisition pathways and redundant proteolytic enzyme systems. *Proceedings of the National Academy of Sciences* **103**, 8840-8845 (2006).

30. Kumar S, Bandyopadhyay U. Free heme toxicity and its detoxification systems in human. *Toxicology letters* **157**, 175-188 (2005).

31. Krugliak M, Zhang J, Ginsburg H. Intraerythrocytic Plasmodium falciparum utilizes only a fraction of the amino acids derived from the digestion of host cell cytosol for the biosynthesis of its proteins. *Molecular and biochemical parasitology* **119**, 249-256 (2002).

32. Desai SA, Krogstad DJ, McCleskey EW. A nutrient-permeable channel on the intraerythrocytic malaria parasite. *Nature* **362**, 643 (1993).

33. Kirk K, Tilley L, Ginsburg H. Transport and trafficking in the malaria-infected erythrocyte. *Parasitol Today* **15**, 355-357 (1999).

34. Waldecker M*, et al.* Differential time-dependent volumetric and surface area changes and delayed induction of new permeation pathways in P. falciparum-infected hemoglobinopathic erythrocytes. *Cell Microbiol* **19**, (2017).

35. Lew VL, Tiffert T, Ginsburg H. Excess hemoglobin digestion and the osmotic stability ofPlasmodium falciparum–infected red blood cells. *Blood* **101**, 4189-4194 (2003).

36. Mebius RE, Kraal G. Structure and function of the spleen. *Nature Reviews Immunology* **5**, 606 (2005).

37. Lanzer M, Wickert H, Krohne G, Vincensini L, Braun Breton C. Maurer's clefts: A novel multi-functional organelle in the cytoplasm of Plasmodium falciparum-infected erythrocytes. *Int J Parasitol* **36**, 23-36 (2006).

38. Cyrklaff M, Sanchez CP, Frischknecht F, Lanzer M. Host actin remodeling and protection from malaria by hemoglobinopathies. *Trends in parasitology* **28**, 479-485 (2012).

39. Crabb BS*, et al.* Targeted gene disruption shows that knobs enable malaria-infected red cells to cytoadhere under physiological shear stress. *Cell* **89**, 287-296. (1997).

40. Rug M, Prescott SW, Fernandez KM, Cooke BM, Cowman AF. The role of KAHRP domains in knob formation and cytoadherence of P falciparum-infected human erythrocytes. *Blood* **108**, 370-378 (2006).

41. Pologe LG, Pavlovec A, Shio H, Ravetch JV. Primary structure and subcellular localization of the knob-associated histidine-rich protein of Plasmodium falciparum. *Proc Natl Acad Sci U S A* **84**, 7139-7143. (1987).

42. Weng H*, et al.* Interaction of Plasmodium falciparum knob-associated histidine-rich protein (KAHRP) with erythrocyte ankyrin R is required for its attachment to the erythrocyte membrane. *Biochim Biophys Acta* **1838**, 185-192 (2014).

43. Cooke BM, Glenister FK, Mohandas N, Coppel RL. Assignment of functional roles to parasite proteins in malaria-infected red blood cells by competitive flow-based adhesion assay. *British journal of haematology* **117**, 203-211 (2002).

44. Quadt KA*, et al.* The density of knobs on Plasmodium falciparum-infected erythrocytes depends on developmental age and varies among isolates. *PLoS One* **7**, e45658 (2012).

45. Subramani R*, et al.* Plasmodium falciparum-infected erythrocyte knob density is linked to the PfEMP1 variant expressed. *MBio* **6**, e01456-01415 (2015).

46. Lansche C. Protection against severe malaria by hemoglobin S and C: A quantitative understanding of the cytoadhesion behavior of Plasmodium falciparum infected erythrocytes. (ed^(eds). Heidelberg (2018).

47. Helms G, Dasanna AK, Schwarz US, Lanzer M. Modeling cytoadhesion of Plasmodium falciparum-infected erythrocytes and leukocytes-common principles and distinctive features. *FEBS Lett* **590**, 1955-1971 (2016).

48. Smith JD, Gamain B, Baruch DI, Kyes S. Decoding the language of var genes and Plasmodium falciparum sequestration. *Trends in parasitology* **17**, 538-545 (2001).

49. Horrocks P*, et al.* PfEMP1 expression is reduced on the surface of knobless Plasmodium falciparum infected erythrocytes. *Journal of cell science* **118**, 2507-2518 (2005).

50. Flick K, Chen Q. var genes, PfEMP1 and the human host. *Mol Biochem Parasitol* **134**, 3-9 (2004).

51. Gardner MJ*, et al.* Genome sequence of the human malaria parasite Plasmodium falciparum. *Nature* **419**, 498 (2002).

52. Su XZ*, et al.* The large diverse gene family var encodes proteins involved in cytoadherence and antigenic variation of Plasmodium falciparum-infected erythrocytes. *Cell* **82**, 89-100. (1995).

53. Pasternak ND, Dzikowski R. PfEMP1: an antigen that plays a key role in the pathogenicity and immune evasion of the malaria parasite Plasmodium falciparum. *Int J Biochem Cell Biol* **41**, 1463-1466 (2009).

54. Dzikowski R, Templeton TJ, Deitsch K. Variant antigen gene expression in malaria. *Cell Microbiol* **8**, 1371-1381 (2006).

55. Ockenhouse CF*, et al.* Molecular basis of sequestration in severe and uncomplicated Plasmodium falciparum malaria: differential adhesion of infected erythrocytes to CD36 and ICAM-l. *Journal of Infectious Diseases* **164**, 163-169 (1991).

56. Ho M, Singh B, Looareesuwan S, Davis T, Bunnag D, White N. Clinical correlates of in vitro Plasmodium falciparum cytoadherence. *Infection and immunity* **59**, 873-878 (1991).

57. Ochola LB*, et al.* Specific receptor usage in Plasmodium falciparum cytoadherence is associated with disease outcome. *PloS one* **6**, e14741 (2011).

58. Silamut K*, et al.* A quantitative analysis of the microvascular sequestration of malaria parasites in the human brain. *The American journal of pathology* **155**, 395-410 (1999).

59. Silverstein RL, Febbraio M. CD36, a scavenger receptor involved in immunity, metabolism, angiogenesis, and behavior. *Sci Signal* **2**, re3-re3 (2009).

60. Newbold C*, et al.* Receptor-specific adhesion and clinical disease in Plasmodium falciparum. *The American journal of tropical medicine and hygiene* **57**, 389-398 (1997).

61. Pain A*, et al.* Platelet-mediated clumping of Plasmodium falciparum-infected erythrocytes is a common adhesive phenotype and is associated with severe malaria. *Proceedings of the National Academy of Sciences* **98**, 1805-1810 (2001).

62. Hsieh F-L, Turner L, Bolla JR, Robinson CV, Lavstsen T, Higgins MK. The structural basis for CD36 binding by the malaria parasite. *Nature communications* **7**, 12837 (2016).

63. Preedy VR. *Adhesion molecules*. Science Publishers ;

Distributed by CRC Press (2010).

64. Rothlein R, Dustin ML, Marlin SD, Springer T. A human intercellular adhesion molecule (ICAM-1) distinct from LFA-1. *The Journal of Immunology* **137**, 1270-1274 (1986).

65. Silamut K*, et al.* A quantitative analysis of the microvascular sequestration of malaria parasites in the human brain. *Am J Pathol* **155**, 395-410 (1999).

66. Lennartz F*, et al.* Structure-guided identification of a family of dual receptor-binding PfEMP1 that is associated with cerebral malaria. *Cell host & microbe* **21**, 403-414 (2017).

67. Thom CS, Dickson CF, Gell DA, Weiss MJ. Hemoglobin variants: biochemical properties and clinical correlates. *Cold Spring Harbor perspectives in medicine* **3**, a011858 (2013).

68. Piel FB*, et al.* Global distribution of the sickle cell gene and geographical confirmation of the malaria hypothesis. *Nat Commun* **1**, 104 (2010).

69. Piel FB*, et al.* Global distribution of the sickle cell gene and geographical confirmation of the malaria hypothesis. *Nature communications* **1**, 104 (2010).

70. Wu T, Wang XS, Cohen B, Ge H. Molecular modeling of normal and sickle hemoglobins. *International Journal for Multiscale Computational Engineering* **8**, (2010).

71. Naik P. *Essentials of Biochemistry (for Medical Students)*. Jaypee Brothers,Medical Publishers Pvt. Limited (2011).

72. Roberts DJ, Williams TN. Haemoglobinopathies and resistance to malaria. *Redox Report* **8**, 304-310 (2003).

73. Cyrklaff M*, et al.* Oxidative insult can induce malaria-protective trait of sickle and fetal erythrocytes. *Nat Commun* **7**, 13401 (2016).

74. Hebbel RP. Beyond hemoglobin polymerization: the red blood cell membrane and sickle disease pathophysiology. *Blood* **77**, 214-237 (1991).

75. Chaves MAF, Leonart MSS, do Nascimento AJ. Oxidative process in erythrocytes of individuals with hemoglobin S. *Hematology* **13**, 187-192 (2008).

76. Jarolim P, Lahav M, Liu SC, Palek J. Effect of hemoglobin oxidation products on the stability of red cell membrane skeletons and the associations of skeletal proteins: correlation with a release of hemin. *Blood* **76**, 2125-2131 (1990).

77. Farah ME, Sirotkin V, Haarer B, Kakhniashvili D, Amberg DC. Diverse protective roles of the actin cytoskeleton during oxidative stress. *Cytoskeleton (Hoboken)* **68**, 340-354 (2011).

78. Fairhurst RM, Bess CD, Krause MA. Abnormal PfEMP1/knob display on Plasmodium falciparum-infected erythrocytes containing hemoglobin variants: fresh insights into malaria pathogenesis and protection. *Microbes Infect* **14**, 851-862 (2012).

79. Cholera R*, et al.* Impaired cytoadherence of Plasmodium falciparum-infected erythrocytes containing sickle hemoglobin. *Proc Natl Acad Sci U S A* **105**, 991-996 (2008).

80. Aidoo M*, et al.* Protective effects of the sickle cell gene against malaria morbidity and mortality. *The Lancet* **359**, 1311-1312 (2002).

81. Agarwal A*, et al.* Hemoglobin C associated with protection from severe malaria in the Dogon of Mali, a West African population with a low prevalence of hemoglobin S. *Blood* **96**, 2358-2363 (2000).

82. Tanaka M, Sackmann E. Polymer-supported membranes as models of the cell surface. *Nature* **437**, 656-663 (2005).

83. Burk AS*, et al.* Quantifying adhesion mechanisms and dynamics of human hematopoietic stem and progenitor cells. *Scientific reports* **5**, 9370 (2015).

84. Rieger H*, et al.* Cytoadhesion of Plasmodium falciparum-infected erythrocytes to chondroitin-4-sulfate is cooperative and shear enhanced. *Blood* **125**, 383-391 (2015).

85. Sackmann E, Tanaka M. Supported membranes on soft polymer cushions: fabrication, characterization and applications. *Trends in biotechnology* **18**, 58-64 (2000).

86. Singer SJ, Nicolson GL. The fluid mosaic model of the structure of cell membranes. *Science* **175**, 720-731 (1972).

87. Sackmann E, Smith A-S. Physics of cell adhesion: some lessons from cell-mimetic systems. *Soft matter* **10**, 1644-1659 (2014).

88. Shelby JP, White J, Ganesan K, Rathod PK, Chiu DT. A microfluidic model for single-cell capillary obstruction by Plasmodium falciparum-infected erythrocytes. *Proceedings of the National Academy of Sciences* **100**, 14618-14622 (2003).

89. Raventos-Suarez C, Kaul DK, Macaluso F, Nagel RL. Membrane knobs are required for the microcirculatory obstruction induced by Plasmodium falciparum-infected erythrocytes. *Proceedings of the National Academy of Sciences* **82**, 3829-3833 (1985).

90. Diakité SA*, et al.* Stage-dependent fate of Plasmodium falciparum-infected red blood cells in the spleen and sickle-cell trait-related protection against malaria. *Malaria journal* **15**, 482 (2016).

91. Brochard F, Lennon J. Frequency spectrum of the flicker phenomenon in erythrocytes. *Journal de Physique* **36**, 1035-1047 (1975).

92. Kilian N*, et al.* Hemoglobin S and C affect protein export in Plasmodium falciparum-infected erythrocytes. *Biology open* **4**, 400-410 (2015).

93. De Samber B*, et al.* Nanoscopic X-ray fluorescence imaging and quantification of intracellular key-elements in cryofrozen Friedreich's ataxia fibroblasts. *PloS one* **13**, e0190495 (2018).

94. De Samber B*, et al.* Hard X-ray nanoprobe investigations of the subtissue metal distributions within Daphnia magna. *Analytical and bioanalytical chemistry* **405**, 6061-6068 (2013).

95. Trager W, Jensen JB. Human malaria parasites in continuous culture. *Journal of Parasitology* **91**, 484-486 (2005).

96. Mata-Cantero L, Lafuente MJ, Sanz L, Rodriguez MS. Magnetic isolation of Plasmodium falciparum schizonts iRBCs to generate a high parasitaemia and synchronized in vitro culture. *Malaria journal* **13**, 112 (2014).

97. Ljungström I, Moll K, Perlmann H, Scherf A, Wahlgren M. *Methods in malaria research*. Citeseer (2008).

98. Claessens A, Rowe JA. Selection of Plasmodium falciparum parasites for cytoadhesion to human brain endothelial cells. *Journal of visualized experiments: JoVE*, (2012).

99. Bell GI, Dembo M, Bongrand P. Cell adhesion. Competition between nonspecific repulsion and specific bonding. *Biophysical journal* **45**, 1051-1064 (1984).

100. Bruinsma R, Behrisch A, Sackmann E. Adhesive switching of membranes: experiment and theory. *Physical Review E* **61**, 4253 (2000).

101. Schmidt D, Bihr T, Seifert U, Smith A-S. Coexistence of dilute and densely packed domains of ligand-receptor bonds in membrane adhesion. *EPL (Europhysics Letters)* **99**, 38003 (2012).

102. Guttenberg Z, Lorz B, Sackmann E, Boulbitch A. First-order transition between adhesion states in a system mimicking cell-tissue interaction. *EPL (Europhysics Letters)* **54**, 826 (2001).

103. Weikl TR, Andelman D, Komura S, Lipowsky R. Adhesion of membranes with competing specific and generic interactions. *The European Physical Journal E* **8**, 59-66 (2002).

104. Cooke BM, Berendt AR, Craig AG, MacGregor J, Newbold CI, Nash GB. Rolling and stationary cytoadhesion of red blood cells parasitized by Plasmodium falciparum: separate roles for ICAM-1, CD36 and thrombospondin. *British journal of haematology* **87**, 162-170 (1994).

105. Johnson JK, Swerlick RA, Grady KK, Millet P, Wick TM. Cytoadherence of Plasmodium falciparum-infected erythrocytes to microvascular endothelium is regulatable by cytokines and phorbol ester. *Journal of Infectious Diseases* **167**, 698-703 (1993).

106. Fried M, Duffy PE. Adherence of Plasmodium falciparum to chondroitin sulfate A in the human placenta. *Science* **272**, 1502-1504 (1996).

107. Kern W. Handbook of semiconductor wafer cleaning technology. *New Jersey: Noyes Publication*, 111-196 (1993).

108. Sackmann E. Supported membranes: scientific and practical applications. *Science* **271**, 43-48 (1996).

109. Körner A*, et al.* Cell differentiation of pluripotent tissue sheets immobilized on supported membranes displaying cadherin-11. *PLoS One* **8**, e54749 (2013).

110. Lipowsky R, Sackmann E. *Structure and dynamics of membranes: I. from cells to vesicles/II. generic and specific interactions*. Elsevier (1995).

111. Abuillan W, Vorobiev A, Hartel A, Jones NG, Engstler M, Tanaka M. Quantitative determination of the lateral density and intermolecular correlation between proteins anchored on the membrane surfaces using grazing incidence small-angle X-ray scattering and grazing incidence X-ray fluorescence. *The Journal of Chemical Physics* **137**, 204907 (2012).

112. Shao JY, Hochmuth RM. Micropipette suction for measuring piconewton forces of adhesion and tether formation from neutrophil membranes. *Biophysical journal* **71**, 2892-2901 (1996).

113. Hochmuth RM. Micropipette aspiration of living cells. *Journal of biomechanics* **33**, 15-22 (2000).

114. Dao M, Lim CT, Suresh S. Mechanics of the human red blood cell deformed by optical tweezers. *Journal of the Mechanics and Physics of Solids* **51**, 2259-2280 (2003).

115. Mills J*, et al.* Effect of plasmodial RESA protein on deformability of human red blood cells harboring Plasmodium falciparum. *Proceedings of the National Academy of Sciences* **104**, 9213-9217 (2007).

116. Neuman KC, Nagy A. Single-molecule force spectroscopy: optical tweezers, magnetic tweezers and atomic force microscopy. *Nature methods* **5**, 491 (2008).

117. Walter N, Selhuber C, Kessler H, Spatz JP. Cellular unbinding forces of initial adhesion processes on nanopatterned surfaces probed with magnetic tweezers. *Nano letters* **6**, 398-402 (2006).

118. Binnig G, Quate CF, Gerber C. Atomic Force Microscope. *Physical Review Letters* **56**, 930-933 (1986).

119. Benoit M, Gabriel D, Gerisch G, Gaub HE. Discrete interactions in cell adhesion measured by single-molecule force spectroscopy. *Nature cell biology* **2**, 313 (2000).

120. Puech P-H, Poole K, Knebel D, Muller DJ. A new technical approach to quantify cell–cell adhesion forces by AFM. *Ultramicroscopy* **106**, 637-644 (2006).

121. Baaijens FP, Trickey WR, Laursen TA, Guilak F. Large deformation finite element analysis of micropipette aspiration to determine the mechanical properties of the chondrocyte. *Annals of biomedical engineering* **33**, 494-501 (2005).

122. Maksym GN*, et al.* Mechanical properties of cultured human airway smooth muscle cells from 0.05 to 0.4 Hz. *Journal of Applied Physiology* **89**, 1619-1632 (2000).

123. Giessibl FJ. AFM's path to atomic resolution. *Materials Today* **8**, 32-41 (2005).

124. Yoshikawa HY*, et al.* Quantitative evaluation of mechanosensing of cells on dynamically tunable hydrogels. *Journal of the American Chemical Society* **133**, 1367-1374 (2011).

125. Lauterborn W, Vogel A. Shock wave emission by laser generated bubbles. In: *Bubble dynamics and shock waves* (ed^(eds). Springer (2013).

126. Vogel A, Noack J, Hüttman G, Paltauf G. Mechanisms of femtosecond laser nanosurgery of cells and tissues. *Applied Physics B* **81**, 1015-1047 (2005).

127. Barcroft J, Hill A. The nature of oxyhaemoglobin, with a note on its molecular weight. *The Journal of physiology* **39**, 411-428 (1910).

128. Berendt AR*, et al.* Molecular mechanisms of sequestration in malaria. *Parasitology* **108 Suppl**, S19-28 (1994).

129. Davis SP, Amrein M, Gillrie MR, Lee K, Muruve DA, Ho M. Plasmodium falciparum-induced CD36 clustering rapidly strengthens cytoadherence via p130CAS-mediated actin cytoskeletal rearrangement. *The FASEB Journal* **26**, 1119-1130 (2012).

130. Fairhurst RM*, et al.* Abnormal display of PfEMP-1 on erythrocytes carrying haemoglobin C may protect against malaria. *Nature* **435**, 1117-1121 (2005).

131. Aikawa M*, et al.* Membrane knobs of unfixedplasmodium falciparumInfected erythrocytes: New findings as revealed by atomic force microscopy and surface potential spectroscopy. *Experimental parasitology* **84**, 339-343 (1996).

132. Huang YX*, et al.* Human red blood cell aging: correlative changes in surface charge and cell properties. *Journal of cellular and molecular medicine* **15**, 2634-2642 (2011).

133. Hempel C, Wang CW, Kurtzhals JAL, Staalsø T. Binding of Plasmodium falciparum to CD36 can be shielded by the glycocalyx. *Malaria journal* **16**, 193 (2017).

134. Lansche C*, et al.* The sickle cell trait affects contact dynamics and endothelial cell activation in Plasmodium falciparum-infected erythrocytes. *Communications biology* **1**, 211 (2018).

135. Viebig NK, Wulbrand U, Forster R, Andrews KT, Lanzer M, Knolle PA. Direct activation of human endothelial cells by Plasmodium falciparum-infected erythrocytes. *Infect Immun* **73**, 3271-3277 (2005).

136. Bell GI. Models for the specific adhesion of cells to cells. *Science* **200**, 618-627 (1978).

137. Evans E, Ritchie K. Dynamic strength of molecular adhesion bonds. *Biophysical journal* **72**, 1541-1555 (1997).

138. Evans E, Leung A, Heinrich V, Zhu C. Mechanical switching and coupling between two dissociation pathways in a P-selectin adhesion bond. *Proceedings of the National Academy of Sciences* **101**, 11281-11286 (2004).

139. Sun L, Cheng Q, Gao H, Zhang Y. Effect of loading conditions on the dissociation behaviour of catch bond clusters. *Journal of The Royal Society Interface* **9**, 928-937 (2011).

140. Malek AM, Alper SL, Izumo S. Hemodynamic shear stress and its role in atherosclerosis. *Jama* **282**, 2035-2042 (1999).

141. Connor J, Pak CC, Schroit AJ. Exposure of phosphatidylserine in the outer leaflet of human red blood cells. Relationship to cell density, cell age, and clearance by mononuclear cells. *Journal of Biological Chemistry* **269**, 2399-2404 (1994).

142. Cooke BM, Berendt AR, Craig AG, MacGregor J, Newbold CI, Nash GB. Rolling and stationary cytoadhesion of red blood cells parasitized by Plasmodium falciparum: separate roles for ICAM-1, CD36 and thrombospondin. *Br J Haematol* **87**, 162-170 (1994).

143. Gray C, McCormick C, Turner G, Craig A. ICAM-1 can play a major role in mediating P. falciparum adhesion to endothelium under flow. *Molecular and biochemical parasitology* **128**, 187-193 (2003).

144. Lim YB, Thingna J, Cao J, Lim CT. Single molecule and multiple bond characterization of catch bond associated cytoadhesion in malaria. *Scientific reports* **7**, 4208 (2017).

145. Dasanna AK, Lansche C, Lanzer M, Schwarz US. Rolling Adhesion of Schizont Stage Malaria-Infected Red Blood Cells in Shear Flow. *Biophys J* **112**, 1908-1919 (2017).

146. Hassan D, Arez A, Mohamed H, Elhussein A, Ibrahim M, Abdulhadi N. The reduced sequestration of Plasmodium-falciparum-infected erythrocytes among malaria cases with sickle-cell trait: in-vivo evidence from Sudan. *Annals of Tropical Medicine & Parasitology* **102**, 743-748 (2008).

147. Chakravorty SJ, Craig A. The role of ICAM-1 in Plasmodium falciparum cytoadherence. *European journal of cell biology* **84**, 15-27 (2005).

148. Oyre S, Pedersen EM, Ringgaard S, Boesiger P, Paaske W. In vivo wall shear stress measured by magnetic resonance velocity mapping in the normal human abdominal aorta. *European journal of vascular and endovascular surgery* **13**, 263-271 (1997).

149. Cholera R*, et al.* Impaired cytoadherence of Plasmodium falciparum-infected erythrocytes containing sickle hemoglobin. *Proceedings of the National Academy of Sciences* **105**, 991-996 (2008).

150. Aidoo M*, et al.* Protective effects of the sickle cell gene against malaria morbidity and mortality. *Lancet* **359**, 1311-1312 (2002).

151. Rädler J, Sackmann E. Imaging optical thicknesses and separation distances of phospholipid vesicles at solid surfaces. *Journal de Physique II* **3**, 727-748 (1993).

152. Higaki Y*, et al.* Ion-specific modulation of interfacial interaction potentials between solid substrates and cell-sized particles mediated via zwitterionic, super-hydrophilic poly (sulfobetaine) brushes. *The Journal of Physical Chemistry B* **121**, 1396-1404 (2017).

153. Wiegand G, Jaworek T, Wegner G, Sackmann E. Studies of structure and local wetting properties on heterogeneous, micropatterned solid surfaces by microinterferometry. *Journal of colloid and interface science* **196**, 299-312 (1997).

154. Wiegand G, Neumaier KR, Sackmann E. Microinterferometry: three-dimensional reconstruction of surface microtopography for thin-film and wetting studies by reflection interference contrast microscopy (RICM). *Applied optics* **37**, 6892-6905 (1998).

155. Reynolds GO. *The New Physical Optics Notebook: Tutorials in Fourier Optics*. ERIC (1989).

156. Monzel C, Fenz SF, Merkel R, Sengupta K. Probing Biomembrane Dynamics by Dual-Wavelength Reflection Interference Contrast Microscopy. *ChemPhysChem* **10**, 2828-2838 (2009).

157. Ploem J. *Reflection-contrast microscopy as a tool for investigation of the attachment of living cells to a glass surface*. Blackwell, Oxford (1975).

158. Limozin L, Sengupta K. Quantitative reflection interference contrast microscopy (RICM) in soft matter and cell adhesion. *ChemPhysChem* **10**, 2752-2768 (2009).

159. Bass M, DeCusatis C, Li G, MacDonald CA, Van Stryland EW, Optical Society of A. Handbook of optics. (2010).

160. Higaki Y*, et al.* Ion-Specific Modulation of Interfacial Interaction Potentials between Solid Substrates and Cell-Sized Particles Mediated via Zwitterionic, Super-Hydrophilic Poly(sulfobetaine) Brushes. *The Journal of Physical Chemistry B* **121**, 1396-1404 (2017).

161. Park Y*, et al.* Refractive index maps and membrane dynamics of human red blood cells parasitized by Plasmodium falciparum. *Proceedings of the National Academy of Sciences* **105**, 13730-13735 (2008).

162. Dillard P, Pi F, Lellouch AC, Limozin L, Sengupta K. Nano-clustering of ligands on surrogate antigen presenting cells modulates T cell membrane adhesion and organization. *Integrative Biology* **8**, 287-301 (2016).

163. Matsuzaki T*, et al.* High contrast visualization of cell–hydrogel contact by advanced interferometric optical microscopy. *The journal of physical chemistry letters* **5**, 253-257 (2013).

164. Fedosov DA, Caswell B, Karniadakis GE. Wall shear stress-based model for adhesive dynamics of red blood cells in malaria. *Biophysical journal* **100**, 2084-2093 (2011).

165. Dasanna AK, Schwarz US, Gompper G, Fedosov DA. Multiscale Modeling of Malaria-Infected Red Blood Cells. In: *Handbook of Materials Modeling: Applications: Current and Emerging Materials* (ed^(eds Andreoni W, Yip S). Springer International Publishing (2018).

166. Dong C, Cao J, Struble EJ, Lipowsky HH. Mechanics of leukocyte deformation and adhesion to endothelium in shear flow. *Annals of biomedical engineering* **27**, 298-312 (1999).

167. Luo ZY, Wang SQ, He L, Lu TJ, Xu F, Bai BF. Front tracking simulation of cell detachment dynamic mechanism in microfluidics. *Chemical Engineering Science* **97**, 394-405 (2013).

168. Ho M, Hickey MJ, Murray AG, Andonegui G, Kubes P. Visualization of Plasmodium falciparum–endothelium interactions in human microvasculature: mimicry of leukocyte recruitment. *Journal of Experimental Medicine* **192**, 1205-1212 (2000).

169. Schmid-Schönbein GW, Usami S, Skalak R, Chien S. The interaction of leukocytes and erythrocytes in capillary and postcapillary vessels. *Microvascular research* **19**, 45-70 (1980).

170. Goldsmith HL, Spain S. Margination of leukocytes in blood flow through small tubes. *Microvascular research* **27**, 204-222 (1984).

171. Hou HW*, et al.* Deformability based cell margination—a simple microfluidic design for malaria-infected erythrocyte separation. *Lab on a Chip* **10**, 2605-2613 (2010).

172. Moore KL*, et al.* P-selectin glycoprotein ligand-1 mediates rolling of human neutrophils on P-selectin. *The Journal of cell biology* **128**, 661-671 (1995).

173. Cutts EE*, et al.* Structural analysis of P. falciparum KAHRP and PfEMP1 complexes with host erythrocyte spectrin suggests a model for cytoadherent knob protrusions. *PLoS Pathog* **13**, e1006552 (2017).

174. McCormick CJ, Craig A, Roberts D, Newbold CI, Berendt AR. Intercellular adhesion molecule-1 and CD36 synergize to mediate adherence of Plasmodium falciparum-infected erythrocytes to cultured human microvascular endothelial cells. *The Journal of clinical investigation* **100**, 2521-2529 (1997).

175. Luo ZY, Bai BF. State diagram for adhesion dynamics of deformable capsules under shear flow. *Soft matter* **12**, 6918-6925 (2016).

176. Erdmann T, Schwarz U. Stability of adhesion clusters under constant force. *Physical review letters* **92**, 108102 (2004).

177. Erdmann T, Schwarz US. Stochastic dynamics of adhesion clusters under shared constant force and with rebinding. *The Journal of chemical physics* **121**, 8997-9017 (2004).

178. Evans E, Yeung A. Apparent viscosity and cortical tension of blood granulocytes determined by micropipet aspiration. *Biophysical journal* **56**, 151-160 (1989).

179. Mathur AB, Collinsworth AM, Reichert WM, Kraus WE, Truskey GA. Endothelial, cardiac muscle and skeletal muscle exhibit different viscous and elastic properties as determined by atomic force microscopy. *Journal of biomechanics* **34**, 1545-1553 (2001).

180. Chen J, Fabry B, Schiffrin EL, Wang N. Twisting integrin receptors increases endothelin-1 gene expression in endothelial cells. *American Journal of Physiology-Cell Physiology* **280**, C1475-C1484 (2001).

181. Browicz T. Further observation of motion phenomena on red blood cells in pathological states. *Zbl med Wissen* **28**, 625-627 (1890).

182. Helfrich W, Servuss R-M. Undulations, steric interaction and cohesion of fluid membranes. *Il Nuovo Cimento D* **3**, 137-151 (1984).

183. Gov N, Safran S. Red blood cell shape and fluctuations: cytoskeleton confinement and ATP activity. *Journal of Biological Physics* **31**, 453-464 (2005).

184. Gov N, Zilman A, Safran S. Cytoskeleton confinement and tension of red blood cell membranes. *Physical review letters* **90**, 228101 (2003).

185. Pecreaux J, Dobereiner HG, Prost J, Joanny JF, Bassereau P. Refined contour analysis of giant unilamellar vesicles. *The European physical journal E, Soft matter* **13**, 277-290 (2004).

186. Betz T, Sykes C. Time resolved membrane fluctuation spectroscopy. *Soft Matter* **8**, 5317-5326 (2012).

187. Milner ST, Safran S. Dynamical fluctuations of droplet microemulsions and vesicles. *Physical Review A* **36**, 4371 (1987).

188. Lamb H. *Hydrodynamics* (1945).

189. Engelberg S. *Random signals and noise: a mathematical introduction*. CRC Press (2006).

190. Betz T, Lenz M, Joanny J-F, Sykes C. ATP-dependent mechanics of red blood cells. *Proceedings of the National Academy of Sciences* **106**, 15320-15325 (2009).

191. Yoon Y-Z*, et al.* Flickering analysis of erythrocyte mechanical properties: dependence on oxygenation level, cell shape, and hydration level. *Biophysical journal* **97**, 1606-1615 (2009).

192. Ito H*, et al.* Quantification of the Influence of Endotoxins on the Mechanics of Adult and Neonatal Red Blood Cells. *The Journal of Physical Chemistry B* **119**, 7837-7845 (2015).

193. Suresh S*, et al.* Connections between single-cell biomechanics and human disease states: gastrointestinal cancer and malaria. *Acta biomaterialia* **1**, 15-30 (2005).

194. Zhang Y*, et al.* Multiple stiffening effects of nanoscale knobs on human red blood cells infected with Plasmodium falciparum malaria parasite. *Proceedings of the National Academy of Sciences* **112**, 6068-6073 (2015).

195. Lanzer M, Wertheimer SP, de Bruin D, Ravetch JV. Chromatin structure determines the sites of chromosome breakages in Plasmodium falciparum. *Nucleic acids research* **22**, 3099-3103 (1994).

196. Dondorp AM, Kager PA, Vreeken J, White NJ. Abnormal blood flow and red blood cell deformability in severe malaria. *Parasitology today* **16**, 228-232 (2000).

197. Nguitragool W*, et al.* Malaria parasite clag3 genes determine channel-mediated nutrient uptake by infected red blood cells. *Cell* **145**, 665-677 (2011).

198. Smith JD, Rowe JA, Higgins MK, Lavstsen T. Malaria's deadly grip: cytoadhesion of Plasmodium falciparum-infected erythrocytes. *Cellular microbiology* **15**, 1976-1983 (2013).

199. Cokelet GR, Meiselman HJ. Rheological comparison of hemoglobin solutions and erythrocyte suspensions. *Science* **162**, 275-277 (1968).

200. Turgeon ML. *Clinical Hematology: Theory and Procedures 5th edition*. Lippincott Williams & Wilkins (2011).

201. Lew VL, Tiffert T, Ginsburg H. Excess hemoglobin digestion and the osmotic stability of Plasmodium falciparum-infected red blood cells. *Blood* **101**, 4189-4194 (2003).

202. Hosseini SM, Feng JJ. How malaria parasites reduce the deformability of infected red blood cells. *Biophysical journal* **103**, 1-10 (2012).

203. Lai L, Xu X, Lim CT, Cao J. Stiffening of Red Blood Cells Induced by Cytoskeleton Disorders: A Joint Theory-Experiment Study. *Biophysical journal* **109**, 2287-2294 (2015).

204. Cyrklaff M*, et al.* Hemoglobins S and C interfere with actin remodeling in Plasmodium falciparum-infected erythrocytes. *Science* **334**, 1283-1286 (2011).

205. Lavazec C. Molecular mechanisms of deformability of Plasmodium-infected erythrocytes. *Current opinion in microbiology* **40**, 138-144 (2017).

206. Fröhlich B, Jäger J. Haemoglobin S and C affect biomechanical membrane properties of *P. falciparum*-infected erythrocytes. *Manuscript submitted for publication*, (2019).

207. Turlier H, Betz T. Fluctuations in active membranes. *arXiv preprint arXiv:180100176*, (2017).

208. Turlier H*, et al.* Equilibrium physics breakdown reveals the active nature of red blood cell flickering. *Nature Physics* **12**, 513 (2016).

209. Mauritz JM, Esposito A, Ginsburg H, Kaminski CF, Tiffert T, Lew VL. The homeostasis of Plasmodium falciparum-infected red blood cells. *PLoS computational biology* **5**, e1000339 (2009).

210. Korytowski AA. Influence of Lipid Oxidization on Structures and Functions of Biological Membranes. (ed^(eds) (2016).

211. Carron NJ. *An introduction to the passage of energetic particles through matter*. CRC Press (2006).

212. Beckhoff B, Kanngießer B, Langhoff N, Wedell R, Wolff H. *Handbook of practical X-ray fluorescence analysis*. Springer Science & Business Media (2007).

213. Hubbell JH, Seltzer SM. Tables of X-ray mass attenuation coefficients and mass energy-absorption coefficients 1 keV to 20 MeV for elements Z= 1 to 92 and 48 additional substances of dosimetric interest. (ed^(eds). National Inst. of Standards and Technology-PL, Gaithersburg, MD (United … (1995).

214. Henke BL, Gullikson EM, Davis JC. X-ray interactions: photoabsorption, scattering, transmission, and reflection at E= 50-30,000 eV, Z= 1-92. *Atomic data and nuclear data tables* **54**, 181-342 (1993).

215. Susini J*, et al.* New challenges in beamline instrumentation for the ESRF Upgrade Programme Phase II. *Journal of synchrotron radiation* **21**, 986-995 (2014).

216. Cloetens P*, et al.* Holotomography: Quantitative phase tomography with micrometer resolution using hard synchrotron radiation x rays. *Applied physics letters* **75**, 2912-2914 (1999).

217. Gramaccioni C*, et al.* Nanoscale quantification of intracellular element concentration by X-ray fluorescence microscopy combined with X-ray phase contrast nanotomography. *Applied Physics Letters* **112**, 053701 (2018).

218. Krause MO. Atomic radiative and radiationless yields for K and L shells. *Journal of physical and chemical reference data* **8**, 307-327 (1979).

219. Solé V, Papillon E, Cotte M, Walter P, Susini J. A multiplatform code for the analysis of energy-dispersive X-ray fluorescence spectra. *Spectrochimica Acta Part B: Atomic Spectroscopy* **62**, 63-68 (2007).

220. Frank V*, et al.* Lensless Tomographic Imaging of Near Surface Structures of Frozen Hydrated Malaria-Infected Human Erythrocytes by Coherent X-Ray Diffraction Microscopy. *Scientific reports* **7**, 14081 (2017).

221. Kanias T, Acker JP. Biopreservation of red blood cells–the struggle with hemoglobin oxidation. *The FEBS journal* **277**, 343-356 (2010).

222. Yildiz D, Uslu C, Cakir Y, Oztas H. L-Cysteine influx and efflux: A possible role for red blood cells in regulation of redox status of the plasma. *Free radical research* **40**, 507-512 (2006).

223. Sarpel G, Barp A, Lubansky H, Omachi A. Erythocyte phosphate content in Huntington's disease. *Neuroscience letters* **31**, 91-96 (1982).

224. Schoorl M, Schoorl M, van der Gaag D, Bartels PCM. Effects of iron supplementation on red blood cell hemoglobin content in pregnancy. *Hematology reports* **4**, e24-e24 (2012).

225. Marvin RG*, et al.* Fluxes in “free” and total zinc are essential for progression of intraerythrocytic stages of Plasmodium falciparum. *Chemistry & biology* **19**, 731-741 (2012).

226. Rasoloson D, Lirong S, Chong CR, Kafsack BF, Sullivan DJ. Copper pathways in Plasmodium falciparum infected erythrocytes indicate an efflux role for the copper P-ATPase. *Biochemical Journal* **381**, 803-811 (2004).

227. Moore LR*, et al.* Hemoglobin degradation in malaria-infected erythrocytes determined from live cell magnetophoresis. *FASEB journal : official publication of the Federation of American Societies for Experimental Biology* **20**, 747-749 (2006).

228. Huang X*, et al.* Soft X-Ray Diffraction Microscopy of a Frozen Hydrated Yeast Cell. *PHYSICAL REVIEW LETTERS* **103**, 198101 (2009).

229. Dhingra R*, et al.* Relations of serum phosphorus and calcium levels to the incidence of cardiovascular disease in the community. *Archives of internal medicine* **167**, 879-885 (2007).

230. Bremner K, Bubb WA, Kemp GJ, Trenell MI, Thompson CH. The effect of phosphate loading on erythrocyte 2, 3-bisphosphoglycerate levels. *Clinica Chimica Acta* **323**, 111-114 (2002).

231. Ding XC, Beck H-P, Raso G. Plasmodium sensitivity to artemisinins: magic bullets hit elusive targets. *Trends in parasitology* **27**, 73-81 (2011).

232. Choveaux DL, Przyborski JM, Goldring JD. A Plasmodium falciparum copper-binding membrane protein with copper transport motifs. *Malaria journal* **11**, 397 (2012).

233. Bozdech Z, Ginsburg H. Antioxidant defense in Plasmodium falciparum–data mining of the transcriptome. *Malaria journal* **3**, 23 (2004).

234. Saliba KJ*, et al.* Sodium-dependent uptake of inorganic phosphate by the intracellular malaria parasite. *Nature* **443**, 582 (2006).

235. Gruber W, Deuticke B. Comparative aspects of phosphate transfer across mammalian erythrocyte membranes. *The Journal of membrane biology* **13**, 19-36 (1973).

236. Van der Zee J, Dubbelman T, Van Steveninck J. Peroxide-induced membrane damage in human erythrocytes. *Biochimica et Biophysica Acta (BBA)-Biomembranes* **818**, 38-44 (1985).

237. Bose S*, et al.* Affinity flow fractionation of cells via transient interactions with asymmetric molecular patterns. *Scientific reports* **3**, 2329 (2013).

238. Dasanna AK, Schwarz US. Adhesion-based sorting of blood cells: an adhesive dynamics simulation study. *Soft matter* **14**, 9061-9070 (2018).

239. Van Deenen L. Some structural and dynamic aspects of lipids in biological membranes. *Annals of the New York Academy of Sciences* **137**, 717-730 (1966).

240. Nelson GJ. Lipid composition of erythrocytes in various mammalian species. *Biochimica et Biophysica Acta (BBA)-Lipids and Lipid Metabolism* **144**, 221-232 (1967).

241. Iwata R, Suk-In P, Hoven VP, Takahara A, Akiyoshi K, Iwasaki Y. Control of nanobiointerfaces generated from well-defined biomimetic polymer brushes for protein and cell manipulations. *Biomacromolecules* **5**, 2308-2314 (2004).

242. Schlenoff JB. Zwitteration: coating surfaces with zwitterionic functionality to reduce nonspecific adsorption. *Langmuir* **30**, 9625-9636 (2014).

243. Shao Q, Jiang S. Molecular understanding and design of zwitterionic materials. *Advanced Materials* **27**, 15-26 (2015).

244. Zhang Z, Chao T, Chen S, Jiang S. Superlow fouling sulfobetaine and carboxybetaine polymers on glass slides. *Langmuir* **22**, 10072-10077 (2006).

245. Wang T, Wang X, Long Y, Liu G, Zhang G. Ion-specific conformational behavior of polyzwitterionic brushes: exploiting it for protein adsorption/desorption control. *Langmuir* **29**, 6588-6596 (2013).

246. Tairy O, Kampf N, Driver MJ, Armes SP, Klein J. Dense, highly hydrated polymer brushes via modified atom-transfer-radical-polymerization: structure, surface interactions, and frictional dissipation. *Macromolecules* **48**, 140-151 (2014).

247. Kobayashi M, Takahara A. Tribological properties of hydrophilic polymer brushes under wet conditions. *The Chemical Record* **10**, 208-216 (2010).

248. Kobayashi M, Terayama Y, Kikuchi M, Takahara A. Chain dimensions and surface characterization of superhydrophilic polymer brushes with zwitterion side groups. *Soft Matter* **9**, 5138-5148 (2013).

249. Kobayashi M, Ishihara K, Takahara A. Neutron reflectivity study of the swollen structure of polyzwitterion and polyeletrolyte brushes in aqueous solution. *Journal of Biomaterials Science, Polymer Edition* **25**, 1673-1686 (2014).

250. Kühner M, Sackmann E. Ultrathin hydrated dextran films grafted on glass: preparation and characterization of structural, viscous, and elastic properties by quantitative microinterferometry. *Langmuir* **12**, 4866-4876 (1996).

251. Albersdörfer A, Sackmann E. Swelling behavior and viscoelasticity of ultrathin grafted hyaluronic acid films. *The European Physical Journal B-Condensed Matter and Complex Systems* **10**, 663-672 (1999).

252. Tanaka M*, et al.* Wetting and dewetting of extracellular matrix and glycocalix models. *Journal of Physics: Condensed Matter* **17**, S649 (2005).

253. Prieve DC, Bike SG, Frej NA. Brownian motion of a single microscopic sphere in a colloidal force field. *Faraday Discussions of the Chemical Society* **90**, 209-222 (1990).

254. Oncsik T, Trefalt G, Borkovec M, Szilagyi I. Specific ion effects on particle aggregation induced by monovalent salts within the Hofmeister series. *Langmuir* **31**, 3799-3807 (2015).

255. Reynolds O. XXIX. An experimental investigation of the circumstances which determine whether the motion of water shall be direct or sinuous, and of the law of resistance in parallel channels. *Philosophical Transactions of the Royal society of London*, 935-982 (1883).

256. Pincus P. Colloid stabilization with grafted polyelectrolytes. *Macromolecules* **24**, 2912-2919 (1991).

257. Derjaguin B. Some results from 50 years' research on surface forces. In: *Surface forces and surfactant systems* (ed^(eds). Springer (1987).

258. Terayama Y, Kikuchi M, Kobayashi M, Takahara A. Well-defined poly (sulfobetaine) brushes prepared by surface-initiated ATRP using a fluoroalcohol and ionic liquids as the solvents. *Macromolecules* **44**, 104-111 (2010).

259. Higaki Y, Kobayashi M, Murakami D, Takahara A. Anti-fouling behavior of polymer brush immobilized surfaces. *Polymer Journal* **48**, 325 (2016).

260. Blakeston AC*, et al.* New poly (amino acid methacrylate) brush supports the formation of well-defined lipid membranes. *Langmuir* **31**, 3668-3677 (2015).

261. Zhao X*, et al.* Solution pH-regulated interfacial adsorption of diblock phosphorylcholine copolymers. *Langmuir* **21**, 9597-9603 (2005).

262. Morita S, Tanaka M, Ozaki Y. Time-resolved in situ ATR-IR observations of the process of sorption of water into a poly (2-methoxyethyl acrylate) film. *Langmuir* **23**, 3750-3761 (2007).

263. Murakami D, Kobayashi M, Moriwaki T, Ikemoto Y, Jinnai H, Takahara A. Spreading and structuring of water on superhydrophilic polyelectrolyte brush surfaces. *Langmuir* **29**, 1148-1151 (2013).

264. World Health Organization. World Malaria Report 2013. *WHO Press*, (2013).

265. Barber BE, Rajahram GS, Grigg MJ, William T, Anstey NM. World Malaria Report: time to acknowledge Plasmodium knowlesi malaria. *Malaria journal* **16**, 135 (2017).

266. Rayleigh L. VIII. On the pressure developed in a liquid during the collapse of a spherical cavity. *The London, Edinburgh, and Dublin Philosophical Magazine and Journal of Science* **34**, 94-98 (1917).

267. Bilaniuk N, Wong GS. Erratum: Speed of sound in pure water as a function of temperature [J. Acoust. Soc. Am. 93, 1609–1612 (1993)]. *The Journal of the Acoustical Society of America* **99**, 3257-3257 (1996).